

Abstract

BURNETTE, JAMES E. JR. Formation of Metal Silicide and Metal Germanosilicide Contacts to $\text{Si}_{1-x}\text{Ge}_x$ Alloys. (Under the direction of Dr. Dale E. Sayers and Dr. Robert J. Nemanich.)

The goals of this research were to study the phase stability and formation of Ti- $\text{Si}_{1-x}\text{Ge}_x$ and Co- $\text{Si}_{1-x}\text{Ge}_x$ thin film reactions. The Ti- $\text{Si}_{1-x}\text{Ge}_x$ and Co- $\text{Si}_{1-x}\text{Ge}_x$ solid phase reactions result in the formation of precipitates within the grain boundaries of the films thus formed. The precipitates are either Ge or a Si-Ge compound, depending on the type of metal used in the reaction.

The formation of $\text{Ti}(\text{Si}_{1-y}\text{Ge}_y)_2$ thin films on $\text{Si}_{1-x}\text{Ge}_x$ has been examined. It has been found that the generation of Ge-rich Si-Ge precipitates which form in the Ti- $\text{Si}_{1-x}\text{Ge}_x$ solid phase reaction could be reduced or eliminated by the insertion of an amorphous Si layer before the metallization step. A Gibbs free energy model, which was parameterized in terms of Ge concentration by atomic percentage was used to determine stability between the $\text{Ti}(\text{Si}_{1-y}\text{Ge}_y)_2$ layer and the $\text{Si}_{1-x}\text{Ge}_x$ substrate. The films in this study were characterized using x-ray diffraction (XRD) to investigate phase formation, stability, and the composition of the $\text{Ti}(\text{Si}_{1-y}\text{Ge}_y)_2$ layer. Scanning electron microscopy (SEM) was used to determine the surface morphology and phase stability. It was found that amorphous Si layers of a certain thickness could prevent precipitate formation, depending on the composition of the underlying $\text{Si}_{1-x}\text{Ge}_x$ layer.

The formation of CoSi_2 on $\text{Si}_{1-x}\text{Ge}_x$ was also examined. The solid phase reaction of Co and $\text{Si}_{1-x}\text{Ge}_x$ results in the formation of a poly-crystalline CoSi_2 layer, and the occurrence of a Ge precipitate. The TIME (Titanium Interlayer Mediated Epitaxy) process has been used in the formation of epitaxial CoSi_2 on Si (100). A Ti layer of varying thicknesses, which serves as a barrier to retard the diffusion of Co atoms was deposited on a c-Si/ $\text{Si}_{1-x}\text{Ge}_x$ substrate pseudomorphically strained to Si (100), before the final Co metallization step. The films in this study were characterized using x-ray absorption fine structure (XAFS) to determine the short-range crystalline order, XRD to determine phase formation and long-range crystalline order, Auger electron spectroscopy (AES) to determine surface chemistry, and SEM to determine the surface morphology. This work shows that the formation of epitaxial CoSi_2 on $\text{Si}_{1-x}\text{Ge}_x$ can be achieved, depending on the thickness of the diffusion barrier. In addition, the optimal diffusion barrier thickness has been determined for the Co layer thickness used in these studies.

**Formation of Metal Silicide and Metal Germanosilicide Contacts to $\text{Si}_{1-x}\text{Ge}_x$
Alloys**

by

James E. Burnette, Jr.

A Dissertation submitted to the Graduate Faculty of

North Carolina State University

in partial fulfillment of the

requirements for the Degree of

Doctor of Philosophy

Physics

Raleigh

2004

APPROVED BY:

Co-chair of Advisory Committee

Co-chair of Advisory Committee

Biography

I was born on May 26, 1970 in Memphis, Tennessee. I was the product of a working-class family. My mother emphasized the importance of education very early on in my life, and apparently, I paid attention to her words. Life was pretty non-descript as a child, but by the time I was old enough for kindergarten, it was discovered by my teachers that I was well advanced beyond my years. After a battery of tests, it had been discovered that I was a “gifted” student. Thankfully, the Memphis City School system had what was known as the Optional Program, whose mission was to nurture and develop the abilities of those students who were considered “smart”. This is where my introduction to the world of science began, and where my passions were cultivated.

After graduating from Memphis East High School in 1988, where I was enrolled in their pre-Engineering program, I enrolled as a freshman at Morehouse College, in Atlanta, GA, graduating with a Bachelors of Science degree in Physics in May of 1993. From there, I went to Clark-Atlanta University in 1994, obtaining a Masters of Science degree in Physics in July 1995. My research at Clark-Atlanta focused on the nonlinear dynamics of biological systems, under the tutelage of Dr. Ronald E. Mickens.

It was in August of 1996 that I enrolled in North Carolina State University, as a Ph.D student in the Department of Physics. Upon passing the Departmental Qualifying Exam, I began my career as an experimental physicist under the direction of Dr. Dale Sayers and Dr. Robert Nemanich. It has been a pleasure to work for these individuals.

Acknowledgements

I would like to thank my co-advisors, Dr. Dale Sayers and Dr. Robert J. Nemanich, for providing direction and inspiration for my research. I would also like to thank them for the patience and understanding they have granted me during my tenure in their research group. I would also like to give thanks to Dr. David Aspnes and Dr. Gregory Parsons for agreeing to be part of my dissertation committee, and for their continued support and knowledge that they have given to me along the way.

Special thanks go out to the past and present members of the Surface Science Laboratory, for their assistance during my stay. In particular, I would like to thank Brian Coppa, Jaeseob Lee, Charlie Fulton, Jacob Gargulio, Franz Koeck (Thanks for the SEM work!), Eugene Bryan, Anderson Sunda-Meya, and the members of the Heteroepitaxy Group for their continued support.

Continued thanks go out to those who provided technical assistance during experiments at Brookhaven National Laboratories, in particular Larry Fareria and Kumi Pandya.

Last but not least, I would like to thank those individuals who have supported and influenced me along the way, namely my wife, Samara Fleming Burnette; I would like to thank her especially for her patience. I would also like to thank my parents, William and Shirley Hines, for their support throughout my post-secondary educational experience. Thanks goes out to friends and colleagues I have met in Georgia and North Carolina during my entire collegiate experience: Willyetta Brown-Mitchell, Myron Murray, Samuel Acha, Dustin Kapraun, Danielle Elswick, Miklos

Kiss, David and Dianne Pierson, Sean Hendrick, Beverly Clark, Darryl Brown, Kevin Nesbitt, Mark McCarthy, Paul McCarthy, Author Johnson, Verlon Grimes, Brian Winston, John Irving, Frazier Hubbard, Juliette Griggs, Phillip Todd Parker, Anthony Ransfer, and Kenyatta Lee.

Table of Contents

List of Journal Papers and Review Articles.....	vii
List of Tables	viii
List of Figures.....	ix
1. Introduction.....	1
1.1 Technical Motivation.....	6
1.2 SALICIDE Process.....	8
1.3 Solid Phase Reactions.....	11
1.3.1 Titanium-Silicon Solid Phase Reaction	11
1.3.2 Titanium-Germanium Solid Phase Reaction	12
1.3.3 Ti-Si _{1-x} Ge _x Solid Phase Reaction.....	13
1.3.4 Co-Si Solid Phase Reaction	18
1.3.5 Co-Si _{1-x} Ge _x Solid Phase Reaction.....	19
1.3.6 Co-Ti-Si Solid Phase Reaction	20
1.3.7 Dissertation Overview	23
References.....	25
2. Experimental.....	30
2.1 Technical Aspects.....	30
2.2 Sample Preparation.....	31
2.3 X-ray Absorption Fine Structure	34
2.3.1 Introduction.....	34
2.3.2 The EXAFS Equation	36
2.3.3 Data Collection	37
2.3.4 Data Analysis.....	41
2.4 X-ray Diffraction	43
2.5 Auger Electron Spectroscopy	46
2.6 Scanning Electron Microscopy.....	49
References.....	51
3. Growth and Stability of Titanium Germanosilicide Thin Films on Si _{1-x} Ge _x	53
3.1 Introduction.....	54
3.2 Experiment.....	56
3.3 Results.....	59
3.4 Discussion.....	63
3.4.1 Equilibrium Concentrations.....	63
3.4.2 Reaction Dynamics	67
3.4.3 Experimental Analysis.....	69
3.5 Conclusion	77
References.....	79
4. Titanium Interlayer Mediated Epitaxy of CoSi ₂ on Si _{1-x} Ge _x	82
4.1 Introduction.....	83
4.2 Experiment.....	85

4.3	Results.....	87
4.4	Discussion.....	97
4.5	Conclusion.....	106
	References.....	109
5.	Conclusions.....	112
5.1	Ti(Si _{1-y} Ge _y) ₂ /Si _{1-x} Ge _x stability.....	112
5.2	CoSi ₂ /Si _{1-x} Ge _x	113
5.3	Future Work.....	114

List of Journal Papers and Review Articles

1. J.E. Burnette, M. Himmerlich, and R. J. Nemanich (2004). Silicide Contacts for Si-Ge Devices. Silicide Technology for ULSI. IEE EMIS Processing Series.
2. J.E. Burnette, R.J. Nemanich, D.E. Sayers, “Thermodynamically Stable $\text{Ti}(\text{Si}_{1-y}\text{Ge}_y)_2$ Thin Films on $\text{Si}_{1-x}\text{Ge}_x$ ”, Journal of Materials Research, to be submitted for publication.
3. J.E. Burnette, D.E. Sayers, R.J. Nemanich, “Titanium Interlayer Mediated Epitaxy of CoSi_2 on $\text{Si}_{1-x}\text{Ge}_x$ ”, Journal of Applied Physics, to be submitted for publication.
4. W. Platow, D.K. Wood, J.E. Burnette, R.J. Nemanich, D.E. Sayers, “Formation of $\sqrt{3} \times \sqrt{3}$ CoSi_2 on 6-H SiC (0001)”, Journal of Synchrotron Radiation **8**, 475-477.
5. W. Platow, D.K. Wood, J.E. Burnette, R.J. Nemanich, and D. E. Sayers, “On the Formation of Cobalt Disilicide films on $\sqrt{3} \times \sqrt{3}$ 6H-SiC (0001)”, Phys. Rev. B. **63**, 115312-1-115312-7.

List of Tables

Table 1.1: Composition and structure of terminal refractory silicide and germanide phases. The silicide and germanide phases of Ni, Co, Pt, and Pd do not exist in the C54, C11 _b , C40, or C49 structures, but their respective structures are listed.....	5
--	---

List of Figures

Figure 1.1: Arrangement of metal and semiconducting atoms in the stacking planes of the C11 _b , C40, C49, and C54 crystal structures. The metal atoms are indicated by the open circles, which are surrounded by six semiconductor atoms, which are indicated by the solid circles. The in-plane lattice directions in the C11 _b , C49, and C54 structures are along the directions of the sides of the dashed box shown in the figure. Reprinted from Ref. [1].	1
Figure 1.2: The layer stacking sequence for the C49 (a) and C54 (b) phases. The dark vertical lines indicate the alignment of the layers. The C49 structure (a) is characterized by a A-B* stacking sequence, where the metal atoms in each layer are located above adjacent semiconductor and metal atoms, while the C54 structure (b) is characterized by an A-B-D-C stacking sequence, where the metal atoms are located above adjacent semiconductor atoms. Reprinted from Ref [1].	3
Figure 1.3: Schematic MOSFET structures which indicate where Si _{1-x} Ge _x alloys can be incorporated to enhance device performance. (a) A compressively strained conduction channel, (b) Si conduction channel under tensile strain from a “virtual” Si _{1-x} Ge _x substrate, (c) tunable ploy-Si _{1-x} Ge _x gate electrode, (d) ultra-shallow Si _{1-x} Ge _x source-drain extensions. Reproduced from Ref. [43].	7
Figure 1.4: Ti-Si-Ge ternary phase diagram at 700°C, indicating stability between Ti(Si _{1-y} Ge _y) ₂ film and Si _{1-x} Ge _x substrate for compositions x = 0.10, 0.20, ..., 0.90.	17
Figure 1.5: Si-rich portion of the ternary phase diagram for the Co-Ti-Si solid phase reaction at 800°C. Reproduced from information in Ref. [41].	23
Figure 2.1: Integrated Analysis and Processing Tool.	33
Figure 2.2: XAFS experimental layout at Beamline X11-A.	39
Figure 2.3: Fluorescent x-ray photon produced from an electronic transition between the 2P _{3/2} and 1S core hole states. Reprinted from Ref [6].	40
Figure 2.4: Schematic depicting the creation of a doubly ionized electronic state as an electron from the 2P _{3/2} energy level fills a core hole in the 1S energy level, and the emergence of an Auger electron, with kinetic energy equal to the difference in energies of the initial and doubly ionized states. Reproduced from Ref. [6].	46

Figure 2.5: AES scan, which indicates the presence of Si and Ti. The locations of the peaks are associated with KLL and LMN electronic transitions for Si and Ti, respectively.	48
Figure 3.1: Layered structure after deposition and subsequent phase formation, leading to the formation of a $\text{Ti}(\text{Si}_{1-y}\text{Ge}_y)_2$ phase in equilibrium with the substrate.....	51
Figure 3.2: θ -2 θ XRD scan of C54 $\text{Ti}(\text{Si}_{1-y}\text{Ge}_y)_2$ compound on a strained Si_8Ge_2 substrate. The intensity peaks from (313), (004), and (311) diffraction planes are shown.....	59
Figure 3.3: θ -2 θ XRD scan of C54 $\text{Ti}(\text{Si}_{1-y}\text{Ge}_y)_2$ compound on a strained Si_7Ge_3 substrate. The intensity peaks from (313), (004), and (311) diffraction planes are shown.....	60
Figure 3.4: SEM micrographs of (a) as deposited, (b) 100 Å, (c) 400 Å, (d) 500 Å, and (e) 600 Å amorphous Si layered samples on a Si_8Ge_2 substrate annealed to 700°C. C54 $\text{Ti}(\text{Si}_{1-y}\text{Ge}_y)_2$ grains and $\text{Si}_{1-z}\text{Ge}_z$ precipitates shown.....	62
Figure 3.5: SEM micrographs of (a) as deposited, (b) 100 Å, (c) 400 Å, (d) 500 Å, and (e) 600 Å amorphous Si layered samples on a Si_7Ge_3 substrate annealed to 700°C. C54 $\text{Ti}(\text{Si}_{1-y}\text{Ge}_y)_2$ grains and $\text{Si}_{1-z}\text{Ge}_z$ precipitates shown.....	64
Figure 3.6: Plot of the germanium concentrations of C54 $\text{Ti}(\text{Si}_{1-y}\text{Ge}_y)_2$ layer in equilibrium with the $\text{Si}_{1-x}\text{Ge}_x$ substrate at 600°C, 700°C, and 800°C. Equilibrium in the high-temperature limit indicated by the dashed line.	66
Figure 3.7: Ternary phase diagram of $\text{Ti}(\text{Si}_{1-y}\text{Ge}_y)_2/\text{Si}_{1-x}\text{Ge}_x$ reaction, indicating titanium germanosilicide compound in equilibrium with Si_8Ge_2 substrate. Arrows indicate initial concentrations of the 100 Å, 400Å, 500Å, 600Å amorphous layered samples and Ti directly deposited onto Si_8Ge_2 substrate. As seen from the diagram, the 600 Å sample should be precipitate free, while the 100 Å, 400 Å, 500, and directly deposited samples should show evidence of precipitate formation at the $\text{Ti}(\text{Si}_{1-y}\text{Ge}_y)_2$ grain boundaries.	71
Figure 3.8: Ternary phase diagram of 1 mol-1 mol $\text{Ti}(\text{Si}_{1-y}\text{Ge}_y)_2/\text{Si}_{1-x}\text{Ge}_x$ reaction, indicating titanium germanosilicide compound in equilibrium with Si_7Ge_3 substrate. Arrows indicate initial concentrations of the 100 Å, 400Å, 500Å, 600Å amorphous layered samples and Ti directly deposited onto Si_7Ge_3 substrate. As seen from the diagram, the 500 and 600 Å samples should be precipitate free, while the 100 Å, 400 Å, and directly-	

deposited samples should show evidence of precipitate formation at the $\text{Ti}(\text{Si}_{1-y}\text{Ge}_y)_2$ grain boundaries..... 73

Figure 3.9: Comparison of y' (initial Ge concentration) and y (final Ge concentration) of as-deposited and amorphous layered samples for $\text{Si}_{0.8}\text{Ge}_{0.2}$ substrates calculated from XRD for (004) and (311) orientations. The solid line indicates y' versus the a-Si layer thickness. Symbols represent the Ge concentration versus a-Si layer thickness, as determined from the (004) and (311) diffraction peaks. The equilibrium Ge concentration of the $\text{Ti}(\text{Si}_{1-y}\text{Ge}_y)_2$ compound is 0.05 for this substrate, and is indicated by the dashed line..... 74

Figure 3.10: Comparison of y' (initial Ge concentration) and y (final Ge concentration) of as-deposited and amorphous layered samples for $\text{Si}_{0.7}\text{Ge}_{0.3}$ substrates calculated from XRD for (004) and (311) orientations. The solid line indicates y' versus the a-Si layer thickness. Symbols represent the Ge concentration versus a-Si layer thickness, as determined from the (004) and (311) diffraction peaks. The equilibrium Ge concentration of the $\text{Ti}(\text{Si}_{1-y}\text{Ge}_y)_2$ compound is 0.09 for this substrate, and is indicated by the dashed line..... 75

Figure 3.11: Plot of amorphous silicon layer thickness and ratio of Ti and a-Si layer thickness vs. germanium concentration of $\text{Si}_{1-x}\text{Ge}_x$ substrate at 600°C, 700°C, and 800°C. Solid lines indicate the a-Si layer thickness predicted to equilibrate to the equilibrium concentration (x) for a 300 Å layer of Ti. The dashed lines indicate the ratio of Ti to a-Si needed to equilibrate to a specific substrate germanium concentration (x) at 600°C, 700°C, and 800 °C for any Ti layer thickness..... 76

Figure 4.1: Layered structure after deposition and subsequent phase formation after annealing, which results in the interlayer inversion and epitaxial CoSi_2 adjacent to the substrate..... 86

Figure 4.2(a): x-ray diffraction data for Ti diffusion barrier samples. Values for 2θ range between 25-75°..... 88

Figure 4.2(b): x-ray diffraction data indicating the formation of CoSi_2 (400) and $\text{Si}_{0.8}\text{Ge}_{0.2}$ (400). The $\text{Si}_{0.8}\text{Ge}_{0.2}$ substrate peak is located at $\sim 68.00^\circ$, while the peak corresponding to the formation of epitaxial CoSi_2 is located at $\sim 70.80^\circ$. In addition, the Si (400) $K\alpha_1$ and $K\alpha_2$ lines are located at 69.13° and 69.33° , respectively..... 89

Figure 4.3 (a)-(e): SEM micrographs of sample surface for interlayers of 10, 30, 50, 70, and 100 Å, from left to right, which reveal the surface of the CoSi_2 film, and the existence of the layer inversion by-products on the surface of the CoSi_2 film..... 91

Figure 4.4: Co K-edge XANES spectra.....	93
Figure 4.5: Ti K-edge XANES spectra.....	94
Figure 4.6: Comparison of XANES data from x-ray absorption at the Ti K edge and fits to the data, assuming that the signal from each sample is a linear combination of signals from TiO_2 , Ti_5Si_3 , and TiSi_2 reference standards. The actual data for each sample is indicated by the solid line, while the fit to the data is indicated by the dashed line.....	95
Figure 4.7: AES scans of inter-layered samples after annealing at 700 °C for 15 minutes.	96
Figure 4.8: AES spectra of 50 Å diffusion barrier sample before annealing and after annealing at 700 °C for 15 minutes.	97
Figure 4.9: Fraction of silicide formation as a function of diffusion barrier thickness.	101

1. Introduction

Transition metals have been commonly used as a means to form metal contacts for silicon based semiconducting devices. These metals can be classified as being either refractory, found in group IV_b (Ti, Zr, Hf), group V_b (V, Nb, Ta), group VI_b (Cr, Mo, W), or as near-noble, found in group VIII (Co, Ni, Pt, Pd) of the periodic table. In the solid phase reaction of metals from groups IV_b, V_b, and VI_b with silicon, the final metal silicide phase that forms is a silicon-rich one, having a composition MSi₂ (M = refractory metal) and one of four crystal structures: C11_b (tetragonal), C40 (hexagonal), C49 (body-centered orthorhombic), and C54 (face-centered orthorhombic). These structures are similar in that they contain metal-silicon layers, where each metal atom is surrounded by 6 silicon atoms, as shown in figure 1.1, but vary from each other in that the layers are arranged in a particular alternating sequence according to polytype, as shown for the two most common polytypes in figure 1.2.

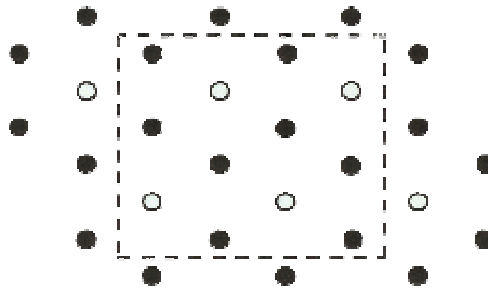


Figure 1.1: Arrangement of metal and semiconducting atoms in the stacking planes of the C11_b, C40, C49, and C54 crystal structures. The metal atoms are indicated by the open circles, which are surrounded by six semiconductor atoms, which are indicated by the solid circles. The in-plane lattice directions in the C11_b, C49, and C54 structures are along the directions of the sides of the dashed box shown in the figure. Reprinted from Ref. [1].

Other transition metals, like cobalt, nickel, platinum, and palladium do not crystallize in the C11_b, C40, C49, and C54 structures in the solid phase reaction with silicon, but in the C1 for Co silicide, the B31 and C1 for the nickel silicides, and the C22 and B31 structures for both Pt and Pd silicides. These silicides are not characterized by stacking planes of metal atoms surrounded by silicon atoms as in the case of the refractory metals.

Most of the transition metals also form metal germanides upon reacting with germanium, and exhibit germanium-rich germanide phases which are in some cases structurally isomorphic to the MSi₂ phase. In the cases where an isomorphism exists between a metal silicide and a metal germanide, a refractory metal-germanosilicide solid phase can be formed. This isomorphism allows control over the physical and chemical properties of the metal-germanosilicide by varying the concentration of Si and Ge atoms in the lattice. A list of transition metal silicide and germanide compounds, detailing their terminal phase and crystal structure can be found in Table 1.1.

Of the many metal silicide or metal germanide phases which could form in a metal-silicide (germanide) solid phase reaction, the most relevant in terms of their contribution to technological advancement are CoSi₂ and the C54 phase of TiSi₂. Both phases are currently being used in the current VLSI manufacturing process as a metal silicide contact to source/drain and gate regions, however, the C54 phase is more widely used.

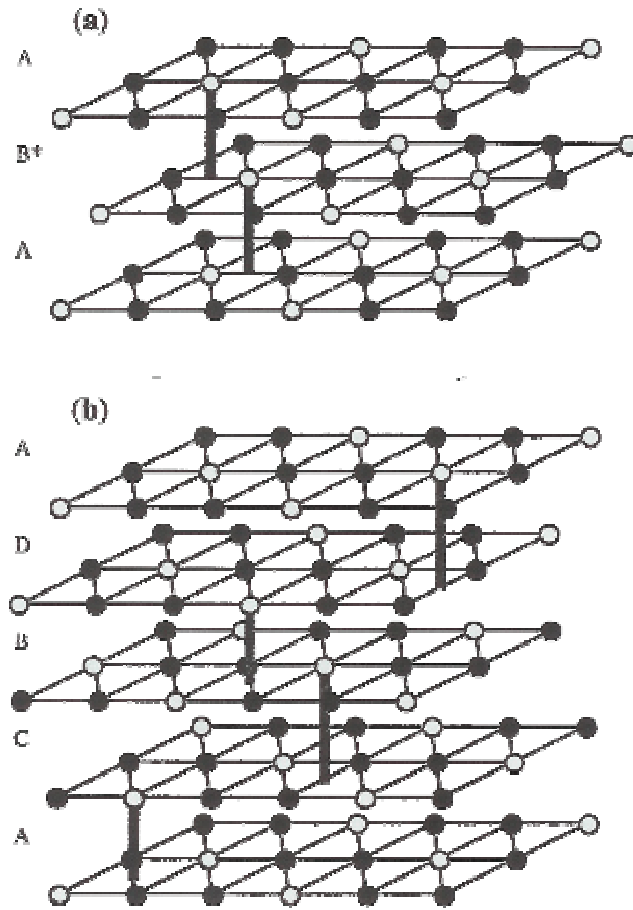


Figure 1.2: The layer stacking sequence for the C49 (a) and C54 (b) phases. The dark vertical lines indicate the alignment of the layers. The C49 structure (a) is characterized by a A-B* stacking sequence, where the metal atoms in each layer are located above adjacent semiconductor and metal atoms, while the C54 structure (b) is characterized by an A-B-D-C stacking sequence, where the metal atoms are located above adjacent semiconductor atoms. Reprinted from Ref [1].

CoSi₂ is seen as a more viable option in the formation of these contacts, as its resistivity is comparable to that of TiSi₂, its high thermal stability, and small lattice mismatch with silicon. The Si (100) orientation is seen as more desirable than Si (111) for CoSi₂ metallization in the fabrication of a metal based transistor (MBT), due to the absence of electronic states in the silicide available for the injection of electrons at the energy of the conduction band minima for Si (111), which are available in Si (100) [36, 37, 38], making it advantageous to establish CoSi₂ epitaxy to Si (100). The epitaxy of CoSi₂ on Si (111) has been achieved; however, epitaxial CoSi₂ on Si (100) is accompanied by (110) oriented CoSi₂ grains contained within the epitaxial layers [41].

Recent advances in technology now permit the use of a Si_{1-x}Ge_x layer instead of Si at the contact regions. The fact that Si_{1-x}Ge_x has a tunable bandgap which can be altered by varying the Si/Ge atom ratio, allows for fast switching speeds, low current drain, low noise, and low power consumption [43,44,45,46]. Developing metallization schemes to form viable contacts requires a knowledge of the solid phase reactions between the refractory metals most commonly used in manufacturing processes and Si-Ge .

Refractory Metal	Final Silicide		Final Germanide	
	Phase	Structure	Phase	Structure
Titanium	TiSi ₂	C54	TiGe ₂	C49
Zirconium	ZrSi ₂	C49	ZrGe ₂	C49
Hafnium	HfSi ₂	C49	HfGe ₂	C49
Vanadium	VSi ₂	C40	VGe ₂	C40
Niobium	NbSi ₂	C40	NbGe ₂	C40
Tantalum	TaSi ₂	C40	TaGe ₂	C40
Chromium	CrSi ₂	C40	---	---
Molybdenum	MoSi ₂	C11 _b	MoGe ₂	C23
Tungsten	WSi ₂	C11 _b	WGe ₂	C11 _b
Cobalt	CoSi ₂	C1	CoGe ₂	C _e
Nickel	NiSi	B31	NiGe	B31
	NiSi ₂	C1	---	---
Platinum	Pt ₂ Si	C22	Pt ₂ Ge	C22
	PtSi	B31	PtGe	B31
	PtSi ₂	B31	PtGe ₂	C35
Palladium	Pd ₂ Si	C22	Pd ₂ Ge	C22
	PdSi	B31	PdGe	B31

Table 1.1: Composition and structure of terminal refractory silicide and germanide phases. The silicide and germanide phases of Ni, Co, Pt, and Pd do not exist in the C54, C11_b, C40, or C49 structures, but their respective structures are listed.

1.1 Technical Motivation

At this time, VLSI schemes have been implemented, which employ doped Si as the semiconducting material at the gate, source, and drain regions of a transistor. However, $\text{Si}_{1-x}\text{Ge}_x$ inclusion has been shown to enhance device performance, and has been demonstrated in the fabrication of MOSFET [35] devices.

A $\text{Si}_{1-x}\text{Ge}_x$ layer pseudomorphically strained on a Si substrate exhibits a greater hole mobility as compared to that of Si, leading to an enhanced conduction channel as compared to Si for p-channel MOSFETs [43]. Improvements in electron mobility of up to 80% have been shown in Si layers under tensile stress which have been grown on relaxed $\text{Si}_{1-x}\text{Ge}_x$ “virtual” substrates, giving rise to a two-fold increase in the switching speed of a device with a strained Si conduction channel as compared to that of a conventional n-channel MOSFET. In addition, B-doped poly- $\text{Si}_{1-x}\text{Ge}_x$ gates can be employed in p-channel MOSFET structures and be used to fine tune the threshold voltage, as heavily B-doped $\text{Si}_{1-x}\text{Ge}_x$ is characterized by a variable work function which ranges from that of pure Si (5.17 eV) to that of pure Ge (4.66 eV). Finally, the introduction of B in epitaxial $\text{Si}_{1-x}\text{Ge}_x$ films reduces compressive strain as well as allow for above equilibrium doping levels, which allows the formation of ultra-shallow, low-resistivity source-drain regions. Schematic MOSFETs illustrating these device structures are shown in figures 1.3 (a), (b), (c), and (d).

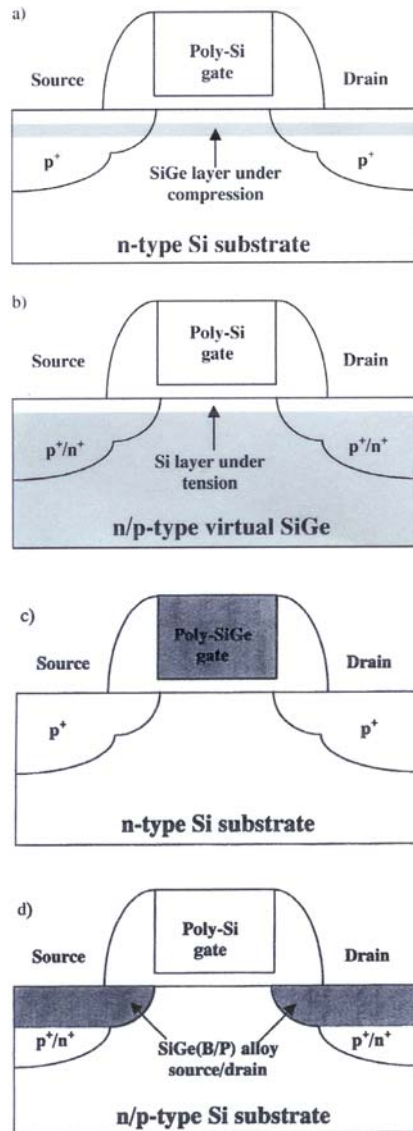


Figure 1.3: Schematic MOSFET structures which indicate where $\text{Si}_{1-x}\text{Ge}_x$ alloys can be incorporated to enhance device performance. (a) A compressively strained conduction channel, (b) Si conduction channel under tensile strain from a “virtual” $\text{Si}_{1-x}\text{Ge}_x$ substrate, (c) tunable poly- $\text{Si}_{1-x}\text{Ge}_x$ gate electrode, (d) ultra-shallow $\text{Si}_{1-x}\text{Ge}_x$ source-drain extensions. Reproduced from Ref. [43].

Device performance is dependent on establishing low resistivity metal silicide and metal germanosilicide contacts to the source, gate, and drain regions to facilitate the transfer of electrical current to and from a device. The method of forming these contacts is known as the self-aligned silicide (SALICIDE) process.

1.2 SALICIDE Process

The issues which are of concern when considering an implementation of the SALICIDE process are the reactivity and diffusivity of the transition metal in Si, oxidation, and thermal stability of the metal silicide phase formed. Both CoSi_2 and the C54 phase of TiSi_2 are attractive due to their high thermal stability and low resistivity, with CoSi_2 having the further advantage of a smaller lattice mismatch and cubic structure, implying that epitaxial CoSi_2 films could be easily grown.

A basic review of the SALICIDE process as it applies to the fabrication of MOSFET devices using Ti as the metal contact will be given as discussed in Ref. 48. The process is similar for devices using Co as the contact material [50]. Starting with a complementary metal-oxide-semiconductor (CMOS) device structure, whose exposed polysilicon gate and doped source/drain regions have been made contamination free, Ti is deposited and is allowed to react in a nitrogen ambient, forming a C49 metal silicide. This is also accompanied by the formation of a TiN layer on the surface of the silicide layer. After a selective etching to remove unreacted metal and the metal nitride layer, and “self-align” the silicide, further heat treatments are needed to acquire the low resistivity C54 phase.

Of great importance for functional device structures is the thermal stability of the metal silicide in the contact regions, which is found to be a function of annealing

temperature, annealing ambient, surface and interfacial energies, grain size, and film thickness [1].

For sufficiently high annealing temperatures during the Ti salicidation process, Si can diffuse through the silicide and precipitate at the metal silicide grain boundaries [1]. Higher annealing temperatures tend to cause the metal silicide films to agglomerate, resulting in a discontinuous metal silicide layer. This, in turn, leads to contacts with a very high resistivity, and also to eventual device degradation.

The annealing ambient plays a key role in metal silicide contact formation. The most common annealing ambient is N₂. The presence of nitrogen serves to block the diffusion of Si atoms into the Ti grain boundaries, thereby reducing diffusion of Si on the Ti surface [1]. This has been found to prevent the occurrence of “bridging”, an effect associated with the diffusion of Si over the isolation regions, where it can react with Ti and form TiSi₂ filaments between the source, gate, and drain areas, providing an electrical connection. As Co is the major diffusing species in the Co/Si solid phase reaction, the problem of Si diffusion through the isolation regions of the transistor during the formation of CoSi₂ contacts in the SALICIDE process are minimized, due in part to the fact that during the formation of the Co silicide, Si is the major diffusing species only during the formation of CoSi, and would grow laterally over the oxide region. However, this CoSi overgrowth could be selectively etched away before the final annealing step. This would eliminate the occurrence of “bridging” between the gate and source/drain regions, another feature which makes Co salicidation a more viable option in the formation of contacts [33].

The grain boundary grooving model, originally proposed by Mullins [32], relates the thermal groove depth between metal silicide grains to the temperature, the interfacial energy between the metal silicide and Si regions (gate, source, drain), groove angle, and diffusion of Si in TiSi_2 . According to the model, silicide agglomeration occurs when the groove depth is equal to the thickness of the silicide film.

It has also been observed that the silicide film thickness affects the occurrence of agglomeration. Thinner films mean that less material transport is required for the grooving phenomena to have a profound effect. Congruently, a decrease in film thickness is related to a decrease in agglomeration temperature [1].

The formation of device structures in the SALICIDE process becomes more complicated with the incorporation of Si-Ge alloys at the gate and source/drain regions, instead of Si. In addition to the concerns raised during the formation of contacts on Si, other issues arise. In particular, since both Si and Ge have similar crystal structures and similar electronic properties, Si-Ge solid solutions can be formed which vary in composition from $0 \leq x \leq 1.00$, where x is the concentration of Ge by atomic fraction.

One of the major concerns related to the metallization of Si-Ge is the thermodynamic stability at the interface between the metal silicide or metal germanosilicide and Si-Ge substrate. In some cases, stability at the interface can be achieved by the formation of precipitate material at the surface of the film or within the film grain boundaries. For both the Ti-Si-Ge and Co-Si-Ge solid phase reactions, the precipitate formation is mediated by differences in the free energies of formation

between metal silicide and metal germanide phases, as well as kinetic considerations related to the availability of Si and Ge during the phase formation sequence.

1.3 Solid Phase Reactions

1.3.1 Titanium-Silicon Solid Phase Reaction

The formation of titanium silicides from the solid state Ti-Si reaction are controlled by both nucleation and diffusion processes. During the reaction sequence, an amorphous Ti-Si layer initially forms at the Ti/Si interface at $\sim 400^\circ\text{C}$, due to the inter-diffusion of both Si and Ti atoms. Continued diffusion of Si atoms into the a-TiSi region permits the nucleation of the C49 phase of TiSi_2 , and a further increase in temperature is accompanied by the lateral growth of C49 TiSi_2 across the a-TiSi/Si interface. The vertical growth of the C49 layer occurs until all of the Ti is consumed. The C49 TiSi_2 phase has a base-centered orthorhombic crystal structure, with lattice constants of $a=3.62 \text{ \AA}$, $b=13.76 \text{ \AA}$, and $c= 3.61 \text{ \AA}$.

A polymorphic transformation occurs at higher annealing temperatures, as the C49 crystal structure converts to that of a face-centered orthorhombic C54 structure, with lattice constants of $a=8.26 \text{ \AA}$, $b=8.55 \text{ \AA}$, and $c= 4.79 \text{ \AA}$. The polymorphic transformation is driven by a difference in the bulk free energy of the two phases. Additional increases in the annealing temperature eventually leads to the agglomeration of the C54 TiSi_2 film, which has been shown to occur due to thermal grooving along the grain boundaries of the film, and has been modeled in terms of a balance of interfacial and surface energies [32].

It has been reported that the formation of titanium silicides, which leads to the formation of the final phase of TiSi_2 occurs in four stages: inter-diffusion, C49

formation, C49 \rightarrow C54 transformation, agglomeration. The polymorphic C49 \rightarrow C54 transformation, driven by a difference in the bulk free energy between the two structures, has been seen to occur at higher temperatures, due to the fact that the higher temperatures help the C49 phase overcome the nucleation barrier to C54 formation. In addition, this nucleation barrier is affected by the misfit strain created by the nucleation of C54 TiSi₂, and differences in the interfacial energies of the substrate and the C49 and C54 grains [1].

The equilibrium shape of C54 TiSi₂ grains has been found to be a function of surface and interface energies at the C54 TiSi₂ surface, the Si surface, and the C54 TiSi₂/Si interface [1,2,3,4]. Further annealing at higher temperatures may cause the C54 grains to separate (agglomeration).

Other factors have been shown to influence the C49 \rightarrow C54 transformation, such as the film thickness and line widths. It was reported [2,3] that the C49 \rightarrow C54 transformation temperature increased as the film thickness decreased, due to the fact that the surface-to-volume ratio of C54 nuclei increased as the thickness is decreased, thereby increasing the C54 nucleation barrier. Thus, more energy is required in these cases to complete the C49 \rightarrow C54 polymorphic transformation [1,2,3]. The effects of reduced line widths are the reduction of available sites for the nucleation of the C54 phase, which becomes critical for submicron lines [47].

1.3.2 Titanium-Germanium Solid Phase Reaction

The solid state reaction of Ti and Ge results in the formation of titanium germanide compounds. The reaction has been characterized by Thomas *et. al.* [6], and

it was found that at temperatures below 400°C, the reactivity between Ti and Ge is small, however, when the temperature reached between 450-500°C, the formation of a Ti-rich Ti_6Ge_5 compound is observed. The films exhibited a mirror-like appearance, and the reaction progressed slowly, indicative of a diffusion controlled reaction. At a temperature of 500°C, all of the Ti had been consumed in the reaction, and there was no change in the films up to a temperature of 560°C. An increase in temperature to 580°C reveals the existence of a mixed composition Ti-Ge phase, as if the film assumed some composition that was intermediate between Ti_6Ge_5 and TiGe_2 . At 600°C, the film had been completely transformed into C54 TiGe_2 . The growth of the Ti_6Ge_5 film and the nucleation and lateral growth of TiGe_2 from Ti_6Ge_5 suggest that the formation of TiGe_2 in the solid state Ti-Ge reaction is both diffusion and nucleation controlled.

The formation temperatures of the C49 and C54 TiSi_2 phases are within the range of temperatures required for the formation of Ti_6Ge_5 and C54 TiGe_2 . Also, the existence of the C49 phase of TiGe_2 has not been observed during the Ti-Ge solid phase reaction. However, the C49 phase of TiGe_2 had been observed by Hong, *et. al.*[1, 7] during the crystallization of a co-deposited Ti+2Ge amorphous layer. The C49 \rightarrow C54 transformation temperature was also observed to be 100°C lower than that for the C49 \rightarrow C54 TiSi_2 transformation.

1.3.3 Ti-Si_{1-x}Ge_x Solid Phase Reaction

The formation of both titanium silicides and titanium germanides has been documented [1, 6, 7]. Both Si and Ge crystallize in a diamond structure, and both

elements are completely miscible. The solid state reaction between Ti deposited on a $\text{Si}_{1-x}\text{Ge}_x$ substrate has been studied by Aldrich, *et. al.* [1,8], and it was found that the reaction paths which lead to the formation of a $\text{Ti}(\text{Si}_{1-y}\text{Ge}_y)_2$ layer on the substrate varied, depending on the concentration of Ge atoms (x) in the substrate. The study employed two different types of samples, where the nucleation temperature, morphology, and thermal stability of the $\text{Ti}(\text{Si}_{1-x}\text{Ge}_x)_2$ films were investigated in ultra-high vacuum (UHV) to minimize contamination. Other samples were annealed for 10 seconds by rapid thermal annealing (RTA) to study the effects of annealing duration on phase formation.

For substrates in which $0 \leq x \leq 0.33$, the reaction followed a “Ti-Si like” reaction path, which could be explained by examining the Ti-Si solid phase reaction. For substrates in which $0.66 \leq x \leq 1.00$, the reaction followed a “Ti-Ge like” reaction path, analogous to that in the Ti-Ge solid phase reaction. For those substrates with intermediate compositions, in which $0.37 \leq x \leq 0.66$, the formation of a Ti_6M_5 phase ($\text{M}=\text{Si}_{1-x}\text{Ge}_x$) was observed, which was followed by the formation of C49 and C54 $\text{Ti}(\text{Si}_{1-x}\text{Ge}_x)_2$ phases at higher temperatures.

It was also determined that the relative nucleation barriers for titanium germanosilicide formation during various stages of the Ti- $\text{Si}_{1-x}\text{Ge}_x$ solid phase reaction could be estimated as a function of Ge concentration. During annealing, the first phases to form are either C49 $\text{Ti}(\text{Si}_{1-x}\text{Ge}_x)_2$ or Ti_6M_5 . It was found that the relative nucleation barrier for C49 $\text{Ti}(\text{Si}_{1-x}\text{Ge}_x)_2$ crystallization increased with increasing Ge content, while the relative nucleation barrier for Ti_6M_5 crystallization decreased with increasing Ge content. The relative nucleation barrier for the

formation of both C49 and C54 $\text{Ti}(\text{Si}_{1-x}\text{Ge}_x)_2$ from Ti_6M_5 was found to increase with increasing Ge content, while the relative nucleation barrier for C54 $\text{Ti}(\text{Si}_{1-x}\text{Ge}_x)_2$ formation from C49 $\text{Ti}(\text{Si}_{1-x}\text{Ge}_x)_2$ was found to decrease with increasing Ge content.

In another study by Aldrich *et.al.*, [9], the effect of film thickness in the formation of $\text{Ti}(\text{Si}_{1-x}\text{Ge}_x)_2$ in the $\text{Ti}-\text{Si}_{1-x}\text{Ge}_x$ solid phase reaction was examined. The nucleation of C54 $\text{Ti}(\text{Si}_{1-x}\text{Ge}_x)_2$ from C49 $\text{Ti}(\text{Si}_{1-x}\text{Ge}_x)_2$ was found to be delayed in thinner films as compared to thicker films due to increased thermal grooving and agglomeration, which decreases the number of C54 nucleation sites. In addition, the formation of Ge-rich Si-Ge precipitates were also found to influence the C49 \rightarrow C54 transformation, as the presence of the precipitates within the grain boundaries could also reduce the number of available C54 nucleation sites.

The interfacial stability of $\text{Ti}(\text{Si}_{1-y}\text{Ge}_y)_2$ compounds on $\text{Si}_{1-x}\text{Ge}_x$ was also examined by Aldrich *et.al.* [8,10,12]. In one study [10], the interfacial stability of C54 $\text{Ti}(\text{Si}_{1-y}\text{Ge}_y)_2$ on $\text{Si}_{1-x}\text{Ge}_x$ samples during long (10 min.) and short (10 sec.) anneals at different temperatures in UHV (long anneals) and RTA (short anneals) indicated the formation of C54 $\text{Ti}(\text{Si}_{1-y}\text{Ge}_y)_2$, in addition to the formation of Ge-rich Si-Ge precipitates. It was found that during the initial stages of phase formation, the C54 film contained the same ratio of Si/Ge atoms as that of the substrate. However, with continued annealing a decrease in the Ge concentration in the C54 layer was observed. As both Si and Ge atoms diffuse from the substrate in to the C54 layer, a Gibbs free energy difference between TiSi_2 and TiGe_2 compounds leads to the replacement of Ge with Si atoms on the C54 lattice. Excess Ge is released in the form

of precipitates within the C54 grain boundaries. This process occurs until the C54 layer is in equilibrium with both the substrate and precipitate layers.

In other studies by Aldrich *et.al.*, [10, 12] the interfacial stability at the $\text{Ti}(\text{Si}_{1-y}\text{Ge}_y)_2/\text{Si}_{1-x}\text{Ge}_x$ interface had been examined by invoking a Gibbs free energy model, parameterized in terms of the Ge atomic concentration. The observation of thermodynamic instabilities in the $\text{Ti}(\text{Si}_{1-y}\text{Ge}_y)_2/\text{Si}_{1-x}\text{Ge}_x$ reaction, in the form of Ge-rich Si-Ge precipitates which were found to form in both the C49 and C54 phases, were analyzed by considering the thermodynamic equilibrium between equal molar amounts of both a $\text{Ti}(\text{Si}_{1-y}\text{Ge}_y)_2$ equilibrium compound and a $\text{Si}_{1-x}\text{Ge}_x$ solid solution. This information was used in order to describe the thermodynamic and kinetic effects which come into play during the Ti- $\text{Si}_{1-x}\text{Ge}_x$ solid phase reaction, and used to explain precipitate formation as a means for the $\text{Ti}(\text{Si}_{1-y}\text{Ge}_y)_2$ film to minimize its free energy to match the composition required for it to be in equilibrium with the bulk substrate. In addition, the free energy model was described in terms of a ternary phase diagram for this system. The thermodynamic stability of the $\text{Ti}(\text{Si}_{1-y}\text{Ge}_y)_2/\text{Si}_{1-x}\text{Ge}_x$ system for substrate compositions $x = 0.10, 0.20, \dots, 0.90$ at 700°C is depicted in Figure 1.4. The line from Si to Ge defines the $\text{Si}_{1-x}\text{Ge}_x$ solid solution, while the line from TiSi_2 to TiGe_2 defines the $\text{Ti}(\text{Si}_{1-y}\text{Ge}_y)_2$ equilibrium compound. Since the solid solubility of Ti in Si, Ge, or any $\text{Si}_{1-x}\text{Ge}_x$ alloy is very small, the width of the line from Si to Ge is assumed to be very small. The line extending from TiSi_2 to TiGe_2 is also assumed to have a small width, although in reality it should have a finite thickness [10, 12]. According to the phase rule [49], in a ternary system at constant temperature and pressure in any two-phase domain, any one phase with a specific composition can

only be in equilibrium with another phase of a specific composition. This is indicated in the ternary phase diagram by the dashed lines which connect a $\text{Ti}(\text{Si}_{1-y}\text{Ge}_y)_2$ and $\text{Si}_{1-x}\text{Ge}_x$ phase in equilibrium.

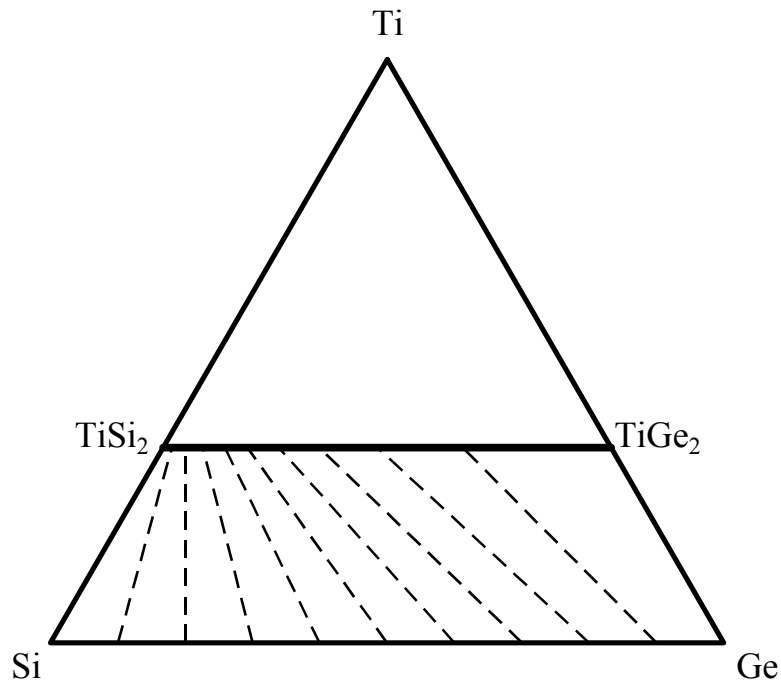


Figure 1.4: Ti-Si-Ge ternary phase diagram at 700°C, indicating stability between $\text{Ti}(\text{Si}_{1-y}\text{Ge}_y)_2$ film and $\text{Si}_{1-x}\text{Ge}_x$ substrate for compositions $x = 0.10, 0.20, \dots, 0.90$.

When considering the occurrence of precipitates at the C54 grain boundaries, the equilibrium compositions of the Si-Ge precipitate and $\text{Ti}(\text{Si}_{1-y}\text{Ge}_y)_2$ film were determined by considering the C54 phase formation sequence and the concentration of the C54 phase during the early stages of formation. During the early stages, the concentration of Ge atoms in both the film and substrate are equal, i.e., $y \sim x$.

Differences in the diffusion of Si and Ge atoms in both the substrate and $\text{Ti}(\text{Si}_{1-y}\text{Ge}_y)_2$ film, which have been related to differences in electronegativity and work function between Ti, Si, and Ge atoms by Freiman, *et.al.* [11], in addition to chemical driving forces which seek to find the configuration of atoms with the lowest total free energy, are then used to determine both the initial concentration of the precipitate formed when $y \sim x$, and also the final concentration of the $\text{Ti}(\text{Si}_{1-y}\text{Ge}_y)_2$ film in equilibrium with the $\text{Si}_{1-x}\text{Ge}_x$ substrate, which is assumed to be in infinite availability.

The effects of Ge segregation on the final phase formation can then be determined, as well as the evolution of the system towards equilibrium, which can be described as a decrease in the Ge concentration of the $\text{Ti}(\text{Si}_{1-y}\text{Ge}_y)_2$ film from its initial value y to y^* , the concentration of the $\text{Ti}(\text{Si}_{1-y}\text{Ge}_y)_2$ film that is in equilibrium with the substrate, and also a transformation from the existence of a Ge-rich Si-Ge precipitate with Ge concentration index z where $z > x$, to a precipitate where $z = x$. At this stage, the interfaces are in thermodynamic equilibrium and the precipitation phenomena ceases.

1.3.4 Co-Si Solid Phase Reaction

The formation of cobalt silicides in the Co-Si solid phase reaction has been extensively studied [14-25]. The formation of the various cobalt silicide phases are thought to be controlled by both diffusion and nucleation processes. The formation of CoSi_2 is preceded by the formation of a least one Co-rich silicide, Co_2Si . This occurs at temperatures in the range of 200-300°C during the first diffusion process, when Co is the major diffusing species. The entire layer of Co is eventually converted to a polycrystalline Co_2Si layer. During the second diffusing stage which occurs around

400°C, when Si is the major diffusing species, the Co_2Si layer is eventually converted to polycrystalline CoSi. The third and final diffusing stage, which occurs around 600 °C results in the nucleation of CoSi_2 at the Si-CoSi interface, and the diffusion of Co continues until the entire silicide film is converted to CoSi_2 . CoSi_2 exists in the cubic CaF_2 structure, with lattice constant $a=5.364 \text{ \AA}$ [40].

Due to its low lattice mismatch and cubic crystal structure [37, 38, 39] it is expected that the formation of epitaxial CoSi_2 on Si would be readily achieved. The growth of epitaxial CoSi_2 on Si (111) has been reported. However, from a device standpoint, epitaxy to Si (100) would be most favorable. The direct formation of epitaxial CoSi_2 on Si (100) through the Co-Si solid phase reaction is also associated with the presence of misoriented CoSi_2 grains. The problem was examined by Bulle-Lieuwma, *et.al.* [24], who concluded that this phenomena was attributable to the possibility of simultaneous epitaxy of multiple CoSi_2 orientations on Si (100).

1.3.5 Co- $\text{Si}_{1-x}\text{Ge}_x$ Solid Phase Reaction

The planned incorporation of $\text{Si}_{1-x}\text{Ge}_x$ in CMOS technologies, coupled with the advantages of cobalt silicides, prompts a study of the Co- $\text{Si}_{1-x}\text{Ge}_x$ solid phase reaction. The reaction has been studied by Z. Wang, *et.al.*, [27] and it was found that a cubic $\text{Co}(\text{Si}_{1-y}\text{Ge}_y)$ phase, isomorphic to CoSi, formed at around 400°C, which eventually transformed to CoSi_2 at 700°C. This was also accompanied by the formation of Ge precipitates on the surface of the CoSi_2 film. The phase formation sequence has been studied by Goeller [26], and was modeled by considering a chemical driving force for the formation of CoSi_2 after the expulsion of Ge from the $\text{Co}(\text{Si}_{1-y}\text{Ge}_y)$ phase and the reaction of the newly-formed CoSi with the $\text{Si}_{1-x}\text{Ge}_x$

substrate. This leads to further Ge expulsion, and the formation of a Ge-rich Si-Ge precipitate. Reports of the formation of a $\text{Co}_2(\text{Si}_{1-y}\text{Ge}_y)$ phase prior to $\text{Co}(\text{Si}_{1-y}\text{Ge}_y)$ phase have not been found in the literature, however, one can expect this to occur due to the diffusion of Co into the $\text{Si}_{1-x}\text{Ge}_x$ layer at low temperature, as in the case of the Co-Si solid phase reaction.

1.3.6 Co-Ti-Si Solid Phase Reaction

The Co-Si solid phase reaction has been extensively studied, and CoSi_2 epitaxy on Si (111) is readily achieved. However, epitaxy to Si (100) remains difficult. One means of achieving epitaxy to Si (100) is to incorporate a layer of titanium between the Si substrate and Co layer, in a process which is commonly known as titanium interlayer mediated epitaxy (TIME) [28, 20, 17]. The layer of titanium is thought to remove the native oxide from the Si surface, in addition to providing a barrier to control the diffusion of Co atoms, thereby controlling the formation of the various cobalt silicide phases which occur and lead to the formation of CoSi_2 .

In a study by Vantomme, *et.al.* [41], the role of the annealing ambient in the formation of epitaxial CoSi_2 on Si (100) was discussed. The Co-Ti-Si solid phase reaction was carried out in the presence of N_2 , $\text{N}_2 + 5\% \text{H}_2$, $\text{He} + 14\% \text{H}_2$, and in UHV. It was determined that annealing in a reactive ambient resulted in the inversion of the Co and Ti layers at 600°C , and the formation of epitaxial CoSi_2 adjacent to the Si substrate. In addition, the presence of a titanium oxide compound at temperatures up to 900°C was confirmed. It was also determined that the surface roughness of the

samples varied depending on which annealing ambient was used. The UHV anneals resulted in the formation of a CoSi_x layer adjacent to the substrate, followed by a ternary Co-Ti-Si phase and a CoSi_y phase, where $y < x$, at 700°C . Further annealing up to 900°C resulted in the formation of a homogenized CoSi_2 and $\text{Co}_{0.25}\text{Ti}_{0.75}\text{Si}_2$ layer adjacent to the substrate. They also noted that inversion was incomplete in the samples annealed in UHV, and that Si was able to diffuse to the surface of these samples. It was determined from RBS measurements that the presence of the ternary Co-Ti-Si phase served to control the formation of the CoSi_x layer, by limiting the availability of Co from the uppermost CoSi_y layer.

In another study by Tung, *et.al.* [28], it was proposed that epitaxial CoSi_2 could be directly formed as the first silicide phase when the Ti diffusion barrier is employed, suggesting that somehow the presence of the diffusion barrier alone would allow the system to bypass the formation of the precursor silicides by delaying the interaction of Co and Si. However, others have proposed that the diffusion barrier does not limit the reaction, but actually controls the concentration of Co at the Co-Si interface, thereby controlling which phases form, in what is known as the concentration controlled phase selection (CCPS) process [42]. An effective heat of formation model [29, 30] was used, where the effective heat of formation is proportional to the change in the enthalpy during the reaction and the ratio between the effective concentration of Co at the reaction site and the concentration of Co in the CoSi_2 compound.

In this case, Co is seen as the limiting agent in the Co-Ti-Si solid phase reaction, due in part to its availability at the Co-Si interface, and the fact that Si is

assumed to be in infinite supply. According to the model, when its effective concentration drops below 40 at. %, the formation of CoSi_2 would be favored, since in this regime the change in the free energy is the greatest.

In contradiction with these results, others have found that the precursor silicide phases are not bypassed during CoSi_2 formation when a Ti diffusion barrier is employed. In a study by Cardenas *et.al.*, [31], it was shown that CoSi formed before the epitaxial CoSi_2 had been formed, and in another study by Barmak, *et.al.*[17], the formation of both Co_2Si and CoSi was observed to occur before CoSi_2 formation.

Many results in the literature report the formation of epitaxial CoSi_2 on Si (100) employing the TIME process. However, none report the formation of any titanium silicide phases. This implies that the Ti interlayer does not actively form its own silicide. However, the fact that TiSi_2 has a lower Gibbs free energy of formation (-134 kJ/mol) than CoSi_2 (-98.7 kJ/mol), implies that it is more thermodynamically favorable to form Ti silicides as opposed to Co silicides in the Co-Ti-Si solid phase reaction. Note however that the Co-Ti-Si ternary phase diagram indicates the stability between both CoSi_2 and TiSi_2 and a Si-rich ternary phase at 800°C, as shown in Figure 1.2, implying that both Co and Ti can form stable silicides on Si.

The role of the Ti interlayer and its promotion of the formation of epitaxial CoSi_2 on $\text{Si}_{1-x}\text{Ge}_x$ was investigated using the Co/Ti bi-layer in addition to a strained c-Si/ $\text{Si}_{1-x}\text{Ge}_x$ structure, where c-Si was deposited in the stoichiometric amount required for the formation of CoSi_2 . An XAFS and XRD study provided detailed information related to the formation of epitaxial CoSi_2 in the bi-layer reaction, and also showed that Ti plays more of a role in this reaction than previously thought.

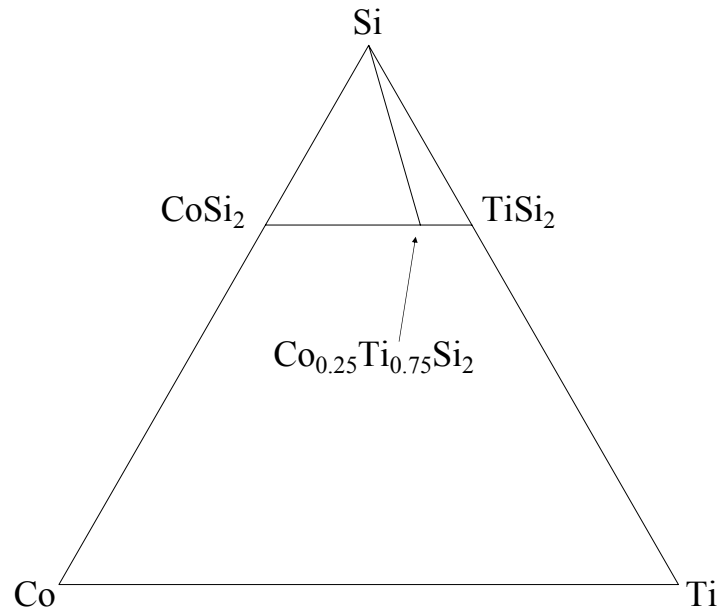


Figure 1.5: Si-rich portion of the ternary phase diagram for the Co-Ti-Si solid phase reaction at 800°C . Reproduced from information in Ref. [41].

1.3.7 Dissertation Overview

The focus of this dissertation is to examine the phase formation and stability of metal silicide and metal germanosilicide contacts to $\text{Si}_{1-x}\text{Ge}_x$ alloys. In particular, the focus was directed towards both Ti and Co metallization, which are currently used in conventional VLSI manufacturing processes and are both known to exhibit properties of low resistivity in the solid phase reaction with both Si and $\text{Si}_{1-x}\text{Ge}_x$. We propose two new methods of forming these contacts, which are based on previous results related to these systems.

The experimental methods used to characterize the growth of the metal silicide and germanosilicide thin films of this study are discussed in chapter two. The aspects of sample preparation are discussed, in addition to the thin film growth methods used. Various analytical techniques, such as AES, XAFS, XRD, and SEM, were used in these studies to obtain morphological, structural, and chemical information.

In chapter three, we examine the formation of $\text{Ti}(\text{Si}_{1-y}\text{Ge}_y)_2$ contacts to $\text{Si}_{1-x}\text{Ge}_x$. An amorphous Si interlayer is interposed between pseudomorphically strained $\text{Si}_{1-x}\text{Ge}_x$ layers before the final Ti metallization step. The role of the amorphous layer in forming a stable contact is addressed.

In chapter four, the titanium interlayer mediated epitaxy (TIME) process is examined as a paradigm for forming epitaxial CoSi_2 on $\text{Si}_{1-x}\text{Ge}_x$. The TIME process has been used previously in the formation of epitaxial CoSi_2 on Si (100), and the results are well known in the literature. Its feasibility as a viable method of forming contacts to $\text{Si}_{1-x}\text{Ge}_x$ as opposed to the use of direct deposition or templating methods is discussed.

In chapter five, a summary of the results from each experiment is given, in addition to the conclusions drawn and a plan for future work.

References

1. D.B. Aldrich, Ph.D. thesis, North Carolina State University, 1995.
2. H. Jeon, C.A. Sukow, J.W. Honeycutt, G.A. Rozgonyi, and R.J. Nemanich, *J. Appl. Phys.* **71**, 4269-4276 (1992).
3. H.J.W. van Houtum and I.J.M.M. Raaijmakers, in *Thin Films-Interfaces and Phenomena; Vol. 54*, edited by R.J. Nemanich, P.S. Ho, and S.S. Lau (Materials Research Society, Pittsburgh, PA, 1986), p. 38-42.
4. Z. Ma, Y. Xu, L.H. Allen, S. Lee, *J. Appl. Phys.* **74**, 2954-2956 (1993).
5. C.A. Sukow and R.J. Nemanich, *J. Mater. Res.* **9**, 1214-1227 (1994).
6. O. Thomas, S. Delage, F.M. d'Heurle, G. Scilla, *Appl. Phys. Lett.* **54**, 228-230 (1989).
7. Q.Z. Hong, K. Barmak, F.M. d'Heurle, *Appl. Phys. Lett.* **62**, 3435-3437 (1993).
8. D.B. Aldrich, Y.L. Chen, D.E. Sayers, R.J. Nemanich, S.P. Ashburn, and M.C. Öztürk, *J. Mater. Res.* **10**, 2849-2863 (1995).
8. D.B. Aldrich, H.L. Heck, Y.L. Chen, D.E. Sayers, and R.J. Nemanich, *J. Appl. Phys.* **78**, 4958-4965 (1995).
9. D.B. Aldrich, F.M. d'Heurle, D.E. Sayers, and R.J. Nemanich, *Phys. Rev. B*, **53**, 16279-16282 (1995).
10. W. Freiman, A. Eyal, Y.L. Khait, R. Beserman, and K. Dettmer, *Appl. Phys. Lett.* **69** 3821-3823 (1996).

11. D.B. Aldrich, F.M. d'Heurle, D.E. Sayers, and R.J. Nemanich, *Mat. Res. Symp. Proc.*, **402**, 21-26 (1996).
12. B.I. Boyanov, P.T. Goeller, D.E. Sayers, and R.J. Nemanich, *J. Appl. Phys.*, **86**, 1355-1362 (1999).
13. F.M. d'Heurle and P. Gas, *J. Mater. Res.*, **1**, 205-221 (1986).
14. F.M. d'Heurle, *J. Mater. Res.*, **3**, 167-195 (1988).
15. S.L. Hsia, T.Y. Tan, P. Smith, and G.E. McGuire, *J. Appl. Phys.*, **72**, 1864-1873 (1992).
16. K. Barmak, L.A. Clevenger, P.D. Agnello, E. Ganin, M. Copel, P. Dehaven, J. Falta, F.M. d'Heurle, and C. Cabral Jr., *Mat. Res. Soc. Symp. Proc.*, **238**, 575-580 (1992).
17. T. Barge, P. Gas, and F.M. d'Heurle, *J. Mater. Res.*, **5**, 1134-1145 (1995).
18. C. Detavernier, R.L. Van Meirhaeghe, F. Cardon, and K. Maex, *Phys. Rev. B*, **62**, 12045-12051 (2000).
19. A. Vantomme, M.A. Nicolet, G. Bai, and D.B. Fraser, *Appl. Phys. Lett.*, **62**, 243-245 (1993).
20. F. Hong, G.A. Rozgonyi, and B.K. Patnaik, *Appl. Phys. Lett.* **64**, 2241-2243 (1994).
21. Q.Z. Hong, K. Barmak, and L.A. Clevenger, *J. Appl. Phys.* **72**, 3423-3430 (1992).
22. P. Liu, B.Z. Li, Z. Sun, Z.G. Gu, W.N. Huang, Z.Y. Zhou, R.S. Ni, C.L. Lin, S.C. Zou, F. Hong, and G.A. Rozgonyi, *J. Appl. Phys.*, **74**, 1700-1706 (1993).

23. S.L. Zhang and F.M. d'Heurle in *Silicides: Fundamentals and Applications* (World Scientific, Singapore, 2000), pg. 349-358.
24. A. Alberti, L. Kappius, and F.M. d'Heurle in *Silicides: Fundamentals and Applications* (World Scientific, Singapore, 2000), pg. 359-366.
25. P.T. Goeller, Ph.D. thesis, North Carolina State University, 1999.
26. Z. Wang, D.B. Aldrich, Y.L. Chen, D.E. Sayers, and R.J. Nemanich, *Thin Solid Films*, **270**, 555-560 (1995).
27. R.T. Tung and F. Schrey, *Appl. Phys. Lett.*, **67**, 2164-2167 (1995).
28. R. Pretorius, A.M. Vredenberg, F.W. Saris, and R. de Reus, *J. Appl. Phys.*, **70**, 3636-3646 (1991).
29. R. Pretorius and J.W. Mayer, *J. Appl. Phys.* **81**, 2448-2450 (1997).
30. J. Cardenas, S. Hatzikonstantinidou, S.-L. Zhang, B.G. Svensson, and C.S. Petersson, *Physica Scripta T54* 198- (1994).
31. W.W. Mullins, *J. Appl. Phys.* **28**, 333-339 (1957).
32. L. Van den hove, R. Wolters, K. Maex, R. De Keersmaecker, and G. Declerck, *J. Vac. Sci. Technol B* **4**, 1358-1363 (1986).
33. J.C. Sturm, E.J. Prinz, and C.W. Magee, *IEEE Elec. Dev. Lett.* **12**, 303-305 (1991).
34. T.J. King, K.C. Saraswat, and J.R. Pfiester, *IEEE Elec. Dev. Lett.* **12**, 584-586 (1991).
35. S.M. Yalisove, R.T. Tung, and D. Loretto, *J. Vac. Sci. Technol.* **7**, 1472-1474 (1989).

36. S.M. Yalisove, R.T. Tung, and J.L. Bastone, *Mat. Res. Soc. Symp. Proc.* **116**, 439-445 (1988).
37. R. Stalder, C. Schwartz, H. Sirringhaus, and H. von Känel, *Surface Science* **271**, 355-375 (1992).
38. D.P. Adams, S.M. Yalisove, and D. J. Eaglesham, *J. Appl. Phys.* **76**, 5190-5194 (1994).
39. K. Maex, M. van Rossum, and A. Reader in *Properties of Metal Silicides*, edited by K. Maex and M. van Rossum, INSPEC, 3-14 (1995).
40. A. Vantomme, M.-A. Nicolet, and N.D. Theodore, *J. Appl. Phys.* **75**, 3882-3891 (1994).
41. A. Vantomme, S. Degroote, J. Dekoster, G. Langouche, and R. Pretorius, *Appl. Phys. Lett.* **74**, 3137-3139 (1999).
42. S.-L. Zhang, *Microelectronic Engineering* **70**, 174-185 (2003).
43. P.-E. Hellberg, S.-L. Zhang, H.H. Radamsson, and W. Kaplan, *Solid State Electronics* **44**, 2085-2088 (2000).
44. Y.C. Yeo, V. Subramanian, J. Kedzierski, P. Xuan, T.-J. King, J. Bokor, and C. Hu, *IEEE Electron Device Lett.* **21**, 161-163 (2000).
45. S. Verdonckt-Vandebroek, E.F. Crabbe, B.S. Meyerson, D.L. Hareme, P.J. Restle, J.M.C. Stork, and J.B. Johnson, *IEEE Trans. on Electron Devices* **41**, 90-101 (1994).
46. Z. Ma, L.H. Allen, and D.D.J. Allman, *J. Appl. Phys.* **77**, 4384-4388 (1995).
47. J.M.E. Harper, C. Cabral Jr., C. Lavoie, L.A. Clevenger, F.M. d'Heurle, L.Gignac, J. Jordan-Sweet, R.A. Roy, K.L. Saenger, G.L. Miles, R.W.

- Mann, and J. Nakos in *Silicides: Fundamentals and Applications* (World Scientific, Singapore, 2000), pg. 261-275.
48. P. Gordon in *Principles of Phase Diagrams in Material Systems* (Krieger, Malabar, FL, 1983).
49. K. Maex and A. Lauwers in *Silicides: Fundamentals and Applications* (World Scientific, Singapore, 2000), pg. 250-260.

2. Experimental

2.1 Technical Aspects

In order to characterize and thence obtain morphological and structural information related to the solid phase reaction that results in the formation of the metal silicide and metal germanosilicide compounds on $\text{Si}_{1-x}\text{Ge}_x$, various techniques were employed.

A fundamental study of these films necessitate some of the growth and characterization processes to be carried out in vacuum, hence the samples used to study the solid phase reactions were grown in ultra high vacuum (UHV), to minimize as much as possible the possibility of oxygen contamination, and the deleterious effects it has in the formation of these films. In addition, the use of pre-growth chemical etch and surface passivation treatments were required to eliminate the surface oxide found on the boron doped, Si (100) seed crystals used to grow these films.

X-ray absorption fine structure (XAFS) was used to obtain information concerning the short-range order, in addition to phase formation, of the compounds thus formed, while x-ray diffraction (XRD) was used to obtain both long-range order and phase information. Auger electron spectroscopy (AES) was used to obtain surface chemistry information, while scanning electron microscopy (SEM) was used to obtain information related to the surface morphology of the films.

2.2 Sample Preparation

The thin film samples in these studies were grown on p-type, 25mm diameter, 20 mm thick $\text{Si}(100) \pm \frac{1}{2}^\circ$ wafers, with resistivity of $8 \Omega \cdot \text{cm}^2$, obtained from Virginia Semiconductor. A pre-growth chemical treatment, consisting of a spin etch in a 1:1:10 HF: ethanol: de-ionized water solution was used in order to both hydrogen passivate and remove any native oxides from the surface of the wafers, as described elsewhere [1,2]. The samples were then placed into a loadlock of the Integrated Analysis and Processing Tool, shown in Figure 2.1. After the pressure in the loadlock chamber was less than 5×10^{-8} Torr they were transferred into a UHV solid source MBE growth chamber, which is outfitted with two e-guns that control the deposition of both Si and Ge in conjunction with a Sycon Instruments model STM-100/MF thickness/rate monitor and Sycon crystal sensors. The wafers were then annealed at 900°C in UHV for 10 minutes to thermally desorb the native oxide from the surface. A resistive element fabricated from tungsten was used for annealing, which was controlled by a programmable Eurotherm controller.

After the thermal desorption process, the wafer surface temperature was lowered to 550°C in order to deposit a 200\AA buffer layer of Si, to permit the growth of a pseudomorphically strained layer of $\text{Si}_{1-x}\text{Ge}_x$. The growth of $\text{Si}_{1-x}\text{Ge}_x$ layers in the solid source MBE of the Integrated Analysis and Processing Tool is described elsewhere [1, 2]. In most cases, the $\text{Si}_{1-x}\text{Ge}_x$ layers were grown to a thickness of 500-1000 \AA . After the growth of the $\text{Si}_{1-x}\text{Ge}_x$ layers, the samples were allowed to cool to room temperature, in order to facilitate their transfer to the e-beam metallization chamber, which is also a part of the Integrated Analysis and Processing Tool. Once in

the metallization chamber, the samples were positioned to allow the evaporated metals to condense on the sample surface. The base pressure of the e-beam metallization chamber was between $2-4 \times 10^{-10}$ Torr, while the pressure in the chamber

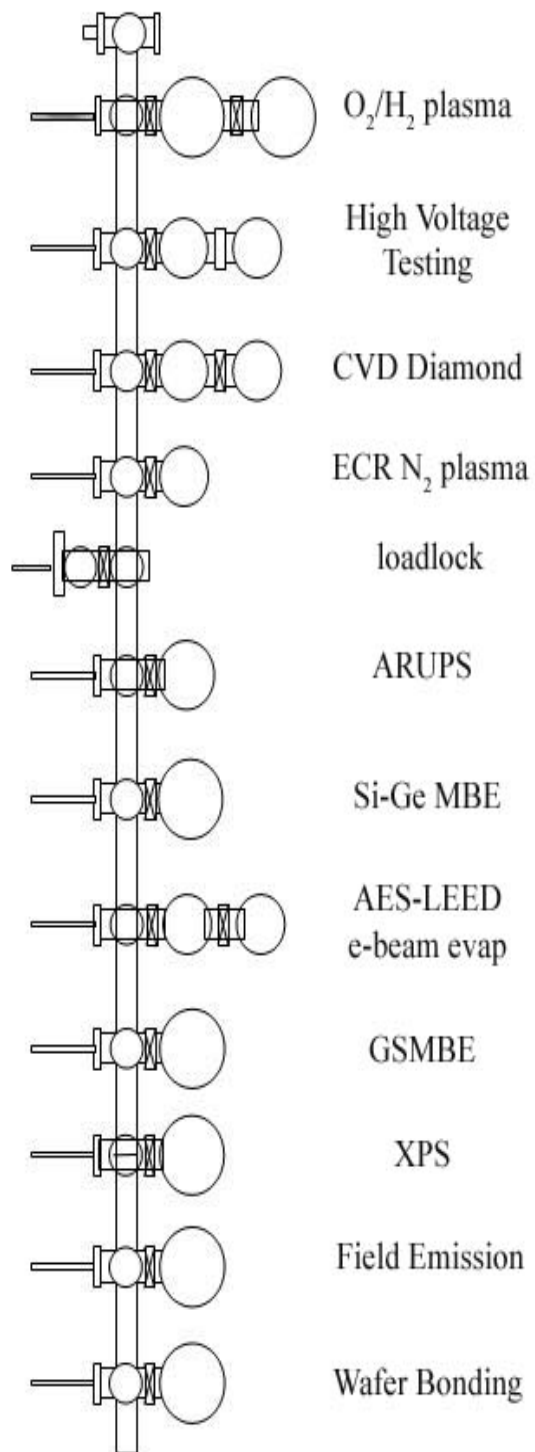


Figure 2.1: Integrated Analysis and Processing Tool.

during deposition was between $7-9 \times 10^{-10}$ Torr. The chamber contains a five-pocket e-gun for the deposition of metals. The metal deposition rate was monitored using a Sycon Instruments model STM-100/MF thickness/rate monitor and Sycon quartz crystal sensor. The metal deposition was concluded by a transfer of the sample into the solid-source MBE, whereupon the wafer was annealed in UHV between 15-20 minutes. The sample was allowed to cool to room temperature after annealing, and *in situ* characterization techniques, such as AES, were employed. After the *in situ* characterization had been completed, the sample was removed and the *ex situ* characterizations, such as XAFS, SEM, and XRD were performed.

2.3 X-ray Absorption Fine Structure

X-ray absorption fine structure, an analytical technique which gives short-range crystallographic order information, was used in these studies to obtain phase information from the various Co and Ti silicide phases formed on the $\text{Si}_{1-x}\text{Ge}_x$ substrates. Other information, such as coordination number and bond lengths can also be obtained. The phase information was determined by focusing on x-ray absorption at the Co and Ti K edges, which are 7709 and 4496 eV, respectfully.

2.3.1 Introduction

A fundamental explanation of the XAFS process has been given by Fay, *et.al.* [3] and Newville [4] and has been summarized in this work, however, a theoretical description can be found in [6].

The intensity of x-rays upon being attenuated by the presence of a medium within their path is found to be a function of the original intensity of the x-rays, the

attenuation distance, and the x-ray absorption coefficient, and is described by the equation $I=I_0e^{-\mu x}$, where I and I_0 are the intensities of the x-rays after and before absorption, μ is the x-ray absorption coefficient, and x is the attenuation distance. The relationship between the degree of x-ray absorption and x-ray incident energy allows the determination of the XAFS signal.

The XAFS principle can be understood by considering the absorption of x-rays by the core level electrons of the element of interest. An incident x-ray strikes a core level electron, and the photoelectron is ejected from the core level with energy equal to the difference in energy between the incoming photon and the energy of the electron in the core level. This photoelectron is then able to interact with other atoms that surround the absorbing atom.

During the process of absorption, the photoelectrons, which can be represented as spherical waves of wavelength λ_e , usually scatter off surrounding atoms, after which some portion of a scattered wave returns to the original location. As a result of this process, both outgoing and back-scattered photoelectrons can interact, where they can either constructively or destructively interfere with each other, and where the interaction is a function of the photoelectron wavelength and the distance between neighboring atoms. This interference leads to a modulation of the absorption cross section of the absorbing atoms, which occurs for incident x-ray energies ~ 50 eV above the absorption edge, and extends outward towards the higher end of the energy range being considered. The cross section modulation leads to the existence of oscillations in the absorption spectrum.

This oscillation in the spectrum is commonly referred to as EXAFS, or extended x-ray absorption fine structure, due to the fact that the oscillations usually occur in the extended part of the energy range under consideration. A significant amount of data analysis is required to extract structural information from these spectra, some of which involves the use of Fourier analysis.

2.3.2 The EXAFS Equation

The EXAFS signal is extracted from the absorption spectra by determining the normalized fraction of x-ray absorption by the material under consideration, which is given by the equation $\chi(E) = \frac{\mu(E) - \mu_o(E)}{\mu_o(E)}$, where $\mu(E)$ is the measured absorption at a particular wavelength, and is a function of x-ray energy, and $\mu_o(E)$ is the absorption at a particular wavelength experienced by a single atom. Since $\mu_o(E)$ cannot be measured experimentally, it is usually approximated by a smooth background function.

The expression for $\chi(E)$ is usually converted from an energy scale to a wave vector scale $\chi(E) \rightarrow \chi(k)$, since the absorption and scattering processes are wave length dependent. The conversion is straight forward, since the wave vector k of the photoelectron is related to the incident photon and photoelectron energy by the equation $k = \sqrt{\frac{2m(E - E_o)}{\hbar^2}}$, where m is the mass of the photoelectron, $E - E_o$ is the energy of the photoelectron, and \hbar is the Dirac constant.

The EXAFS equation is an expression which relates the normalized fractional absorption to structural parameters, and therefore allows the determination of

structural information from the absorption data. An expression for the EXAFS equation under the assumptions of single electron, single scattering events, and under the assumption that the amount of random disorder in the position between neighboring atoms is thermal in nature can be described by a Gaussian profile and is given by

$$\chi(k) = \sum_j \frac{N_j f_j(k) e^{-\frac{R_j}{\lambda(k)}} e^{-2k^2 \sigma_j^2}}{k R_j^2} \sin[2kR_j + \delta_j(k)] \quad (2.1)$$

where $f(k)$ is the scattering amplitude, $\delta(k)$ is the phase shift in the photoelectron wavefunction which occurs during the scattering process, N is the number of neighboring atoms, R is the distance between neighboring atoms, σ^2 is the Debye-Waller factor, which is related to the disorder in the neighbor distance, and $\lambda(k)$ is the mean free path for inelastic scattering of photoelectrons. The index j identifies the coordinate shell surrounding the absorbing atom, therefore $\chi(k)$ is just a sum of the individual sinusoidal components arising from backscattering from each coordination shell. The EXAFS equation is usually weighed by a k, k^2 , or k^3 term when plotted against the wavenumber to display the results with more uniform amplitudes as a function of k .

2.3.3 Data Collection

The XAFS data for the samples in these experiments was obtained at the National Synchrotron Light Source at Brookhaven National Labs in Upton, NY. The data was collected at beamline X-11A. X-ray absorption at the Co K edge (7709 eV) and Ti K edge (4496 eV) was used to probe the samples. The electron beam energy of the synchrotron was 2.583 GeV and the ring current varied between 110 and 240 mA.

A monochromatic x-ray beam was produced at the beamline using a Si (111) double crystal monochromator, where the suppression of higher-order harmonics was achieved by detuning the crystals. The detuning process consists of changing the voltage bias across the second monochromator crystal, causing it to bend slightly. This changes the Bragg angle relative to the first monochromator crystal which has the effect of filtering out unwanted x-ray wavelengths. A monochromator crystal detuning of 50% was used when collecting Ti K-edge absorption data, while a crystal detuning of 30% was used when collecting Co K-edge absorption data. A diagram of the experimental setup is shown in Figure 2.2. The x-ray absorption scans were taken at room temperature in the fluorescence mode, using a Canberra 13-element Ge array detector. The samples were placed in a Plexiglas sample holder, and were oriented 45° with respect to both the incoming x-ray beam and the entrance window of the 13-element detector. The sample holder was placed between the I_0 and I

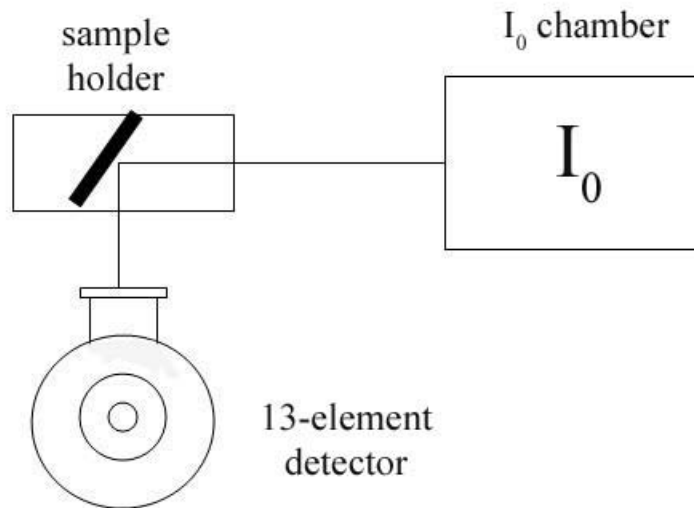


Figure 2.2: XAFS experimental layout at Beamline X11-A.

chambers (I chamber not shown), which are also used to measure XAFS signals. A steady flow of He gas was pumped into the sample holder to displace in ambient air, which would minimize scattering of the incoming x-rays, while a mixture of He and N₂ gas was pumped into the I₀ chamber. The gas mixture is ionized by the incoming x-ray beam, which gives a measure of the relative x-ray flux from the beamline.

When the x-rays leave the I₀ chamber, they become incident on the sample at an angle of 45°, as shown in figure 2.2. Some of the incident rays are elastically scattered from the sample surface, while others are absorbed by the sample. The absorbed x-rays can then generate electronic transitions within the sample of interest

which result in the production of fluorescent x-rays. The production of fluorescent x-rays and Auger electrons are both considered as competitive processes, and are generated by the decay of core holes which remain after the absorption of x-rays [6]. A fluorescent x-ray is produced when an electron from a higher energy state fills a core hole. When the core hole resides in a K shell, K_{α} fluorescent x-rays, whose energies are less than that of the incoming photons that initiated the series of electronic transitions, are produced. The production of fluorescent x-rays is depicted in figure 2.3.

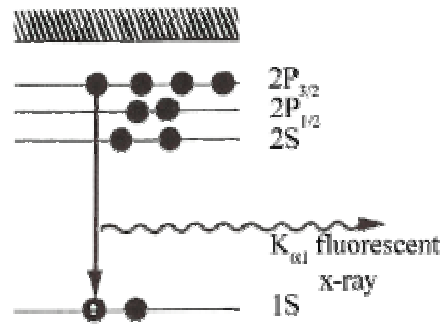


Figure 2.3: Fluorescent x-ray photon produced from an electronic transition between the $2P_{3/2}$ and $1S$ core hole states. Reprinted from Ref [6].

This results in the appearance of both elastic scattered and fluorescent x-ray signals, which are then measured by the 13-element detector. The signals from the elastically scattered x-rays are then electronically gated off from the signal of interest, such that only the fluorescent signal is obtained. The x-ray absorption of the sample can then be obtained, since the absorption is proportional to the ratio of the fluorescent and incident intensities, or $\mu(E) \propto I_f / I_0$.

The experimental set-up was mounted on a motorized stage, which is mounted on an optical bench, located in the x-ray hutch on the beamline. The signals from the 13-element detector were routed to and amplified by a separate electronics rack, and the signals were then directed to the data acquisition computer located beside the x-ray hutch. The data acquisition computer also controlled the movement of the monochromator, in addition to controlling the movements of the slits used to fine tune the amount of x-rays from the beamline and the motorized stage.

2.3.4 Data Analysis

The analysis of data proceeds as follows. Once the absorption spectra are obtained, the normalized fraction of absorption is determined from the EXAFS equation, with regards to the particular type of absorbing atom. After weighing by a power of the wavenumber, the relationship between the EXAFS equation and the wavenumber are determined, and a Fourier filtering program is used to transform from k-space to r-space, giving what is known as the radial structure function (RSF), which gives the approximate distance between the absorbing species and the neighboring atoms within a particular coordination shell. Peaks within the RSF can be isolated and back-transformed into k-space, which allows one to determine the number of atoms within a coordination shell which have contributed to backscattering. Other information can be determined as well, such as the amount of disorder in the position of the atoms involved in the absorption process, also known as the Debye-Waller factor. The determination of these parameters requires that both the scattering amplitude and the phase shifts for each absorber-scatterer pair be known in advance.

A number of data processing programs are available to analyse the data. The IFEFFIT numerical analysis library [8], developed by Bruce Ravel and Matt Newville, was used in these studies to analyze experimental data from the XAFS spectra. The package is comprised of seven graphical user interfaces (GUIs) which are able to perform deglitching, background subtraction [10], data calibration, and alignment, but also able to generate $\chi(k)$, the RSF, and determine values for fitting parameters. The IFEFFIT package operates in conjunction with FEFF and FEFFIT software routines, also written by Ravel and Newville.

Since XAFS was used more in these studies to identify phase formation and to determine the presence of mixed phases, and not to determine values for the disorder, number of atoms in a coordination shell, etc., those aspects of the process will not be considered here. However, a more thorough treatment of these aspects can be found elsewhere [1,2].

The phase identification process was carried out by comparing the near-edge features (XANES) of the XAFS spectra to the near-edge features from experimental standards of the compounds of interest. This comparison involved making a linear interpolation between the standards of some titanium silicide and titanium oxide compounds and the samples discussed in the formation of epitaxial CoSi_2 on $\text{Si}_{1-x}\text{Ge}_x$ using Ti as a diffusion barrier. The linear interpolation allowed the determination of the formation of both oxides and silicides, in addition to determining the fraction of the Ti diffusion barrier that competed with Co in forming its own silicide, which was obtained from the fit parameters. The SixPACK graphical users interface (GUI), which is part of the IFEFFIT numerical library [9], was used to perform the least

squares fitting of the XANES region, which is roughly ± 50 eV below and above the Co K absorption edge

2.4 X-ray Diffraction

X-ray diffraction has been used to obtain information concerning the long-range order and crystallographic orientation of the metal silicide and metal germanosilicide thin films grown on the $\text{Si}_{1-x}\text{Ge}_x$ substrates in this study. In addition, the technique was used to identify the silicide and germanosilicide phases found on the samples. The usefulness of the technique resides in the ability of a crystal lattice to diffract radiation whose wavelength is on the order the distance between adjacent crystal planes. The relationship between plane spacing, wavelength of incident x-rays, and diffraction angle is known as Bragg's Law, and is given by the equation $n\lambda = 2d \sin \theta$, where λ is the wavelength of the incident and diffracted x-rays, d is the spacing between diffraction planes, θ is the angle of incidence of the x-rays, and n is the order of diffraction.

A determination of the composition of the $\text{Si}_{1-x}\text{Ge}_x$ layers used in these studies was obtained from the 2θ value from the (400) reflection, in combination with a Vegard's Law analysis, where a linear relation between the composition and lattice constant are assumed. The growth of the $\text{Si}_{1-x}\text{Ge}_x$ layer using the Si wafer as an epitaxial substrate results in bi-axial compression in the growth plane, as Ge atoms fill spaces normally occupied by Si atoms, and the in-plane $\text{Si}_{1-x}\text{Ge}_x$ lattice constant is forced to match that of the substrate. This in turn produces a uniaxial strain in the growth direction, which results in an increase in the out-of-plane lattice constant, which is obtained via XRD.

The relation between in-plane and out-of-plane strains for cubic materials can be used to determine the strains in the $\text{Si}_{1-x}\text{Ge}_x$ alloy, and is given by the equation

$$\varepsilon_{\perp} = -2 \frac{c_{12}}{c_{11}} \varepsilon_{\parallel} \quad (2.2)$$

where ε_{\perp} and ε_{\parallel} are the out-of-plane and in-plane strains; c_{11} and c_{12} are the elastic constants. The in and out-of-plane strains of the $\text{Si}_{1-x}\text{Ge}_x$ alloy can also be defined in terms of the in-plane and out-of-plane lattice parameters by the following equations:

$$\varepsilon_{\parallel} = \frac{a_{\parallel} - a_0}{a_0} \quad (2.3)$$

$$\varepsilon_{\perp} = \frac{a_{\perp} - a_0}{a_0} \quad (2.4)$$

where a_{\parallel} and a_{\perp} are the in-plane and out-of-plane lattice constants, respectively, and a_0 is the lattice parameter of the unstrained $\text{Si}_{1-x}\text{Ge}_x$.

The elastic constants c_{11} and c_{12} can be determined from the Rule of Mixtures [7], which relates the elastic constants of the strained alloy in terms of the elastic constants of pure Si and Ge, and is given by the relation

$$c_{ij} = c_{ij}^{Ge} x_{Ge} + c_{ij}^{Si} (1 - x_{Ge}) \quad (2.5)$$

where c_{ij} is the elastic constant of the strained alloy, $c_{ij}^{Ge(Si)}$ is the elastic constant of either pure Si or pure Ge, and x_{Ge} is the concentration of Ge in the strained alloy.

Equations 2.2-2.5 can be combined, along with the relation for the lattice constant of the unstrained alloy

$$a_0 = a_{Ge} x_{Ge} + a_{Si} (1 - x_{Ge}) \quad (2.6)$$

to obtain a relation between the elastic constants and the lattice parameters, given by the equation [1]

$$1.55x_{Ge}^2 + (37.3a_{\perp} - 136)x_{Ge} + 165.8a_{\perp} - 90.05 = 0 \quad (2.7)$$

where a_{\perp} is given in units of nm.

The composition of the titanium germanosilicide thin films grown in these studies were also obtained from the XRD data. The composition was determined by using Vegard's Law, assuming that the out-of-plane lattice parameter of the $Ti(Si_{1-y}Ge_y)_2$ film has a linear relationship to the lattice parameters of both bulk $TiSi_2$ and $TiGe_2$. The relationship can be fully expressed by the equation

$$a_{Ti(Si_{1-y}Ge_y)_2} = a_{TiSi_2}(1-y) + a_{TiGe_2}y \quad (2.8)$$

where y is the Ge concentration of the germanosilicide, a_{TiSi_2} and a_{TiGe_2} are the lattice parameters of bulk $TiSi_2$ and $TiGe_2$, and $a_{Ti(Si_{1-y}Ge_y)_2}$ is the out-of-plane lattice parameter of the $Ti(Si_{1-y}Ge_y)_2$ film, and can be obtained from the 2θ values of the XRD scans.

The x-ray diffraction scans were taken on a Rigaku Geigerflex D/Max A series diffractometer, with $Cu K_{\alpha}$ radiation, operated at a 27kV tube voltage and 20mA tube current in a $\theta - 2\theta$ data collection mode, with 1° diffraction and scattering slits, and a detector energy resolution of 42-45%. A graphite monochromator was used to filter the x-rays after diffraction from the sample surface and before they reached the detector. Since the seed crystals used in these studies are Si (100), the Si (400) K_{α} peaks at 69.13° and 69.33° were used to align the samples to the diffractometer optics, which results in an uncertainty of $\pm 0.01^{\circ}$.

2.5 Auger Electron Spectroscopy

Auger electron spectroscopy (AES) was used to obtain surface chemistry information from the samples. In particular, it was used to determine the presence of Si, Ge, Ti, and Co, in addition to O or C contamination which might be present on a sample surface.

The technique relies on the production of Auger electrons from the material to be analyzed, and is dependent upon the transition probability for either x-ray fluorescence or for the Auger electron to be produced. The Auger transition occurs when the core level of a surface atom is probed by incoming electrons with a certain kinetic energy. If the core level is ionized, the atom can make a transition to a lower energy state by either emitting a x-ray photon, or by electrons from higher energy levels occupying the core hole left by the initial ejected electron.

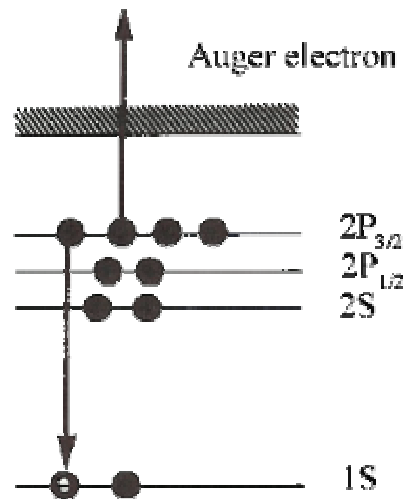


Figure 2.4: Schematic depicting the creation of a doubly ionized electronic state as an electron from the $2P_{3/2}$ energy level fills a core hole in the 1S energy level, and the emergence of an Auger electron, with kinetic energy equal to the difference in energies of the initial and doubly ionized states. Reproduced from Ref. [6].

If an electron in a higher energy level fills the void left by the initial ejected one, a series of electronic transitions can leave the atom in a doubly ionized state. The energy difference between the ionized and doubly ionized state is transferred to an Auger electron, which is ejected from the surface of the material and has an energy which is characteristic of the atom from which it was ejected. When Auger transitions occur near the surface, the electrons are ejected from the material without much of a loss of energy, and give rise to peaks in the secondary electron energy spectrum. The size and shape of these peaks are then used to identify the elements present on the surface.

An example of an AES spectrograph indicating the presence of Si and Ti, is shown in Figure 2.5. The change in electron count as a function of energy versus the change in energy for the KLL and LMN Auger transitions is used to indicate the presence of elements to within several monolayers of electron penetration depth, since the mean free path of the Auger electrons is on the order of 10 Å. Thus, AES provides relatively good information regarding the surface chemistry of the sample in question.

The samples used in these studies were calibrated for measurement by the adjustment of the sample surface distance from the gun and analyzer to 2 KeV incident electrons, with a filament current of 1mA and emission current of 0.5 mA. The scans were taken with 3 KeV incident electrons, also with the same filament and emission current used during calibration. The energy range of the scans was from 0 to 1200 eV.

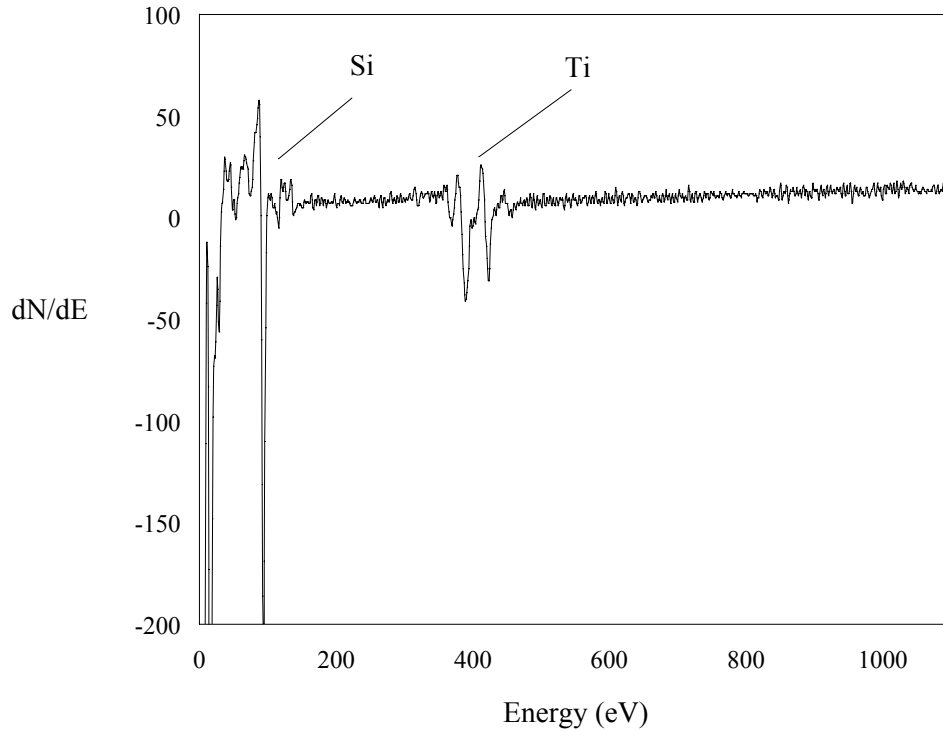


Figure 2.5: AES scan, which indicates the presence of Si and Ti. The locations of the peaks are associated with KLL and LMN electronic transitions for Si and Ti, respectively.

The electron gun and analyzer used in the AES characterizations were manufactured by VG Microtech and Physical Electronics Industries, respectively. The specifications for both components are given as follows:

Electron gun:	Model LEG63
Energy range	0.1-5 KeV
Filament	Thorium/Rhenium

Current	10nA-5 μ A
Spot size	~ 50 μ m
Analyzer:	Model 10-360 SCA

The analyzer is component of the Model 3057 photoelectron spectroscopy subsystem from Physical Electronics Industries which also consists of a Model 80-365H SCA control, a Model 137 PC interface, a Model 1182 amplifier/discriminator, A Model 72-366 OMNI Focus Small Area Lens Control, an OMNI Focus Small Area Lens Fixed Aperture, and a Model 3057-AD-01 SCA Single Channel Detector Option.

2.6 Scanning Electron Microscopy

Scanning Electron Microscopy (SEM) was used in these studies to observe the surface morphology of the films. In this technique, a focused electron beam of 100 Å spot size is raster scanned across the surface of the specimen to be observed. During this event, various signals are produced from the irradiated volume of interest, including signals from backscattered, secondary, and Auger electrons, as well as signals from x-rays and photons of other wavelengths.

The secondary and backscattered electron signals were collected while in topography mode, as they vary as a function of surface topography, and allow the acquisition of images with high resolution. The secondary electrons are emitted from the sample surface with a kinetic energy on the order of tens of angstroms, and with a mean free path of less than 50 Å.

The high resolution capabilities of this instrument allowed the determination of surface morphology and precipitate formation occurring in the titanium

germanosilicide on $\text{Si}_{1-x}\text{Ge}_x$ thin film samples, as well as a determination of the surface morphology and layer inversion which occurred in the titanium interlayer mediated epitaxy of CoSi_2 on $\text{Si}_{1-x}\text{Ge}_x$ samples.

A JOEL Model number JSM 6400F SEM was used, with a resolution of 15\AA @ 30kV , and 70\AA @ 1kV , accelerating voltage of $0.5\text{-}30\text{kV}$, magnification of $20\text{x-}450,000\text{x}$, and depth of focus of $5\text{-}39\text{ mm}$.

References

1. P.T. Goeller, Ph.D. thesis, North Carolina State University, 1999.
2. D.B. Aldrich, Ph.D. thesis, North Carolina State University, 1995.
3. M.J. Fay, A. Proctor, D.P. Hoffmann, and D.M. Hercules, *Anal. Chem.* **60**, 1225-1243 (1988).
4. M. Newville in *Fundamentals of XAFS* (Consortium for Advanced Radiation Sources, University of Chicago, 2002).
5. L.E. Davis, N.C. MacDonald, P.W. Palmberg, G.E. Riach, and R.E. Webber in *Handbook of Auger Electron Spectroscopy* (Physical Electronics Industries, 1976).
6. D.C. Koningsberger and R. Prins in *X-ray Absorption: Principles, Applications, Techniques of EXAFS, SEXAFS, AND XANES* (John Wiley and Sons, 1988).
7. S.P. Baker and E. Arzt, *Elastic Stiffness Constants of SiGe*, in *Properties of Strained and Relaxed Silicon Germanium*, E. Kasper, Editor. 1995, INSPEC: London. 67-69.
8. H.P. King and L.E. Alexander in *X-ray Diffraction Procedures: For Polycrystalline and Amorphous Materials, 2nd Edition*. 1974, Wiley-Interscience.
9. M. Newville, *J. Synchrotron Rad.* **8**, 322-324 (2001).
10. M. Newville, P. Līviņš, Y. Yacoby, J.J. Rehr, and E.A. Stern, *Phys. Rev. B* **47**, 14126-14131 (1993).

Chapter 3

Growth and Stability of Titanium Germanosilicide Thin Films on $\text{Si}_{1-x}\text{Ge}_x$

James E. Burnette, Robert J. Nemanich, and Dale E. Sayers

Submitted for Publication to Journal of Applied Physics

3. Growth and Stability of Titanium Germanosilicide Thin Films on $\text{Si}_{1-x}\text{Ge}_x$

James E. Burnette, Robert J. Nemanich, Dale E. Sayers

Department of Physics, North Carolina State University, Raleigh, NC 27695-8202

The sequential deposition and annealing to 700°C of $\text{Si}_{1-x}\text{Ge}_x$ pseudomorphically strained to Si (100) with concentrations $x = 0.20$ and 0.30 , amorphous silicon, and titanium on Si (100) leads to the formation of a C54 $\text{Ti}(\text{Si}_{1-y}\text{Ge}_y)_2/\text{Si}_{1-x}\text{Ge}_x$ bi-layer, whose phase formation and interface stability are studied. The use of an amorphous layer of Si is employed to eliminate or decrease the formation of germanium-rich $\text{Si}_{1-z}\text{Ge}_z$ alloy precipitates found in the solid phase reaction of Ti and $\text{Si}_{1-x}\text{Ge}_x$. It has been proposed that the precipitation phenomenon was driven by changes in the enthalpy of formation as a function of concentration in the $\text{Ti}(\text{Si}_{1-y}\text{Ge}_y)_2$ layer, resulting from the enthalpy difference between TiSi_2 and TiGe_2 compounds, both of which are assumed to be completely miscible with one another. In this study, a Gibbs free energy model parameterized in terms of atomic percentage of Ge was used to determine the concentration of the $\text{Ti}(\text{Si}_{1-y}\text{Ge}_y)_2$ compound in equilibrium with the $\text{Si}_{1-x}\text{Ge}_x$ substrate. Layers of amorphous silicon of varying thickness were incorporated between a 300 \AA Ti layer and the strained $\text{Si}_{1-x}\text{Ge}_x$ substrate layer to achieve $\text{Ti}(\text{Si}_{1-y}\text{Ge}_y)_2$ films that are in equilibrium with the $\text{Si}_{1-x}\text{Ge}_x$ substrate. The use of amorphous silicon layers of varying thickness indicated that $\text{Ti}(\text{Si}_{1-y}\text{Ge}_y)_2/\text{Si}_{1-x}\text{Ge}_x$ films could be formed with the absence of germanium rich precipitates at the grain boundaries, depending on the amorphous silicon layer thickness.

3.1 Introduction

Epitaxial $\text{Si}_{1-x}\text{Ge}_x$ alloys on Si (100) are of interest from a technological standpoint because of their potential in IC device applications. Electronic devices have been fabricated and demonstrated based on $\text{Si}_{1-x}\text{Ge}_x/\text{Si}$ heterojunctions, and $\text{Si}_{1-x}\text{Ge}_x$ in the context of integrated circuit technology has been used for channel engineering and raised source-drain contacts [1-4]. In silicon integrated circuit technology, source-drain contacts typically employ silicide films formed by solid-state reaction. A similar approach would be important for Si-Ge device structures. Information concerning reactions between metal germanosilicides and $\text{Si}_{1-x}\text{Ge}_x$ alloys is necessary in order to successfully fabricate these structures.

There has been a significant effort to study the phase formation of some metal/ $\text{Si}_{1-x}\text{Ge}_x$ reactions and the properties of their products [5-9]. When Ti reacts with Si or Ge, the final phases that form are C54 TiSi_2 or C54 TiGe_2 (face-centered orthorhombic), which form around 600-700°C. Intermediate phases of C49 TiSi_2 (body-centered orthorhombic) or Ti_6Ge_5 compounds form between 400°C and 600°C. The C54 phase of TiSi_2 is used to form interconnects and source-drain contacts, due to its lower resistivity as compared to the C49 phase of TiSi_2 , the C54 phase of TiGe_2 , or the Ti_6Ge_5 compound.

Recently, the phase formation and interface stability of Ti on $\text{Si}_{1-x}\text{Ge}_x$ has been studied [10]. In this work, Ti was directly deposited onto a strained $\text{Si}_{1-x}\text{Ge}_x$ substrate grown epitaxially to Si (100). Upon annealing, it was found that a $\text{Ti}(\text{Si}_{1-y}\text{Ge}_y)_2$ layer initially formed on the $\text{Si}_{1-x}\text{Ge}_x$ substrate, and the $\text{Ti}(\text{Si}_{1-y}\text{Ge}_y)_2$ compound contained the same ratio of silicon to germanium atoms as the substrate ($y = x$). Upon further

annealing, it was noted that the composition of the $\text{Ti}(\text{Si}_{1-y}\text{Ge}_y)_2$ layer changed ($y < x$), and that Ge-rich ($z > x$) $\text{Si}_{1-z}\text{Ge}_z$ precipitates formed along the grain boundaries of the C54 $\text{Ti}(\text{Si}_{1-y}\text{Ge}_y)_2$ film.

Since TiSi_2 and TiGe_2 , and Si and Ge are completely miscible and form continuous solid solutions, and the enthalpy of formation of TiSi_2 is larger than that of TiGe_2 , there is a tendency for Si to replace Ge in the $\text{Ti}(\text{Si}_{1-y}\text{Ge}_y)_2$ compound. This replacement is accompanied by the formation of germanium-rich Si-Ge precipitates at the $\text{Ti}(\text{Si}_{1-y}\text{Ge}_y)_2$ grain boundaries. During this process, Si and Ge atoms are extracted from the $\text{Si}_{1-x}\text{Ge}_x$ substrate and diffuse through the $\text{Ti}(\text{Si}_{1-y}\text{Ge}_y)_2$ compound, and as Ge is replaced by Si in the $\text{Ti}(\text{Si}_{1-y}\text{Ge}_y)_2$ compound, excess Si and Ge atoms diffuse to the grain boundaries. The formation of the precipitate clusters occurs as the bi-layer system minimizes the Gibbs free energy at both the $\text{Ti}(\text{Si}_{1-y}\text{Ge}_y)_2/\text{Si}_{1-x}\text{Ge}_x$ interface and between $\text{Ti}(\text{Si}_{1-y}\text{Ge}_y)_2$ grains.

This behavior is not desirable in the context of IC technology since this segregation will lead to $\text{Ti}(\text{Si}_{1-y}\text{Ge}_y)_2$ layer degradation and an interruption of the low-resistance conductance path through the film. This paper addresses this problem by investigating an approach to form stable bi-layer structures without the formation of the Ge-rich $\text{Si}_{1-z}\text{Ge}_z$ precipitates found when Ti is directly deposited onto a strained $\text{Si}_{1-x}\text{Ge}_x$ substrate. To this end, layers of amorphous silicon of varying thickness are formed between the strained $\text{Si}_{1-x}\text{Ge}_x$ and Ti layers to determine whether this approach can prevent precipitate formation and produce a more stable $\text{Ti}(\text{Si}_{1-y}\text{Ge}_y)_2/\text{Si}_{1-x}\text{Ge}_x$ alloy film.

In this study we employ a Gibbs free energy model, to determine the conditions that generate precipitate formation. The incorporation of an amorphous silicon layer serves to decrease the enthalpy of formation of the $\text{Ti}(\text{Si}_{1-y}\text{Ge}_y)_2$ layer, thereby effectively controlling the occurrence of the precipitation phenomenon. All experiments employed a 300 Å Ti layer and an amorphous Si layer thicknesses between 0 and 600 Å, since 681 Å of silicon would be consumed by 300 Å of Ti to form TiSi_2 . The 300 Å Ti thickness is typical in contact formation applications. Our experiments and calculations explore the temperature stability at 700° C, which is high enough to cause the solid-state reaction to form the C54 phase, and only causes partial relaxation of the $\text{Si}_{1-x}\text{Ge}_x$ layer.

3.2 Experiment

The $\text{Ti}(\text{Si}_{1-y}\text{Ge}_y)_2/\text{Si}_{1-x}\text{Ge}_x$ alloy films were formed by first growing strained $\text{Si}_{1-x}\text{Ge}_x$ layers with $x = 0.2$ and 0.3 approximately 1000 Å thick onto Si (100) p-type wafers using e-beam molecular beam epitaxy. The wafers were prepared for deposition by spin-etching with a $\text{HF}:\text{H}_2\text{O}:\text{ethanol}$ solution and then loaded into UHV for a thermal desorption at 900°C for 10 minutes to remove surface oxides and contaminants. To enhance pseudomorphic growth of the strained $\text{Si}_{1-x}\text{Ge}_x$ layer, silicon buffer layers ~ 200 Å thick were grown at 550°C in a solid-source MBE chamber with a base pressure of $<2.4 \times 10^{-10}$ Torr.

The strained $\text{Si}_{1-x}\text{Ge}_x$ layers were also grown at a temperature of 550°C. Silicon and germanium for the $\text{Si}_{0.80}\text{Ge}_{0.20}$ substrates were deposited at a rate of 4 Å/s and 1 Å/s, respectfully, and at rates of 3.5 Å/s and 1.5 Å/s for the $\text{Si}_{0.70}\text{Ge}_{0.30}$ substrates. A thickness of 1000 Å was chosen for these layers and the amount of

strain relaxation present before and after sample annealing was determined by Raman spectroscopy from the wavenumber of the optic phonon of the $\text{Si}_{1-x}\text{Ge}_x$ layers. The Raman spectra were obtained in a backscattering geometry using 514.5 nm radiation. Measurements were made on the $\text{Si}_{1-x}\text{Ge}_x$ layers after growth and after annealing at 700°C. The $\text{Si}_{0.70}\text{Ge}_{0.30}$ substrates show a 54% relaxation before annealing and a 72% relaxation after annealing, and the $\text{Si}_{0.8}\text{Ge}_{0.2}$ substrates show a 36% relaxation before annealing and a 42% relaxation after annealing [16,17].

After deposition of the strained $\text{Si}_{1-x}\text{Ge}_x$, the samples were allowed to cool and amorphous Si layers of 100, 400, 500, and 600 Å were deposited in the same MBE chamber with the substrate at room temperature. The samples were then transferred in UHV to an e-beam metallization chamber, where 300 Å of Ti was deposited at room temperature. As-deposited samples, where 300 Å of titanium was deposited directly onto strained $\text{Si}_{1-x}\text{Ge}_x$ layers were also fabricated for both $x = 0.20$ and 0.30. All samples were annealed in UHV at 700°C for 20 minutes. The position of the layered structure and the phase formation sequence is shown in Figure 3.1

The films were studied *ex situ* by x-ray diffraction (XRD) using a Rigaku Geigerflex diffractometer with $\text{Cu K}\alpha$ radiation, at a 27kV tube voltage and 20mA tube current, and data was collected in a θ - 2θ mode with 1° diffraction and scattering slits, with a detector resolution of 42-45%. The surface morphology of the films was studied using a Joel Scientific model 6400 field emission scanning electron microscope.

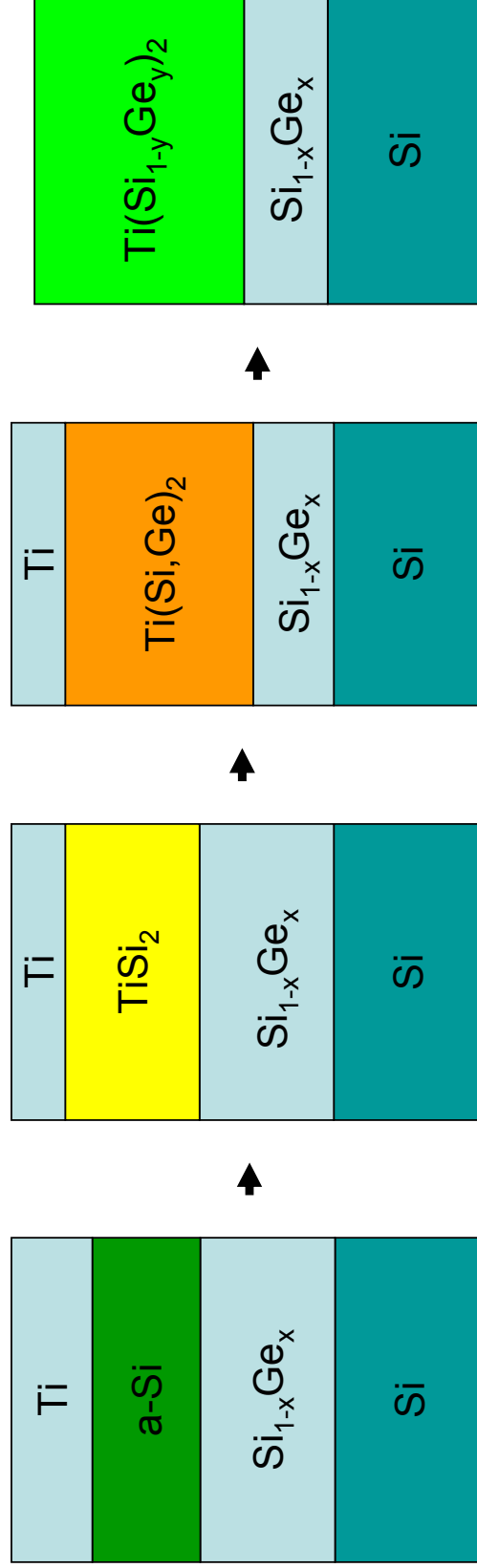


Figure 3.1: Layered structure after deposition and subsequent phase formation, leading to the formation of a $\text{Ti}(\text{Si}_{1-y}\text{Ge}_y)_2$ phase in equilibrium with the substrate.

3.3 Results

The XRD scans contain intensity peaks indicating diffraction from the C54 $\text{Ti}(\text{Si}_{1-y}\text{Ge}_y)_2$ (004), (311), and (313) diffraction planes, as shown in Figures 3.2 and 3.3. The concentration of germanium contained within the $\text{Ti}(\text{Si}_{1-y}\text{Ge}_y)_2$ compound can be determined by using the 2θ value for an intensity peak associated with a given orientation. From the determined plane spacing the lattice parameters are calculated, and compared with lattice parameters calculated from Vegard's Law using the C54 TiSi_2 and TiGe_2 lattice parameters as the endpoints.

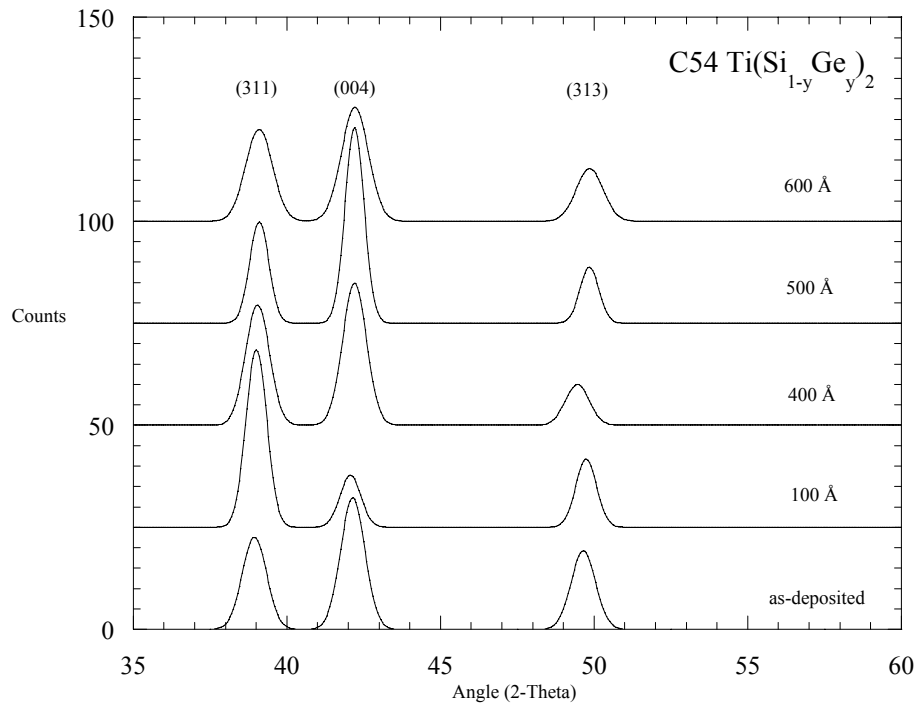


Figure 3.2: θ - 2θ XRD scan of C54 $\text{Ti}(\text{Si}_{1-y}\text{Ge}_y)_2$ compound on a strained $\text{Si}_{1.8}\text{Ge}_{0.2}$ substrate. The intensity peaks from (313), (004), and (311) diffraction planes are shown.

As shown in Figure 3.2, all three orientations occur in all samples with a $\text{Si}_{0.80}\text{Ge}_{0.20}$ substrate. The variation in peak intensities suggests a complex texturing process beyond the scope of this study.

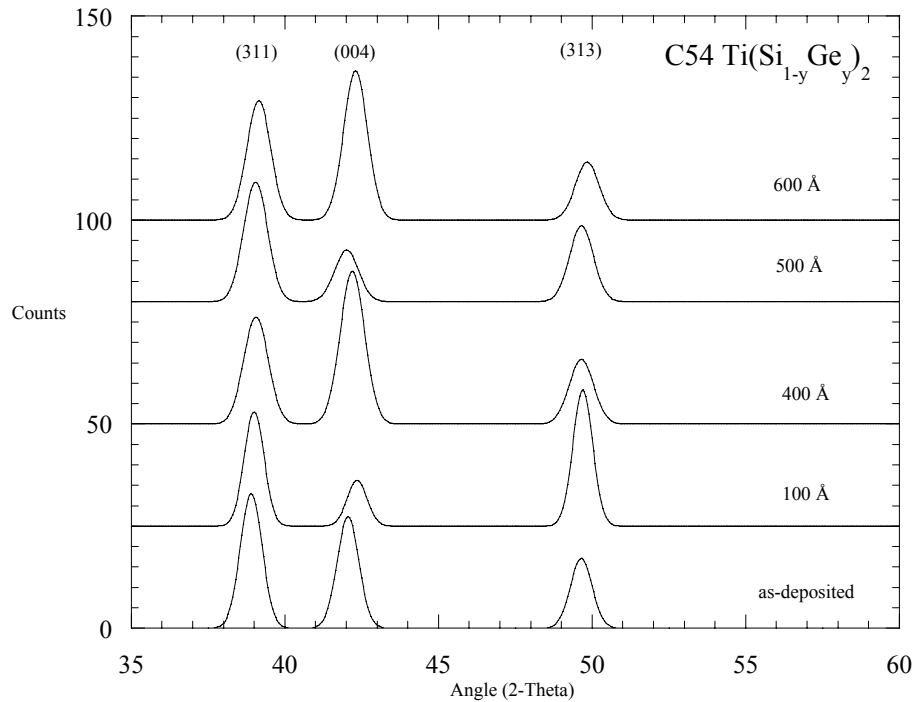


Figure 3.3: θ - 2θ XRD scan of $\text{C54 Ti(Si}_{1-y}\text{Ge}_y)_2$ compound on a strained $\text{Si}_{7}\text{Ge}_{3}$ substrate. The intensity peaks from (313), (004), and (311) diffraction planes are shown.

Using the position of the (004) diffraction peak, the concentration of the as-deposited sample was found to be $y = .077 \pm .019$. Similarly, the Ge concentration of the 100, 400, 500, and 600Å amorphous Si layered samples

were $y = .115 \pm .044$, $y = .034 \pm .012$, $y = .034 \pm .012$, and $y = .028 \pm .018$ respectfully. Using the position of the (311) diffraction peak, the concentration of the as-deposited sample was found to be $y = .106 \pm .024$. Similarly, the Ge concentration of the 100, 400, 500, and 600Å amorphous Si layered samples were $y = .069 \pm .012$, $y = .046 \pm .012$, $y = .016 \pm .018$, and $y = .016 \pm .017$ respectfully. The composition determination from the (004) and (311) diffraction peaks are all within the range of error for each respective layer thickness.

The SEM images clearly show the presence of precipitates at the grain boundaries in the as-deposited sample (Figure 3.4(a)), but as the amorphous layer thickness is increased, to 100 and 400 Å (Figures 3.4(b), 3.4(c)) the precipitate density decreases. As the amorphous layer thickness is further increased to 500 and 600Å, the precipitation phenomena is virtually non-existent, as shown in Figures 3.4(d) and 3.4(e).

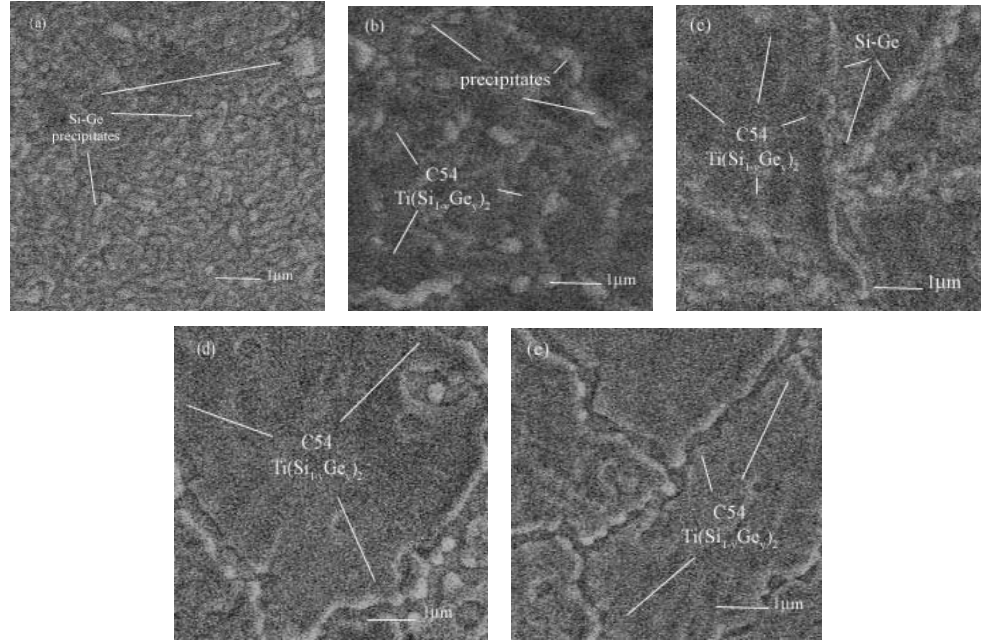


Figure 3.4: SEM micrographs of (a) as deposited, (b) 100 Å, (c) 400 Å, (d) 500 Å, and (e) 600 Å amorphous Si layered samples on a Si_8Ge_2 substrate annealed to 700°C. C54 $\text{Ti}(\text{Si}_{1-y}\text{Ge}_y)_2$ grains and $\text{Si}_{1-z}\text{Ge}_z$ precipitates shown.

For $\text{Si}_{0.70}\text{Ge}_{0.30}$ substrates, we again observe diffraction occurring from the (004), (311), and (313) planes and again a complex variation in intensities is observed, as shown in Figure 3.3.

Using the position of the (004) diffraction peak, the concentration of the as-deposited sample was found to be $y = .127 \pm .010$. Similarly, the Ge concentration of the 100, 400, 500, and 600Å amorphous Si layered samples were $y = .051 \pm .031$, $y = .040 \pm .012$, $y = .053 \pm .030$, and $y = .021 \pm .021$ respectfully. Using the position of the (311) diffraction peak, the concentration of the as-deposited sample was found to be $y = .129 \pm .016$. Similarly, the Ge concentration of the 100, 400, 500, and 600Å amorphous Si layered samples were $y = .075 \pm .012$, $y = .040 \pm .018$, $y = .082 \pm .020$,

and $y = .014 \pm .018$ respectfully. Again, the composition determination from the (004) and (311) diffraction peaks are all within the range of error for each respective layer thickness.

As shown in Figure 3.5, SEM micrographs indicate that precipitate formation is found in the as-deposited, 100, and 400 Å samples (Figures 3.5(a,b,c)), with decreasing precipitate density as the amorphous layer thickness is increased, but as the equilibrium phase boundary region is approached precipitate formation is eliminated (Figures 3.5(d,e)).

3.4 Discussion

3.4.1 Equilibrium Concentrations

The thermodynamic stability in the $\text{Ti}(\text{Si}_{1-y}\text{Ge}_y)_2/\text{Si}_{1-x}\text{Ge}_x$ system can be analyzed qualitatively by formulating its description in terms of the equilibration of the two phase field connecting a C54 $\text{Ti}(\text{Si}_{1-y}\text{Ge}_y)_2$ phase at a specific concentration with that of a coexisting $\text{Si}_{1-x}\text{Ge}_x$ phase at a particular concentration, where y need not be equal to x .

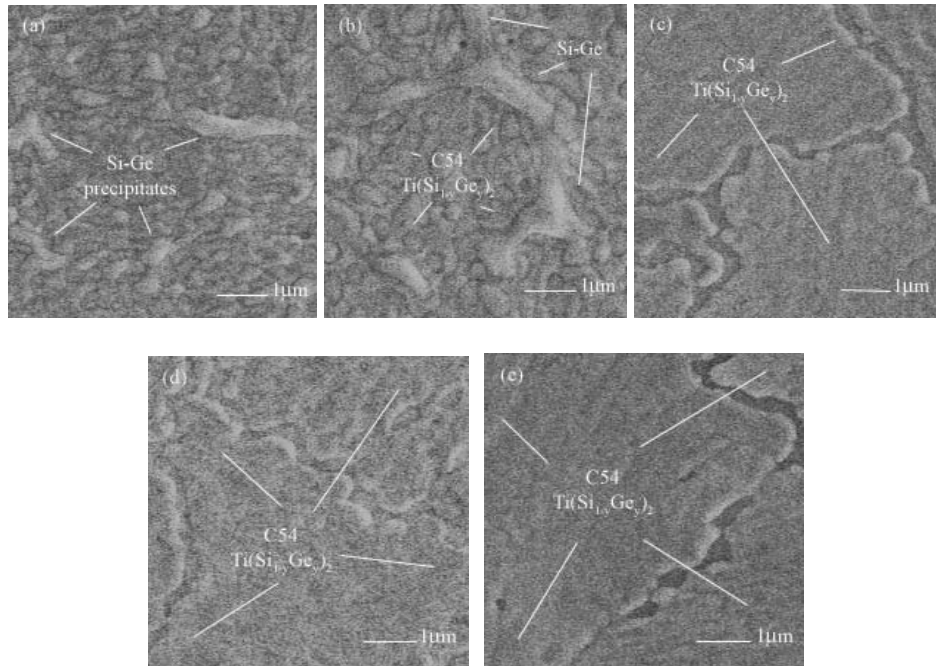


Figure 3.5: SEM micrographs of (a) as deposited, (b) 100 Å, (c) 400 Å, (d) 500 Å, and (e) 600 Å amorphous Si layered samples on a Si_7Ge_3 substrate annealed to 700°C. C54 $\text{Ti}(\text{Si}_{1-y}\text{Ge}_y)_2$ grains and $\text{Si}_{1-z}\text{Ge}_z$ precipitates shown.

Under isobaric and isochoric conditions, it is assumed that equilibrium states occur at minima for the total Gibbs free energy at the thin film interface between the two phases.

Aldrich, *et. al.* [10] developed a first approximation thermodynamic model to determine the Ge concentration present in both the $\text{Ti}(\text{Si}_{1-y}\text{Ge}_y)_2$ equilibrium compound and $\text{Si}_{1-x}\text{Ge}_x$ solid solution formed by direct deposition of Ti onto a strained $\text{Si}_{1-x}\text{Ge}_x$ substrate. The results were presented in a ternary phase diagram for the reaction, in order to determine the conditions that marked the onset of precipitate formation.

In order to simplify matters, we assume that one mole of the $\text{Ti}(\text{Si}_{1-y}\text{Ge}_y)_2$ equilibrium compound is in contact with one mole of the $\text{Si}_{1-x}\text{Ge}_x$ solid solution, under the assumptions that the Si and Ge in both the equilibrium compound and solid solution behave as an “ideal” solution, where the entropy in the system is only due to the mixing of Si and Ge atoms. We also assume that pure Si and pure Ge are at a zero free energy reference state, and that pure TiSi_2 also has a free energy reference state of zero. Then the free energy reference state of TiGe_2 is the difference in the enthalpy of formation of TiSi_2 (-57 kJ/mol) and TiGe_2 (-49 kJ/mol), with a value of 8 kJ/mol [10].

An expression for the change in the Gibbs free energy of the $\text{Ti}(\text{Si}_{1-y}\text{Ge}_y)_2$ equilibrium compound is found to be:

$$\Delta G_1 = m(y) + 2/3RT[y \ln y + (1 - y) \ln(1 - y)] \quad (1)$$

where in the first term m is the difference in enthalpy of formation between C54 TiSi_2 and C54 TiGe_2 , the second term describes the entropy of mixing, where the factor of $2/3$ is due to the fact that only Si and Ge atoms mix in the equilibrium compound, and y is the initial C54 $\text{Ti}(\text{Si}_{1-y}\text{Ge}_y)_2$ Ge concentration, which is a function of the a-Si layer thickness and the substrate concentration x .

The expression for the change in free energy of the $\text{Si}_{1-x}\text{Ge}_x$ solid solution is:

$$\Delta G_2 = RT[x \ln x + (1 - x) \ln(1 - x)] \quad (2)$$

where the only contribution to the Gibbs free energy is the entropy of mixing, and x is the Ge concentration of the $\text{Si}_{1-x}\text{Ge}_x$ solid solution. Because of the difference in the heat of formation between TiSi_2 and TiGe_2 , the Ge concentration in the equilibrium compound decreases from the initial value during the course of the reaction.

Conservation of matter then dictates an increase in the concentration of the solid solution from its initial value. The free energy terms ΔG_1 and ΔG_2 would be summed, and the final Ge compositions of both the equilibrium compound and solid solution are determined from minimizing this expression [10].

A graph depicting the coexisting equilibrium phases of the C54 $\text{Ti}(\text{Si}_{1-y}\text{Ge}_y)_2$ compound with the $\text{Si}_{1-x}\text{Ge}_x$ substrate at 600, 700, and 800°C is shown in Figure 3.6. The dashed line indicates the high-temperature limit, where the total configurational entropy of the system drives the change in free energy, in which case the germanium concentrations of both the $\text{Ti}(\text{Si}_{1-y}\text{Ge}_y)_2$ compound and $\text{Si}_{1-x}\text{Ge}_x$ substrate are equal ($y = x$).

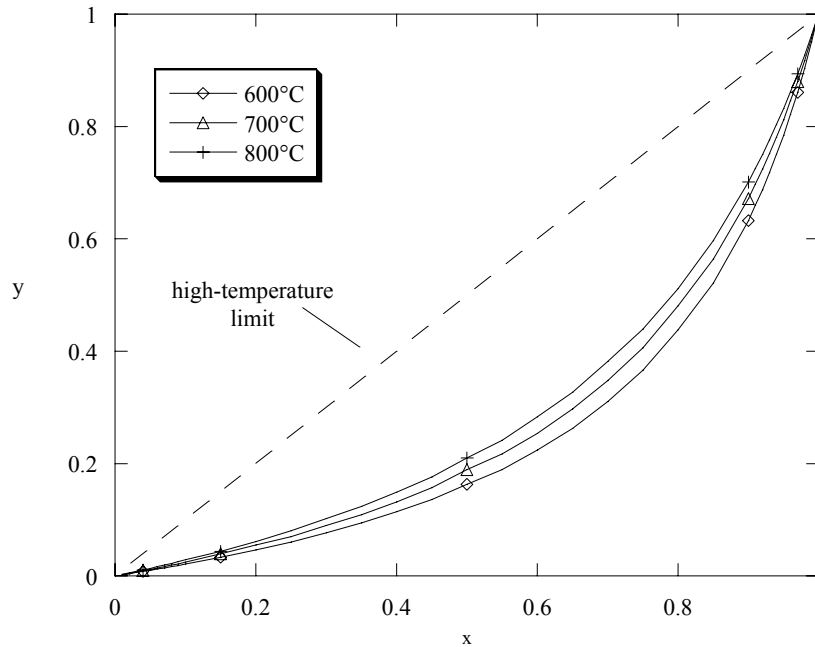


Figure 3.6: Plot of the germanium concentrations of C54 $\text{Ti}(\text{Si}_{1-y}\text{Ge}_y)_2$ layer in equilibrium with the $\text{Si}_{1-x}\text{Ge}_x$ substrate at 600°C, 700°C, and 800°C. Equilibrium in the high-temperature limit indicated by the dashed line.

If the atomic mobilities of Si and Ge in both the $\text{Ti}(\text{Si}_{1-y}\text{Ge}_y)_2$ compound and $\text{Si}_{1-x}\text{Ge}_x$ substrate were similar, the system would be directly driven to equilibrium, with the absence of precipitation, implying thermodynamic stability. However, the mobilities of Si and Ge in the $\text{Ti}(\text{Si}_{1-y}\text{Ge}_y)_2$ compound and substrate are different; the diffusion of Si and Ge atoms is rapid in the $\text{Ti}(\text{Si}_{1-y}\text{Ge}_y)_2$ compound and negligible in the substrate. This, coupled with the enthalpy change in the of $\text{Ti}(\text{Si}_{1-y}\text{Ge}_y)_2$ compound eventually leads to the formation of precipitates at the grain boundaries of the subsequent film that forms.

These calculations show that for a solid solution substrate with Ge concentration $x = 0.20$ at 700°C , the Ge concentration for the equilibrium $\text{Ti}(\text{Si}_{1-y}\text{Ge}_y)_2$ compound film is $y = 0.05$. The tie line connecting this equilibrium two phase field defines a saturation limit with respect to the maximum percentage of germanium which the $\text{Ti}(\text{Si}_{1-y}\text{Ge}_y)_2$ layer can incorporate without precipitate formation. The chemical potentials with respect to Ge of both the $\text{Ti}(\text{Si}_{1-y}\text{Ge}_y)_2$ layer and the $\text{Si}_{1-x}\text{Ge}_x$ layer are equivalent at this point, implying that the bi-layer system is at equilibrium, defining a boundary between phases where precipitation will and will not occur.

3.4.2 Reaction Dynamics

We now consider two situations where $\text{Ti}(\text{Si}_{1-y}\text{Ge}_y)_2$ films are formed through solid state reactions, which are then in contact with the $\text{Si}_{1-x}\text{Ge}_x$ strained substrate layer. In one case the $\text{Ti}(\text{Si}_{1-y}\text{Ge}_y)_2$ film has a concentration that is more Ge-rich than the equilibrium concentration, and in the other case the film is more Si-rich than the equilibrium concentration.

For $\text{Ti}(\text{Si}_{1-y}\text{Ge}_y)_2$ layers with Ge concentrations, y , to the right of the boundary, the Gibbs free energy in the $\text{Ti}(\text{Si}_{1-y}\text{Ge}_y)_2$ layer would be reduced by the formation of the Ge-rich Si-Ge precipitates. Our observations are consistent with this prediction. We note that the formation of Ge rich precipitates can occur from any surface of the $\text{Ti}(\text{Si}_{1-y}\text{Ge}_y)_2$ layer, since this precipitation will drive that region of the film towards the concentration determined from the Gibbs free energy minimum. Diffusion will occur in the $\text{Ti}(\text{Si}_{1-y}\text{Ge}_y)_2$ layer which would equilibrate the concentration of the film and lower the overall Ge concentration. This process was described previously [10].

For $\text{Ti}(\text{Si}_{1-y}\text{Ge}_y)_2$ layers with Ge concentrations, y , to the left of the equilibrium tie line, the $\text{Ti}(\text{Si}_{1-y}\text{Ge}_y)_2$ layer is Si-rich. According to the model, the reduction of the Gibbs free energy in this case should result in the precipitation of a Si-Ge compound with a Ge concentration less than x of the $\text{Si}_{1-x}\text{Ge}_x$ substrate. To maintain equilibrium at the precipitate interface, the precipitate concentration, as determined from the equilibrium calculations, would have a Ge concentration greater than y of the $\text{Ti}(\text{Si}_{1-y}\text{Ge}_y)_2$ layer. Again, any surface of the film could be available for precipitate formation; however, the situation is different from the Ge-rich case. In this case, the precipitation would lead to a Si enrichment of the adjoining $\text{Ti}(\text{Si}_{1-y}\text{Ge}_y)_2$ layer. The formation of a Si enriched $\text{Ti}(\text{Si}_{1-y}\text{Ge}_y)_2$ region leads to a relative increase in the Gibbs free energy. In other words, even though enough Si is available from the $\text{Ti}(\text{Si}_{1-y}\text{Ge}_y)_2$ layer to form the precipitate, Ge is not available in the amount required to create a Si-Ge precipitate which would be in equilibrium with the $\text{Ti}(\text{Si}_{1-y}\text{Ge}_y)_2$ layer. As a result, a significant amount of material transport would have to

occur between both interfaces in order to minimize the free energy in this manner. Thus, the diffusion of material through the $\text{Ti}(\text{Si}_{1-y}\text{Ge}_y)_2$ layer leads to a tendency for the system to remain in its initial state.

For both cases discussed above, there may be other factors such as surface energies and strain that would modify the Gibbs equilibrium and also diffusion kinetics and nucleation barriers that would limit the precipitation process.

3.4.3 Experimental Analysis

From our experimental conditions, with an amorphous Si interlayer, the initial values for the concentrations are determined from the equation:

$$y' = \left[\left(I - \frac{t_{Si}}{2.27 t_{Ti}} \right) x \right] \quad (3)$$

where y' is the initial Ge concentration in the $\text{Ti}(\text{Si}_{1-y}\text{Ge}_y)_2$ layer formed by solid state reaction, t_{Si} and t_{Ti} are the a-Si layer and titanium layer thickness, and $0 \leq t_{Si} \leq 2.27 t_{Ti}$. Here 2.27 is a stoichiometric factor arising from the differences in the molar densities and atomic masses between pure Ti and Si, calculated by taking a volume containing n moles of Ti with a certain thickness, equal to t_{Ti} , of which 2n moles of Si will be need to form a TiSi_2 compound, from which an upper limit to t_{Si} can be determined. The term x is the initial Ge concentration in the $\text{Si}_{1-x}\text{Ge}_x$ solid solution. The changes in ΔG_1 due to the presence of the a-Si layer are then

incorporated into y , since it is assumed that during the initial stages of the reaction, the titanium, a-Si, and the $\text{Si}_{1-x}\text{Ge}_x$ react to form a $\text{Ti}(\text{Si}_{1-y'}\text{Ge}_{y'})_2$ layer. From there, the system is driven to its equilibrium state.

Based on our analysis, those $\text{Ti}(\text{Si}_{1-y}\text{Ge}_y)_2$ films with $y' \leq 0.05$ in contact with a $\text{Si}_{0.8}\text{Ge}_{0.2}$ substrate, which are to the left of the boundary, will not be driven by the free energy difference. As a consequence, precipitate formation in grain boundaries is not likely. In this case, the energetics of the system are such that there is a barrier to precipitate formation, and y' does not change appreciably during the course of the reaction. For those $\text{Ti}(\text{Si}_{1-y}\text{Ge}_y)_2$ films with a concentration $y' \geq 0.05$, equilibration to the $\text{Si}_{0.80}\text{Ge}_{0.20}$ substrate is achieved by replacing Ge atoms with Si atoms in the $\text{Ti}(\text{Si}_{1-y}\text{Ge}_y)_2$ lattice, which can be accomplished by extracting Si and Ge atoms from the substrate. Precipitate formation then occurs to minimize interfacial and surface energies due to the presence of extra Ge. In this case, the minimization of the Gibbs free energy in the $\text{Ti}(\text{Si}_{1-y}\text{Ge}_y)_2$ layer drives the subsequent phase formation and the precipitation process. Within the context of the experiment, the a-Si layered samples resulting in concentrations $y' \leq 0.05$ should not exhibit precipitate formation, while those with concentrations greater than $y' \geq 0.05$ should exhibit precipitate formation.

Based on the thicknesses employed, the 100, 400, 500, and 600 Å samples would have initial concentrations of 0.080, 0.060, 0.053, and 0.047, respectfully. Thus, the tie line which shows the $\text{Ti}(\text{Si}_{1-y}\text{Ge}_y)_2$ compound in equilibrium with the $\text{Si}_{0.80}\text{Ge}_{0.20}$ solid solution is bounded on the left by the concentration of the 600 Å sample, and bounded on the right by the concentrations of the 100, 400, and 500 Å samples, which implies that the 600 Å amorphous layered sample should be

precipitate-free, while the 500 , 400 and 100 Å samples should show evidence of precipitate formation in the grain boundaries of the film. Figure 3.7 displays a ternary phase diagram, which depicts the compositional

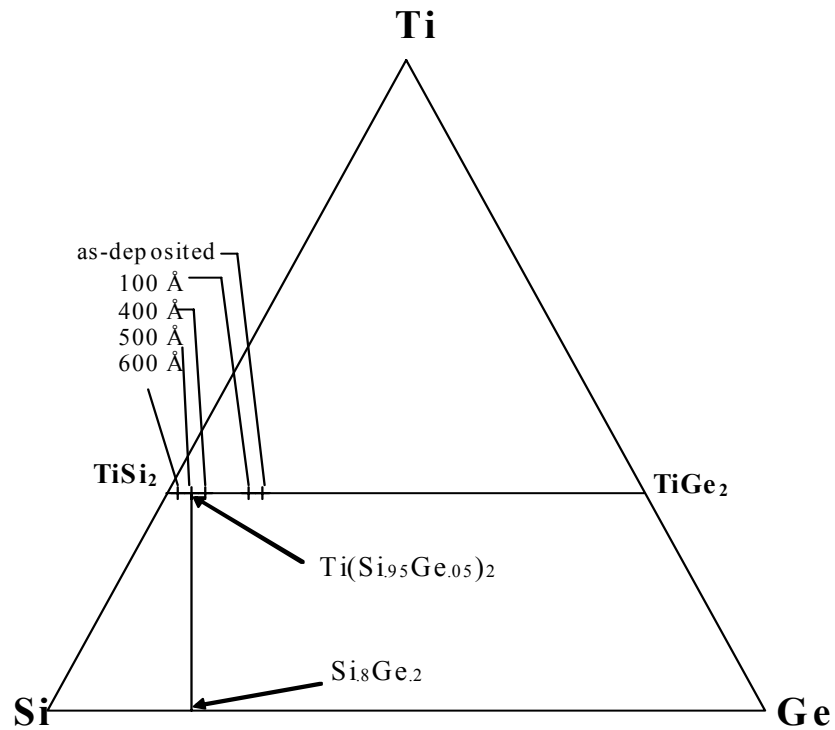


Figure 3.7: Ternary phase diagram of $\text{Ti}(\text{Si}_{1-y}\text{Ge}_y)_2/\text{Si}_{1-x}\text{Ge}_x$ reaction, indicating titanium germanosilicide compound in equilibrium with Si_8Ge_2 substrate. Arrows indicate initial concentrations of the 100 Å, 400 Å, 500 Å, 600 Å amorphous layered samples and Ti directly deposited onto Si_8Ge_2 substrate. As seen from the diagram, the 600 Å sample should be precipitate free, while the 100 Å, 400 Å, 500, and directly deposited samples should show evidence of precipitate formation at the $\text{Ti}(\text{Si}_{1-y}\text{Ge}_y)_2$ grain boundaries.

relationship of the as-deposited and amorphous layered samples to the two-phase equilibrium boundary for a solid solution with concentration of $x = 0.20$.

For $\text{Si}_{0.70}\text{Ge}_{0.30}$ substrates at 700°C , the equilibrium tie line connects the $\text{Ti}(\text{Si}_{0.91}\text{Ge}_{0.09})_2$ phase with the substrate. Based on the a-Si layer thickness employed, the 100, 400, 500, and 600 Å samples would have initial concentrations of 0.255, 0.123, 0.079, and 0.035, respectively. The 600 and 500 Å amorphous layered samples lie to the left of the $y = 0.090$ boundary, while the 400 and 100 Å amorphous layered samples lie to the right of the boundary, as shown in Figure 3.8.

A comparison between the values of y' and the concentrations of the as-deposited and amorphous layered samples determined from XRD for both $\text{Si}_{0.80}\text{Ge}_{0.20}$ and $\text{Si}_{0.70}\text{Ge}_{0.30}$ substrates is shown in Figures 3.9 and 3.10. We note that for the 600 and 500 Å amorphous layers, concentration information from XRD is comparable to the values for y' , within the region of uncertainty. As the amorphous layer thickness is decreased, to 400 and 100 Å, and finally to 0 Å (as-deposited), the germanium concentration as calculated from XRD measurements decreases, and is less than the value given for y' . In each case the values approach the equilibrium concentrations predicted by the model.

We can then use the model to determine the minimum a-Si layer thickness which will equilibrate a $\text{Ti}(\text{Si}_{1-y}\text{Ge}_y)_2/\text{Si}_{1-x}\text{Ge}_x$ bi-layer without precipitate formation, for a given Ti layer thickness. These layer thicknesses could be used to define a window for fabrication processes. Focusing attention to equilibrating with $\text{Si}_{0.70}\text{Ge}_{0.30}$ substrates at 700°C , we have shown that given a Ti layer thickness of 300 Å, a direct equilibration tie line connects a $\text{Ti}(\text{Si}_{0.91}\text{Ge}_{0.09})_2$ phase with the $\text{Si}_{0.70}\text{Ge}_{0.30}$ substrate.

Again using the relation between the initial composition in the equilibrium compound and the amorphous

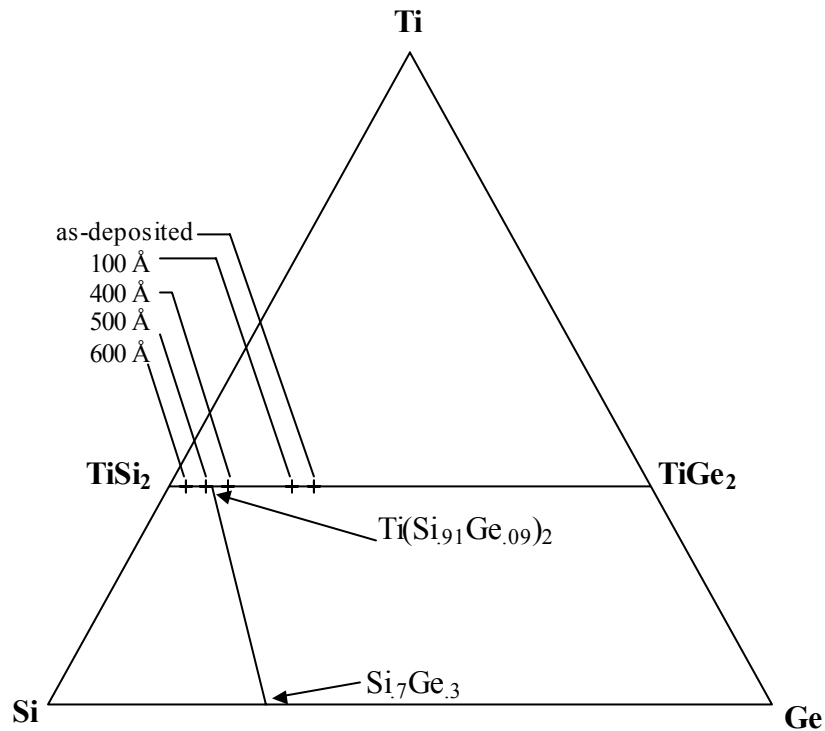


Figure 3.8: Ternary phase diagram of 1 mol-1 mol $\text{Ti}(\text{Si}_{1-y}\text{Ge}_y)_2/\text{Si}_{1-x}\text{Ge}_x$ reaction, indicating titanium germanosilicide compound in equilibrium with Si_7Ge_3 substrate. Arrows indicate initial concentrations of the 100 Å, 400 Å, 500 Å, 600 Å amorphous layered samples and Ti directly deposited onto Si_7Ge_3 substrate. As seen from the diagram, the 500 Å and 600 Å samples should be precipitate free, while the 100 Å, 400 Å, and directly-deposited samples should show evidence of precipitate formation at the $\text{Ti}(\text{Si}_{1-y}\text{Ge}_y)_2$ grain boundaries.

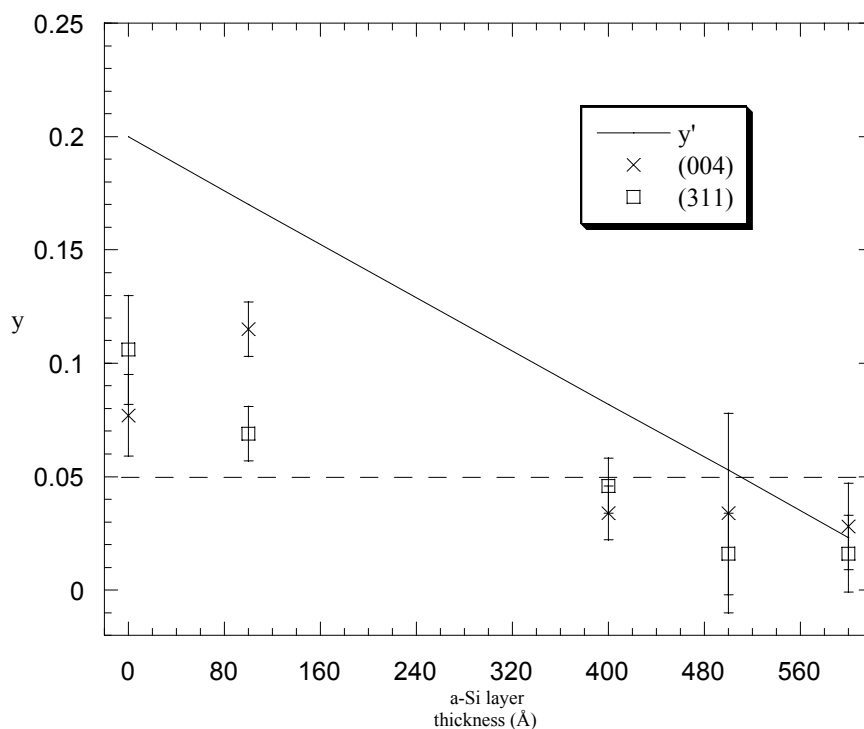


Figure 3.9: Comparison of y' (initial Ge concentration) and y (final Ge concentration) of as-deposited and amorphous layered samples for $\text{Si}_{1.8}\text{Ge}_{0.2}$ substrates calculated from XRD for (004) and (311) orientations. The solid line indicates y' versus the a-Si layer thickness. Symbols represent the Ge concentration versus a-Si layer thickness, as determined from the (004) and (311) diffraction peaks. The equilibrium Ge concentration of the $\text{Ti}(\text{Si}_{1-y}\text{Ge}_y)_2$ compound is 0.05 for this substrate, and is indicated by the dashed line.

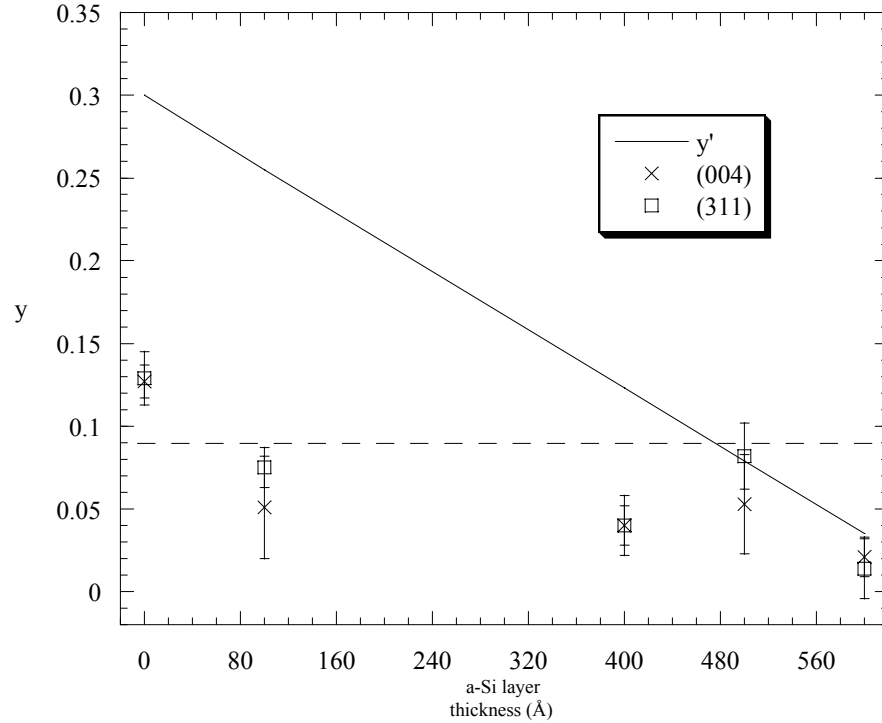


Figure 3.10: Comparison of y' (initial Ge concentration) and y (final Ge concentration) of as-deposited and amorphous layered samples for $\text{Si}_{1.7}\text{Ge}_{0.3}$ substrates calculated from XRD for (004) and (311) orientations. The solid line indicates y' versus the a-Si layer thickness. Symbols represent the Ge concentration versus a-Si layer thickness, as determined from the (004) and (311) diffraction peaks. The equilibrium Ge concentration of the $\text{Ti}(\text{Si}_{1-y}\text{Ge}_y)_2$ compound is 0.09 for this substrate, and is indicated by the dashed line.

layer thickness, we find that an amorphous layer of ~ 477 Å will equilibrate the two phases. Figure 3.11 presents a plot of a-Si layer thickness and $t_{\text{Ti}} / t_{\text{a-Si}}$ versus substrate concentration, at temperatures of 600, 700, and 800°C.

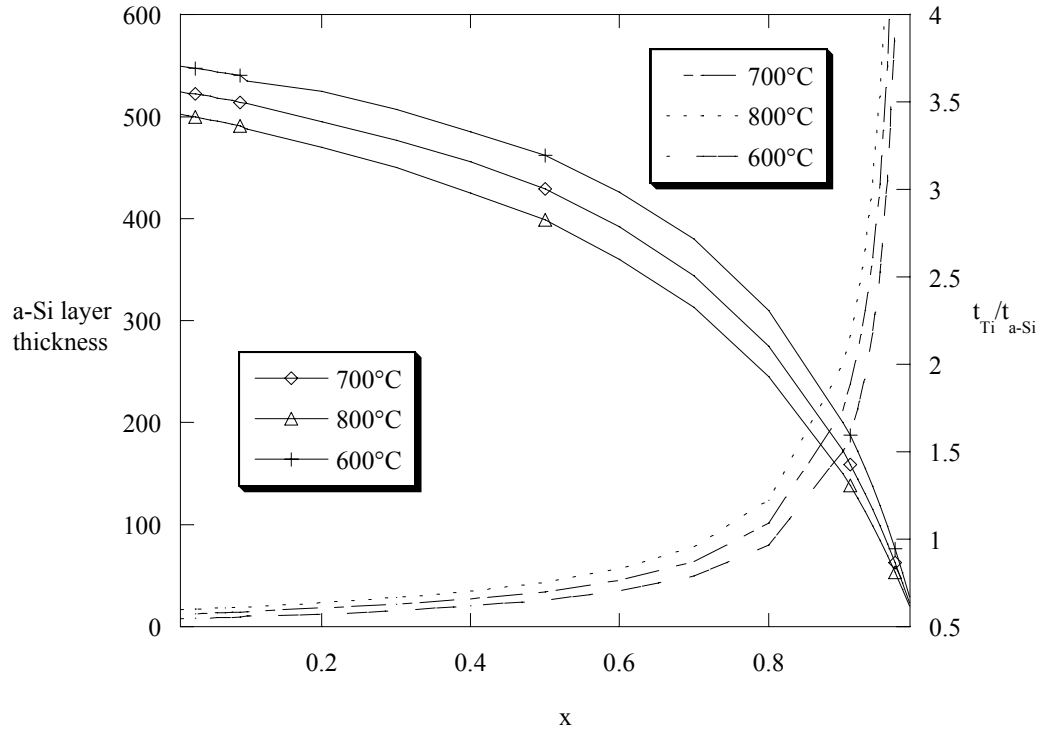


Figure 3.11: Plot of amorphous silicon layer thickness and ratio of Ti and a-Si layer thickness vs. germanium concentration of $\text{Si}_{1-x}\text{Ge}_x$ substrate at 600°C, 700°C, and 800°C. Solid lines indicate the a-Si layer thickness predicted to equilibrate to the equilibrium concentration (x) for a 300 Å layer of Ti. The dashed lines indicate the ratio of Ti to a-Si needed to equilibrate to a specific substrate germanium concentration (x) at 600°C, 700°C, and 800 °C for any Ti layer thickness.

It is interesting to note that the model predicts a decrease in minimum amorphous layer thickness with increasing substrate Ge concentration (x) at a given temperature. Note that an a-Si layer greater than the minimum thickness could still be used, with a value of y' which lies to the left of the phase equilibrium boundary, and,

based on our analysis, precipitation would be inhibited. Recalling the expressions for the change in free energies ΔG_1 and ΔG_2 , we find that the addition of a-Si serves to align the chemical potential minimum of the $\text{Ti}(\text{Si}_{1-y}\text{Ge}_y)_2$ layer to that of the $\text{Si}_{1-x}\text{Ge}_x$ substrate. The model further predicts that thicker a-Si layers are needed to equilibrate the system to a specific substrate Ge concentration at higher temperatures, which can be attributed to the need to balance the chemical potentials at the $\text{Ti}(\text{Si}_{1-y}\text{Ge}_y)_2/\text{Si}_{1-x}\text{Ge}_x$ interface as the temperature is increased.

A comparison of the ratio $t_{\text{Ti}} / t_{\text{a-Si}}$ to the substrate concentration allows the determination of the a-Si layer thickness appropriate for equilibration to a substrate at a specific value for x , regardless of Ti layer thickness. Thus, we find that stable $\text{Ti}(\text{Si}_{1-y}\text{Ge}_y)_2/\text{Si}_{1-x}\text{Ge}_x$ films could be formed and the process folded into the existing SALICIDE technology with a proper re-scaling of layer thickness.

3.5 Conclusion

The use of amorphous Si layers of varying thickness to control or eliminate the formation of germanium rich Si-Ge precipitates in the $\text{Ti}(\text{Si}_{1-y}\text{Ge}_y)_2/\text{Si}_{1-x}\text{Ge}_x$ thin film system has been investigated. Amorphous layers were incorporated between the sequentially deposited layers of titanium and strained $\text{Si}_{1-x}\text{Ge}_x$. The dynamics of the $\text{Ti}(\text{Si}_{1-y}\text{Ge}_y)_2/\text{Si}_{1-x}\text{Ge}_x$ bi-layer system was analyzed within the context of a Gibbs free energy model parameterized in terms of the Ge concentration of both the $\text{Ti}(\text{Si}_{1-y}\text{Ge}_y)_2$ equilibrium compound and $\text{Si}_{1-x}\text{Ge}_x$ solid solution. For a 300 Å Ti layer, reaction temperature of 700°C and substrate Ge concentration of $x = 0.20$ or $x = 0.30$, the Gibbs free energy model predicts that an amorphous layered sample with a thickness equal

to 495 Å or 477 Å should not contain precipitates in the grain boundary regions. Results from XRD and SEM indicated that a 300 Å Ti layer with 600 Å interlayer on $\text{Si}_{0.70}\text{Ge}_{0.30}$ did not form precipitates, and the 500 Å interlayer on $\text{Si}_{0.80}\text{Ge}_{0.20}$ showed a similar stability. We have proposed that a barrier to precipitate formation exists for $\text{Ti}(\text{Si}_{1-y}\text{Ge}_y)_2$ compositions that are to the Si rich side of the calculated stability, and this effect broadens the range of processing conditions which mitigate precipitate formation. The model has been used to determine the thickness of an a-Si layer required to equilibrate the bi-layer system for particular $\text{Si}_{1-x}\text{Ge}_x$ substrate compositions at temperatures of 600, 700, and 800°C. Thus, we have established the thermodynamic stabilities of the $\text{Ti}(\text{Si}_{1-y}\text{Ge}_y)_2$ - $\text{Si}_{1-x}\text{Ge}_x$ thin film structures and demonstrated a process that may be incorporated into existing IC manufacturing technology.

Acknowledgement

This research has been supported by the National Science Foundation (NSF) under Grant No. DMR 0102652, and the Department of Energy (DOE), contract numbers DE-FG05-93ER79236 and DE-FG05-89ER45384. James E. Burnette gratefully acknowledges the support through the GAANN Fellowship program of the Department of Education.

References

1. J. M. Stork, E. J. Prinz, C. W. Magee, IEEE Electron. Device Lett., **12** (1991) 303.
2. P. M. Garone, V. Venkataraman, J. C. Sturm, IEDM, **90** (1990) 383.
3. M. Arienzo, J. H. Comfort, E. F. Comfort, E. F. Crabbe, D. L. Hareme, S.S. Iyer, B. S. Meyerson, G.L. Patton, J. M. C. Stork, Y. C. Sunnin, Mater. Res. Soc. Proc., **220** (1991) 421.
4. D. C. Houghton, J. P. Noel, N. L. Rowell, Mater. Res. Soc. Proc., **220** (1992) 299.
5. Q. Z. Zong, J. W. Mayer, J. Appl. Phys., **66** (1989) 611.
6. H. K. Liou, X. Wu, U Gennser, Appl. Phys. Lett., **60** (1992) 577.
7. P. J. Wang, C. Chang, B. S. Meyerson, J. O. Chu, M. J. Tejwani, Mater. Res. Soc. Proc., **260** (1992) 863.
8. A. Buxbaum, M. Eizenberg, A. Raizmann, F. Schaffler, Mater. Res. Soc. Proc., **230** (1992) 151.
9. V. Aubry, F. Meyer, R. Laval, C. Clerc, P. Warren, D. Dutartre, Mater. Res. Soc. Proc., **320** (1992) 299.
10. D. B. Aldrich, F. M. d'Heurle, D. E. Sayers, R. J. Nemanich, Phys. Rev. B, **53** (1996) 16279.
11. Z. Wang, D. B. Aldrich, Y. L. Chen, D.E. Sayers, R. J. Nemanich, Thin Solid Films, **270** (1995) 555.

12. N. Boutarek , R. Madar, Appl. Surf. Sci., **73** (1993) 209.
13. R. J. Kasica, E. J. Cotts, J. Appl. Phys. , **82** (1997) 1488.
14. J.B. Lai, L. J. Chen, J. Appl. Phys. , **86** (1999) 1340.
15. D.B. Aldrich, H.L. Heck, Y.L. Chen, D.E. Sayers, R.J. Nemanich, J. Appl. Phys., **78** (1995) 4958.
16. E. Anastasskis, M. Cardona, “Phonons, Strians, and Pressure in Semiconductors”, in *High Pressure in Semiconductor Physics II* , edited by R.K. Willardson and A.C. Beer (American Press, San Diego 1998), vol 56, p.117.
17. F. Cerdeira, C.J. Buchenauer, F.H. Pollak, M. Cardona, Solid State Communications **114** (2000) 505.

Chapter 4

Titanium Interlayer Mediated Epitaxy of CoSi_2 on $\text{Si}_{1-x}\text{Ge}_x$

James E. Burnette, Dale E. Sayers, and Robert J. Nemanich

Submitted for Publication to Journal of Applied Physics

4. Titanium Interlayer Mediated Epitaxy of CoSi_2 on $\text{Si}_{1-x}\text{Ge}_x$

*James E. Burnette, Dale E. Sayers, Robert J. Nemanich
Department of Physics, North Carolina State University, Raleigh, NC 27695-8202*

Because of the emergence of Si-Ge as an important technological material, an understanding of the mechanisms of formation of CoSi_2 as a possible contact material for Si-Ge needs to be better understood. Structural similarities between Si and $\text{Si}_{1-x}\text{Ge}_x$ alloys have motivated a study of whether TIME could be successful in forming epitaxial CoSi_2 on $\text{Si}_{1-x}\text{Ge}_x$. Titanium layers of varying thickness were deposited as interlayers between Co and c-Si/ Si_8Ge_2 pseudomorphically grown on Si (100) to investigate their role in the formation of epitaxial CoSi_2 on Si-Ge alloys.

The effect of Ti interlayer thickness on the selective orientation of CoSi_2 to the $\text{Si}_{1-x}\text{Ge}_x$ substrate, and the circumstances under which a polycrystalline CoSi_2 film has been formed have been studied. It was found that Ti was beneficial in promoting epitaxy, and experimental results indicate that an interlayer thickness of about 50 Å enhanced the formation of epitaxial CoSi_2 adjacent to the substrate. In addition, it was shown that Ti was active in the formation of its own silicides.

4.1 Introduction

The future of integrated circuit (IC) technology is dependent on the production of stable metal silicide contacts to Si device structures. Current IC fabrication processes employ the formation of metal silicide source/drain contacts to Si, where the C54 phase of TiSi_2 is preferred due to its low resistivity. However, CMOS devices employing TiSi_2 as the electrical contact material suffer from structural instabilities at the source and drain regions, due to the lateral growth of the silicide over the oxide spacer. These instabilities lead to leakage currents in the device [11]. The formation of CoSi_2 contacts to Si has been explored as a candidate in the fabrication of CMOS devices and for implementation into existing self-aligned silicide (SALICIDE) processing schemes [29]. CoSi_2 is more desirable as a contact because its resistivity ($\sim 15 \mu\Omega \text{ cm}$) is comparable to that of TiSi_2 , yet it has a high thermal stability on Si and SiO_2 , and its cubic CaF_2 structure has a smaller lattice mismatch with Si. On the basis of this small lattice mismatch it might be expected that epitaxial CoSi_2 on Si (100) would form relatively easily. However, this is not the case.

The formation of CoSi_2 on Si (111) has been reported in the literature and is well documented [12]. However, the formation of epitaxial CoSi_2 on Si (100) by the sequential deposition of Co and Si on Si (100), or by the deposition of Co on Si (100) has been found to lead to the formation of a poly-crystalline CoSi_2 film. Epitaxial alignment of CoSi_2 on Si (100) has been found to occur in films where Co and Si were co-deposited. The proper control of the flux of Co and Si atoms was found to affect the phase formation and subsequent growth of the film [18]. Other methods

have also been used to achieve CoSi_2 epitaxy to Si, such as template methods, where thin layers of Co and Si are co-deposited at a low flux and at a prescribed temperature, in the stoichiometric amounts required for CoSi_2 formation, whereupon the further co-deposition of Co and Si and subsequent annealing leads to the formation of epitaxial CoSi_2 [5, 20]. However, the high-quality epitaxial films grown using this method were of limited thickness, as the critical thickness for strain relaxation using this template method was estimated to be about 65 Å. In addition, templating to Si (100) requires that the ratio of Co/Si atoms needed to form the initial template be carefully controlled to avoid the formation of a poly-crystalline silicide film [20].

One of the more successful means of promoting CoSi_2 epitaxy on Si has been by the use of what has been called TIME (Titanium Interlayer Mediated Epitaxy) [13]. In the Co/Ti/Si reaction, Ti assists the formation of epitaxial CoSi_2 by acting as an oxygen getter, cleaning the surface of the Si substrate, and controlling the diffusion of Co atoms, thereby controlling the formation of the successive cobalt silicide phases that eventually lead to the formation of CoSi_2 . The formation of a poly-crystalline CoSi_2 layer was found to occur in the interlayer mediated process unless the annealing stages are carried out in the presence of an ambient atmosphere, such as N_2 . Although the role Ti plays in the formation of epitaxial CoSi_2 remains unclear, its relative success with Si (100) has motivated this study of whether TIME can be used to form epitaxial CoSi_2 on $\text{Si}_{1-x}\text{Ge}_x$ pseudomorphically grown to Si (100).

The formation of CoSi_2 on Si-Ge was studied using the following general scheme, where $\text{Si}_{1-x}\text{Ge}_x$:c-Si:Ti:Co layers, with Ti layers 10, 30, 50, 70, and 100 Å

thick, were sequentially deposited on a Si (100). All samples were annealed in UHV at 700 °C, a temperature high enough to initiate phase formation, but not so high as to promote the generation of morphological instabilities in the film that develops. The films were grown on $\text{Si}_{0.8}\text{Ge}_{0.2}$ substrates, since this composition is close to that which is considered to be stable with CoSi_2 , according to the Co-Si-Ge ternary phase diagram [6]. The samples were characterized by Auger electron spectroscopy, x-ray diffraction, scanning electron microscopy, and x-ray absorption fine-structure measurements.

4.2 Experiment

The p-type Si (100) wafers were prepared for deposition by spin-etching in a $\text{HF}:\text{H}_2\text{O}:\text{ethanol}$ solution and then loaded into UHV for a thermal desorption at 900°C for 10 minutes, a procedure that has been shown to result in the removal of surface oxides and contaminants [5]. To enhance pseudomorphic growth of the strained $\text{Si}_{1-x}\text{Ge}_x$ layer, silicon buffer layers ~ 200 Å thick were grown at 550°C in a solid-source MBE chamber, at a rate of 2 Å/s. Strained $\text{Si}_{1-x}\text{Ge}_x$ layers with $x = 0.2$ were grown approximately 500 Å thick onto the buffer layer at a temperature of 550°C. Silicon and germanium for the $\text{Si}_{0.8}\text{Ge}_{0.2}$ substrates were deposited at a rate of 4 Å/s and 1 Å/s, respectfully. Both the buffer and $\text{Si}_{1-x}\text{Ge}_x$ layers were grown at a base pressure of $<2.4 \times 10^{-10}$ Torr.

Immediately after the $\text{Si}_{0.8}\text{Ge}_{0.2}$ layer had been formed, c-Si was deposited at a temperature of 550°C, and grown to a thickness of 728 Å, corresponding to the stoichiometric amount of Si needed to form CoSi_2 . This would prevent the consumption of Si from the $\text{Si}_{1-x}\text{Ge}_x$ layer, under the assumption that only Co atoms

combine with Si atoms to form a silicide as the reaction takes place. The deposition rate for the growth of the c-Si layer was 2 Å/s, and the deposition pressure was $<2.4 \times 10^{-10}$ Torr.

Following the growth of the c-Si layer, the samples were allowed to cool to a temperature of 22°C, and were transferred in UHV to an e-beam metallization chamber, base pressure $<3 \times 10^{-10}$ Torr, where layers of Ti were deposited with a thickness of 10, 30, 50, 70, and 100 Å, to study the effects of the diffusion barrier layer thickness upon phase formation. The deposition of a 200 Å thick Co layer at a temperature of 22°C was the final metallization step; all samples were subsequently annealed in UHV at 700°C for 15 minutes. Figure 4.1 shows the layered sequence after deposition, and the subsequent phase formation after annealing.

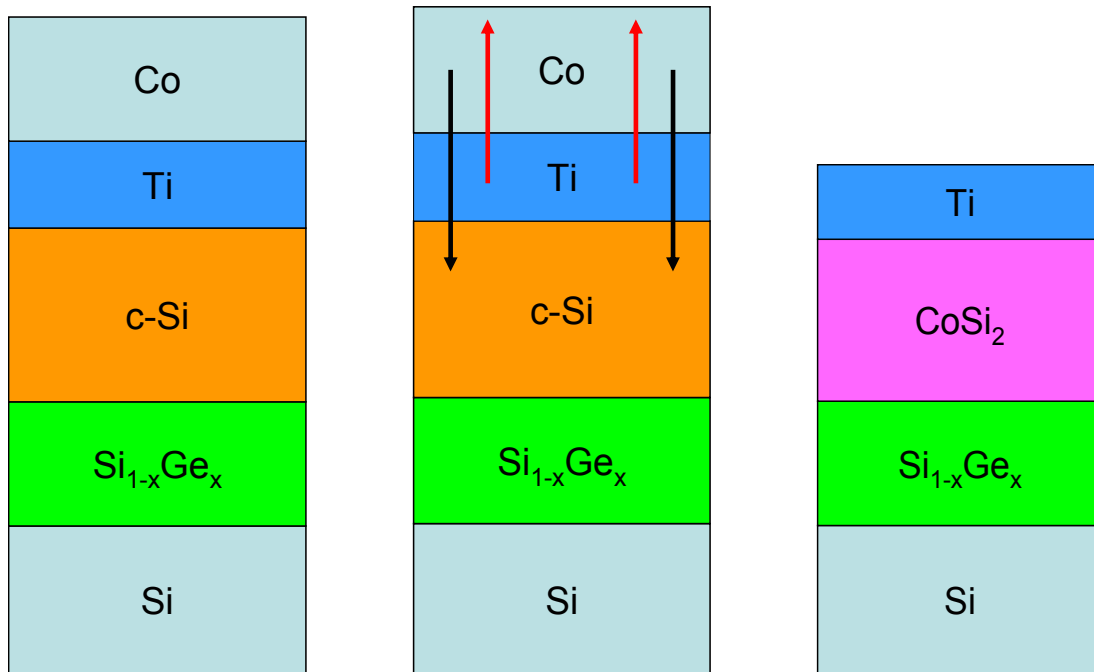


Figure 4.1: Layered structure after deposition and subsequent phase formation after annealing, which results in the interlayer inversion and epitaxial CoSi_2 adjacent to the substrate.

The films were studied *in situ* using Auger electron spectroscopy (AES) to determine the surface composition. The films were studied *ex situ* by x-ray diffraction (XRD) using a Rigaku Geigerflex diffractometer with Cu K_{α} radiation, at a 27kV tube voltage and 20mA tube current, and data was collected in a θ - 2θ mode, where 2θ ranged between 25-75°, with 1° diffraction and scattering slits, and a detector energy resolution of 42-45%. The surface morphology of the films was studied using a Joel Scientific model 6400 field emission scanning electron microscope. The short-range order present in the films was examined using x-ray absorption fine structure (XAFS), focusing on the x-ray absorption at Co and Ti K-edges and examining the near-edge structure of the films. The XAFS measurements were conducted at the National Synchrotron Light Source on beamline X-11A at Brookhaven National Laboratory.

4.3 Results

The long-range crystalline order was determined from the θ - 2θ x-ray diffraction scans, as shown in figures 4.2(a) and 4.2(b). Each sample was marked by the appearance of a Si (200) peak at 32.91°, shown in figure 4.2(a), as well as substrate peaks corresponding to diffraction from the $\text{Si}_{0.8}\text{Ge}_{0.2}$ (400) planes at ~ 68.00°, and the Si (400) $K\alpha_1$ and $K\alpha_2$ lines at 69.13° and 69.33°, respectively, as shown in figure 4.2(b).

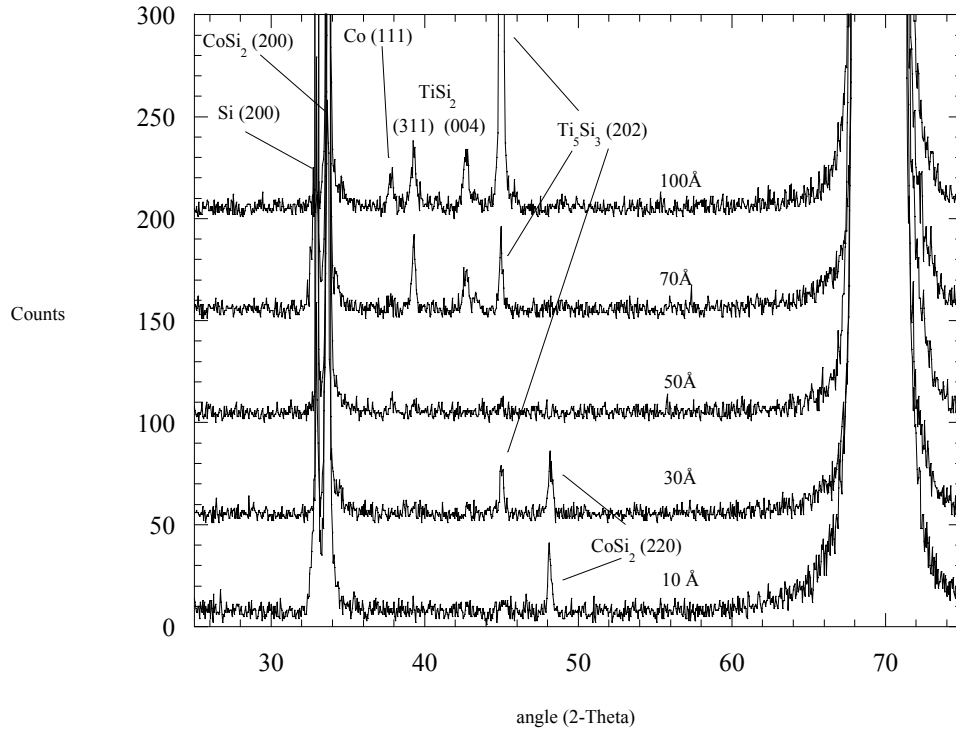


Figure 4.2(a): x-ray diffraction data for Ti diffusion barrier samples. Values for 2θ range between $25-75^\circ$.

As shown in figures 4.2(a) and 4.2(b), high intensity CoSi_2 (200) and (400) peaks, as well as a well-defined (220) peak of low intensity were present in the scan for the 10 Å diffusion barrier sample, whereas the (200), (400), and (220) peaks, in addition to a peak from a Ti_5Si_3 phase with (202) orientation were present in the 30 Å diffusion barrier sample. Aside from peaks associated with the substrate, only the CoSi_2 (200) and (400) peaks were present in the 50 Å diffusion barrier sample.

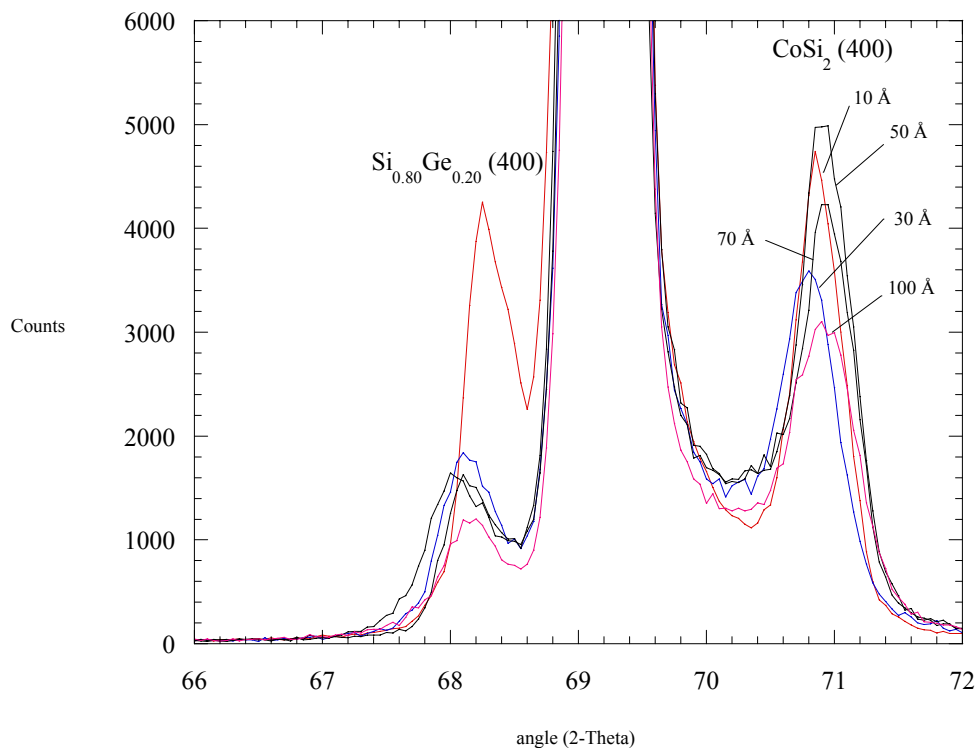


Figure 4.2(b): x-ray diffraction data indicating the formation of CoSi_2 (400) and $\text{Si}_{0.8}\text{Ge}_{0.2}$ (400). The $\text{Si}_{0.8}\text{Ge}_{0.2}$ substrate peak is located at $\sim 68.00^\circ$, while the peak corresponding to the formation of epitaxial CoSi_2 is located at $\sim 70.80^\circ$. In addition, the Si (400) $\text{K}\alpha_1$ and $\text{K}\alpha_2$ lines are located at 69.13° and 69.33° , respectively.

A change in Ti interlayer thickness from 50 to 70 Å and 100 Å was marked by a transition from the exclusive presence of cobalt silicide phases, to the re-emergence of peaks from the Ti-rich silicide phase of similar orientation but higher intensity, which increased with the diffusion barrier, and the presence of a relatively low intensity C54 TiSi_2 phase, with (311) and (004) orientation. The TiSi_2 in the 100 Å

sample was found to be more epitaxially aligned as compared to the 70 Å sample. In addition, a low intensity (111) peak corresponding to un-reacted Co metal was found in the 100 Å sample. The scan range was enlarged by extending the 2θ range to 150° ; no other peaks were seen, which indicated the absence of any additional ordered phases.

The out-of-plane lattice constants for the CoSi_2 films were calculated from XRD, starting with a value of $5.318 \pm 0.001 \text{ \AA}$ for the 10 Å interlayer sample, which decreased with increasing interlayer thickness to $5.308 \pm 0.001 \text{ \AA}$ for the 50 Å sample, and then increased with further increases in interlayer thickness to $5.314 \pm 0.001 \text{ \AA}$ for the 100 Å sample. The bulk CoSi_2 lattice constant is 5.367 \AA , which suggests that the films are under tensile stress in the plane of the interface.

The in plane lattice constants of the CoSi_2 film can be obtained using classical elasticity theory [43] and the CoSi_2 elastic constants [42], where it was found that the in plane lattice constant of CoSi_2 ranged from $5.527 \pm 0.09 \text{ \AA}$ for the 10 Å interlayer to a maximum of $5.531 \pm 0.09 \text{ \AA}$ for the 50 and 70 Å interlayers, but was marked by an decrease in lattice constant back $5.527 \pm 0.09 \text{ \AA}$ for the 100 Å sample. This suggests that the films exhibited a small amount of relaxation, calculated to be in the range of 0.1% - 3% according to the uncertainty in the lattice constant, since the in-plane lattice constant of $\text{Si}_{0.8}\text{Ge}_{0.2}$ layer should be equal to that of bulk Si, with a value of 5.4310 \AA .

SEM micrographs of the Ti diffusion barrier samples are shown in figures 4.3(a)-4.3(e). The surfaces of the Co-silicide films formed during the reaction can be

seen in all of the figures. In addition, the micrographs reveal the presence of pinholes in the 10, 30, and 100 Å samples. The results indicate that islands are found on the surface of the CoSi_2

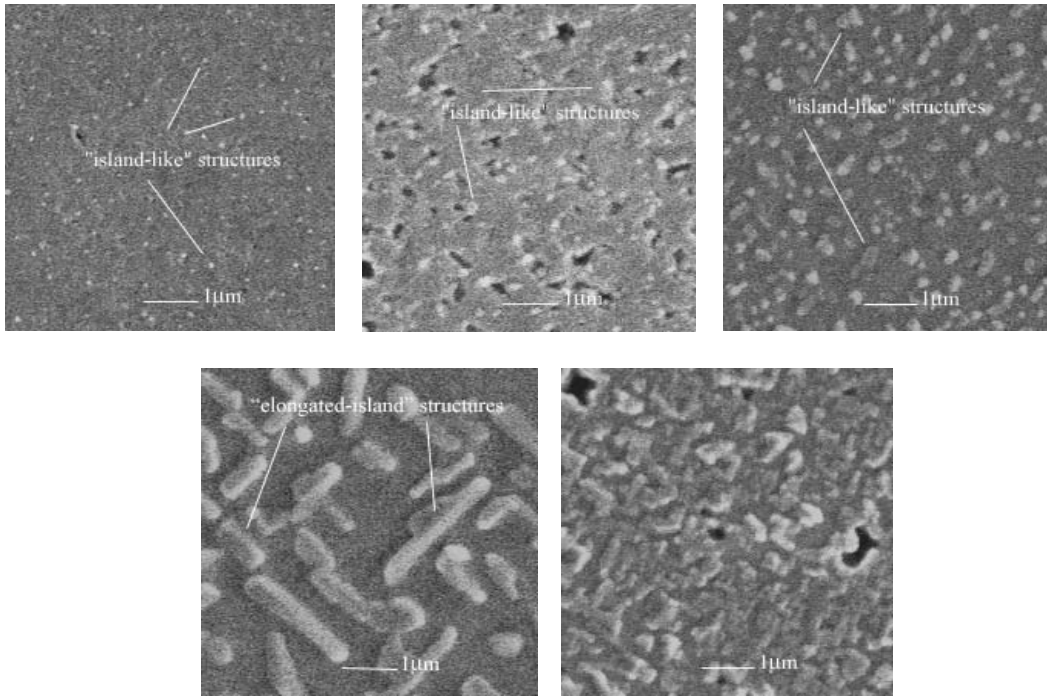


Figure 4.3 (a)-(e): SEM micrographs of sample surface for interlayers of 10, 30, 50, 70, and 100 Å, from left to right, which reveal the surface of the CoSi_2 film, and the existence of the layer inversion by-products on the surface of the CoSi_2 film.

film in the 10 Å diffusion barrier sample as shown in figure 4.3 (a), with similar results occurring in the 30 and 50 Å samples, as shown in figures 4.3(b) and 4.3 (c).

The islands on the surface of the 50 Å sample are about a factor of 2 larger than those found on the surface of the 10 and 30 Å samples. Elongated island structures, which appear to be oriented along preferential directions, are found on the surface of the 70 Å diffusion barrier sample as shown in figure 4.3 (d). The SEM micrograph of the 100 Å sample indicates the formation of a somewhat agglomerated surface layer which also appears to be oriented along preferential directions, just as in the case of the 70 Å diffusion barrier sample, and appear to have a size distribution that ranges on the order of 1-10 μm, as shown in figure 4.3 (e).

The short-range order in the films was examined by using XAFS, focusing on x-ray absorption at the Co and Ti K edges. The near-edge structure (XANES) scans for both Co and Ti are shown in figures 4.4 and 4.5. All of the XANES data were pre-processed by background removal and edge energy calibration using the Athena EXAFS Data Processing program, and the data were fit to reference compound standards using Six PACK, both of which are graphical user interfaces (GUI's) to the IFEFFIT XAFS analysis numerical library [32].

In figure 4.4, the near edge spectra for the samples and for Co and CoSi₂ reference standards are shown. A comparison between the spectra and reference standards indicate that the films are predominately CoSi₂, with respect to the Co-Si reaction. A linear interpolation of the samples of interest to the Co and CoSi₂ reference standards indicates that the films are roughly 96 ± 3% CoSi₂ and 4 ± 3% Co metal.

An examination of the Ti K edge x-ray absorption data shown in figure 4.5 indicates the presence of TiO₂/TiSi₂/Ti₃Si₃ phases in the 10, 30, and 50 Å samples,

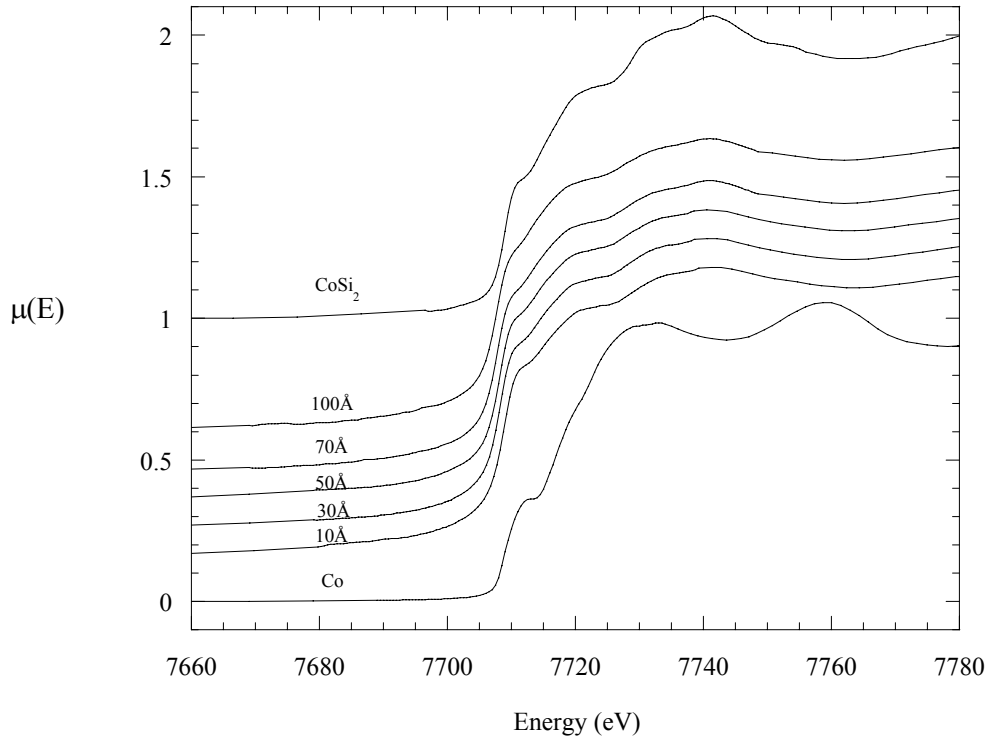


Figure 4.4: Co K-edge XANES spectra.

whereas mostly TiSi_2 and Ti_5Si_3 was found in the 70 and 100 Å samples. A graph of the data and associated fits for the samples is shown in figure 4.6. In figure 4.6, the sample data is indicated by a solid line, while the fit data is indicated by a dashed line. The fits were performed assuming that the signals from the near-edge data were linear combinations of anatase TiO_2 , Ti_5Si_3 , and C54 TiSi_2 , in an energy range ± 50 eV above and below the absorption edge.

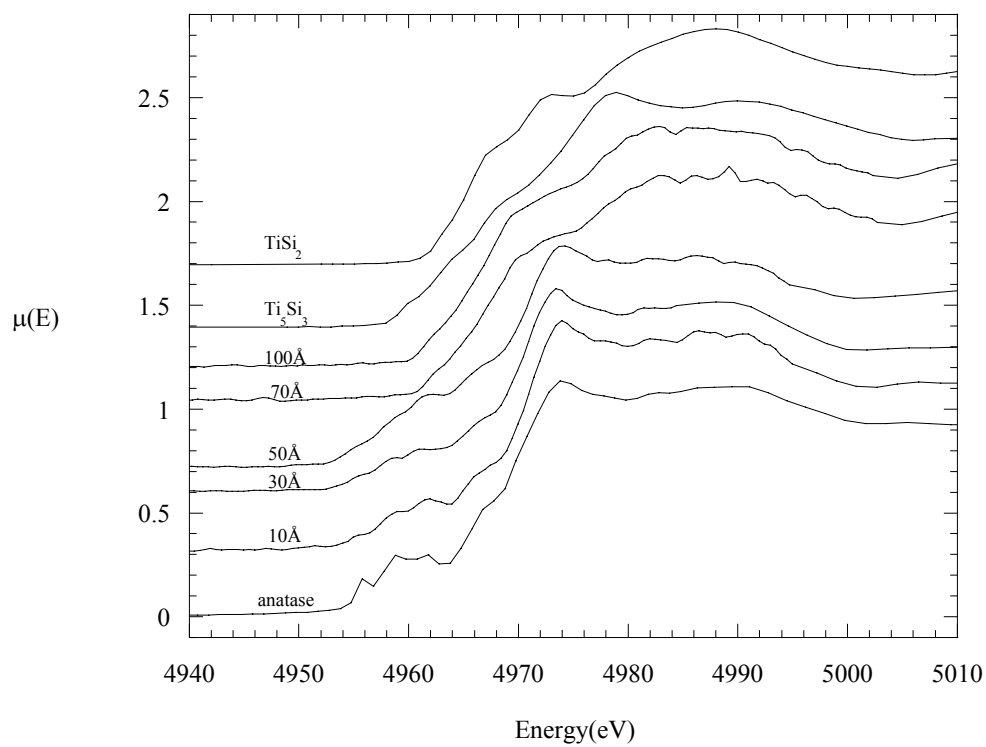


Figure 4.5: Ti K-edge XANES spectra.

The AES of the samples after annealing and an analysis of a 50 Å diffusion barrier sample before and after annealing at 700°C for 15 minutes in UHV are shown in figures 4.7 and 4.8. As shown in figure 4.8, Si, Ti, and Co LMM peaks indicate the

presence of these elements at or near the surface of the film. A difference in the peak-to-
to-

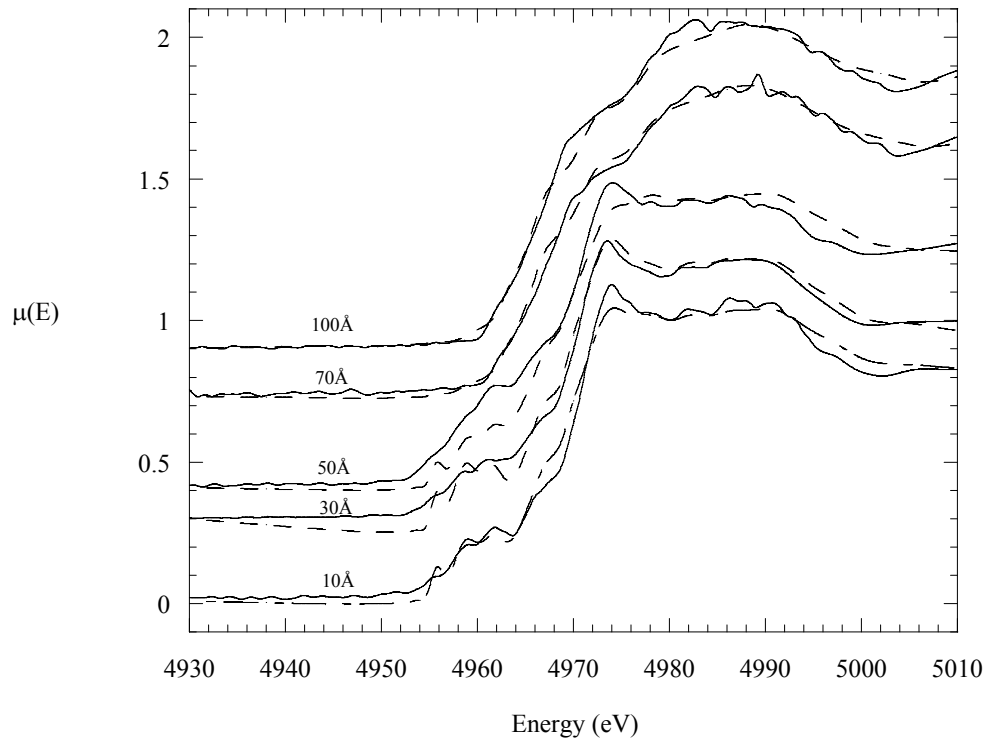


Figure 4.6: Comparison of XANES data from x-ray absorption at the Ti K edge and fits to the data, assuming that the signal from each sample is a linear combination of signals from TiO_2 , Ti_5Si_3 , and TiSi_2 reference standards. The actual data for each sample is indicated by the solid line, while the fit to the data is indicated by the dashed line.

peak heights from the Si, Ti, and Co signals can be seen, consistent with the increase in the interlayer thickness. As shown in figure 4.8, for the 50 Å diffusion barrier

before and after annealing case, after annealing, a decrease in the Co signal is observed. A Ti peak is not present before annealing since the Ti interlayer is covered by a thick layer of Co. Its emergence after annealing suggests the presence of Ti or a Ti compound on or near the surface of the film, which would attenuate the signal from the underlying layer containing Co and Si atoms.

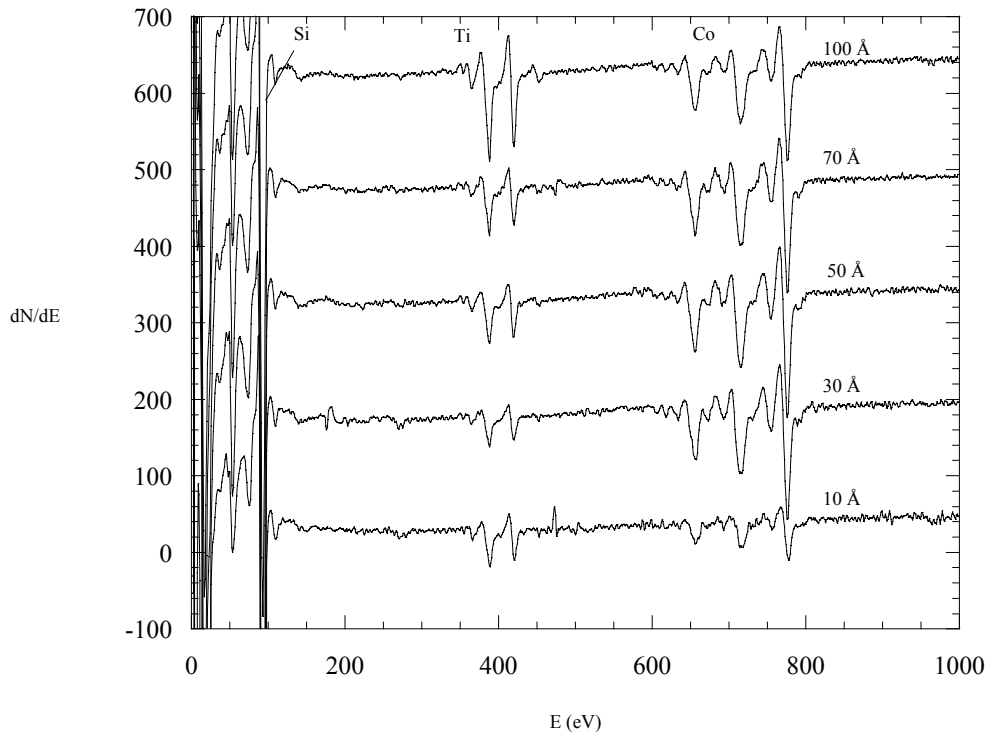


Figure 4.7: AES scans of inter-layered samples after annealing at 700 °C for 15 minutes.

4.4 Discussion

The formation of CoSi_2 on Si (100), using Co/Ti bi-layers has been well documented [2, 4, 13, 9, 21]. Titanium has been proposed to assist in this process by reducing the native oxide on the silicon surface, and by controlling the movement of Co atoms towards the substrate, acting as a diffusion barrier.

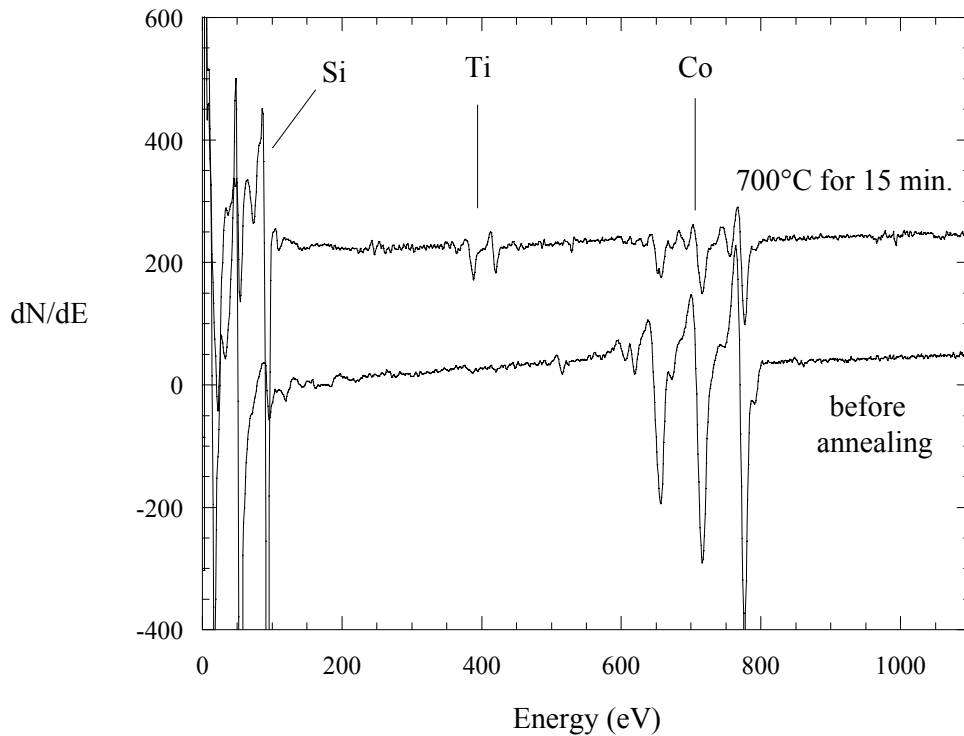


Figure 4.8: AES spectra of 50 Å diffusion barrier sample before annealing and after annealing at 700 °C for 15 minutes.

Previous studies related to the formation of CoSi_2 in the bi-layer reaction include a study by Dass, *et.al.*, in which the formation of epitaxial CoSi_2 was

achieved by the sequential deposition of 100-300 Å Ti and 200-300 Å Co layers on Si (100), followed by rapid thermal annealing in a nitrogen enriched environment at temperatures ranging from 450-900°C [4]. This resulted in a layer of epitaxial CoSi₂ covered with TiN. In other studies by Vantomme, *et.al*, it is suggested that the annealing ambient plays a significant role in epitaxial CoSi₂ formation on Si (100). The sequential deposition of 85 Å of Ti and 230 Å of Co, followed by annealing in N₂, N₂+H₂, and He+H₂ environments over a temperature range of 300-900°C resulted in the formation of epitaxial CoSi₂ covered by a layer of TiO_y. In contrast, annealing in vacuum resulted in the diffusion of Si to the sample surface and the formation of epitaxial CoSi₂, in addition to a Si-rich Co-Ti-Si ternary phase, which was conjectured to influence the availability of Co, thereby limiting the growth of CoSi₂ adjacent to the substrate [2, 21].

In this work, the results from SEM and AES indicate the inversion of the diffusion barrier. The AES spectra indicate that the Co signal near the surface has decreased as a result of its attenuation by the inverted interlayer, and that most, if not all of the available Ti or formed Ti compound can be found on or near the sample surface. The surface of the CoSi₂ film, in addition to the existence of islanded structures adjacent to the film has been indicated by SEM. The results from XAFS and XRD are also consistent as they both indicate the formation of a highly-oriented CoSi₂ phase, in addition to the formation of both Si-rich and Ti-rich Ti silicide phases.

The appearance of the Ti(O) phase in the XAFS data and the absence O peaks from the AES data indicate that while under vacuum the island structures are mainly

composed of un-reacted Ti, Ti_5Si_3 , and TiSi_2 , which are present on the surface of the cobalt disilicide layer after inversion and CoSi_2 formation, and that the un-reacted Ti was oxidized after removal from the UHV environment.

This information, related to the inversion of the interlayer, is somewhat consistent with that which has already been reported in the literature for the Co/Ti/Si solid phase reaction. This study differs from others in the sense that the existence of Ti_5Si_3 and TiSi_2 phases has been confirmed, which has not been reported in other studies, whereas the ternary Co-Ti-Si phase reported in Refs. [2, 21] and from other studies was not observed in the XRD data. According to the ternary phase diagram for the Co-Ti-Si system [28], stability exists between Si , $\text{Co}_{0.25}\text{Ti}_{0.75}\text{Si}_2$, CoSi_2 , and TiSi_2 phases at high temperature and under Si-rich conditions. It was conjectured [2, 21] that under Si-rich conditions, the ternary phase and at least one of the two silicide phases should form, as was confirmed experimentally in these studies by RBS, XRD, and both plain-view and cross-sectional TEM. Since the ternary phase is a Si-rich one, the absence of the ternary phase in these experiments is most likely attributable to the limited availability of Si during the reaction sequence.

Ti_5Si_3 has been shown to be one of the first silicide phases to form in investigations concerning the stages of silicidation in Ti/Si films [33-37]. These studies confirm that the Ti_5Si_3 compound nucleates, probably at the interface between the a-TiSi layer formed during the initial stages of the silicidation process and the Ti layer at temperatures between 400-500 °C. The transformation of the Ti_5Si_3 compound into a Si-rich silicide occurs under the availability of Si, in addition to increases in the

annealing temperature. The presence of Ti_5Si_3 , as confirmed by XRD and XAFS, suggests that although the annealing temperature in these experiments was high enough to induce its transformation to a Si-rich silicide, the transformation was affected by the availability of Si from the underlying substrate, due to its consumption by Co atoms in the nucleation and formation of the $CoSi_2$ film, and from the remaining Ti which eventually reacted with Si to form its own Si-rich silicide phase.

The experimental data indicate the formation of Co silicide and a delay in significant Ti silicide formation, until the initial thickness of the interlayer is 70 Å. From these trends, it appears that both Co and Ti actively compete to form bonds with Si in the formation of their respective silicide, depending on the initial thickness of the interlayer. The competition between the phases has been studied by Alberti, *et.al.* [1], and Hong, *et.al.* [27] to obtain a qualitative explanation of experimental results found in multi-layered Co/Ti/Si systems, and can be modeled by considering the rate dependent free energy change associated with the Co-Si and Ti-Si reactions, which can be expressed as

$$-\Delta G = -\int_0^t \left(\frac{d\Delta G}{dt}\right) dt \quad (1)$$

for both reactions, and where for the Co-Si reaction the rate of energy change

$-\left(\frac{d\Delta G}{dt}\right) = -F \bullet \nu$, $F = \sum_i \alpha_i \mu_i$, the chemical affinity of the Co-Si reaction, is the

driving force for the reaction, $\nu = \frac{D}{2x}$ is the reaction rate, where in this simple case it

is assumed that the initial thickness of the interlayer $x = \sqrt{Dt}$, and D is the diffusion coefficient of Co in the interlayer [27]. It can be seen from the expression for the

reaction rate that increases in interlayer thickness x will lead to a decrease in the diffusion of Co through the barrier (and a decrease in the reaction rate), and therefore decrease the rate of energy change.

Evidence of this competition can be obtained from the XRD and the XANES least squares analysis information. A graph, depicting the fraction of the initial Ti layer converted into a silicide phase as a function of diffusion barrier thickness, determined from the Ti K-edge XANES data, is shown in figure 4.9, where it can be seen that the formation of TiSi_2 is delayed

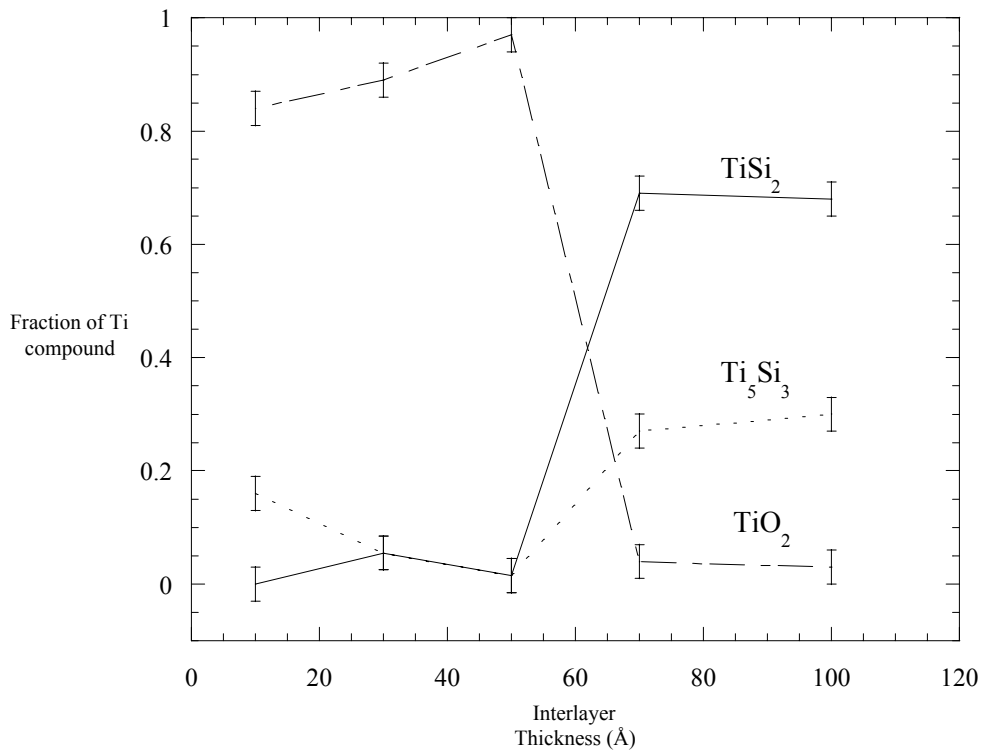


Figure 4.9: Fraction of silicide formation as a function of diffusion barrier thickness.

until the initial interlayer thickness is 70 Å. This crossover point, denoted by the onset of significant TiSi₂ formation, can also be correlated with the information from XRD, as the diffraction pattern from the 50 Å interlayer sample indicates the absence of any other long-range ordered phases besides CoSi₂ and the substrate, while that of the 70 Å sample indicates the formation of a oriented TiSi₂ phase. This indicates that the formation of CoSi₂ was delayed with increases in interlayer thickness to the extent such that Ti was allowed to react more with Si, thereby competing with Co to form its own Si bonds, in the barrier thickness region between 70-100 Å.

By considering the rate of energy change for both reactions the formation of the Ti-silicide phase is more likely to occur first when the rate of energy change in the Co-Si reaction is equal to that for the Ti-Si reaction, or $-\left(\frac{d\Delta G}{dt}\right)_{\text{Co-Si}} = -\left(\frac{d\Delta G}{dt}\right)_{\text{Ti-Si}}$.

An expression for the Ti-Si reaction rate can then be formulated. If it is assumed that during growth the thickness of both silicide films is proportional to \sqrt{t} , then from Eqn. (1) the driving force for the formation of CoSi₂ can be expressed as

$$F_{\text{Co-Si}} = -\mu_{\text{Co}} - 2\mu_{\text{Si}} + \mu_{\text{CoSi}_2} \quad (2)$$

while the driving force for the formation of TiSi₂ can be expressed as

$$F_{\text{Ti-Si}} = -\mu_{\text{Ti}} - 2\mu_{\text{Si}} + \mu_{\text{TiSi}_2} \quad (3)$$

In the absence of mixing between Co and Si atoms, and Ti and Si atoms in the formation of their respective compounds, the driving forces can be approximated by the chemical potentials of the CoSi₂ and TiSi₂ compounds. In addition, the absence of

mixing between the metal silicides allows a further approximation of the driving forces, so that they are equal to the respective Gibbs free energies of formation. Assuming Gibbs free energies of formation of 134 kJ/mol for TiSi₂ and 102 kJ/mol for CoSi₂ [7], then the reaction rate for TiSi₂ formation can be expressed as

$$v_{\text{TiSi}_2} = \frac{D_0 e^{-\frac{\Delta G_a}{kT}}}{2x} \left(\frac{\Delta G_{\text{CoSi}_2}}{\Delta G_{\text{TiSi}_2}} \right) \cong \frac{D_0 e^{-\frac{\Delta G_a}{kT}}}{2x} (0.7611) \quad (4)$$

where D_0 is the pre-exponential factor for diffusion of Co in Ti, ΔG_a is the activation energy for diffusion of Co in Ti, and x is the thickness of the interlayer.

Unfortunately, reliable estimates for the values of D_0 and ΔG_a are not available. However, it can be assumed that the values are greater than those for TiSi₂ formation. Then the reaction rates should be relatively larger than those for Co silicide formation, and a small difference in reaction rates should be observed as the interlayer thickness is increased beyond the thickness which is associated with the onset of significant TiSi₂ formation.

By controlling the flux of Co atoms toward the substrate, the interlayer assists in the formation of substrate matched nuclei [31]. It is conjectured that as the diffusion barrier thickness is increased from 10 to 50Å, and as both Ti and Si react, Co is able to diffuse through the diffusion barrier in sufficient amounts and at a sufficient rate for epitaxial nucleation. As the interlayer thickness is increased to 70 and 100Å, the diffusion of Co decreases, and more of the interlayer interacts with available Si to form its own compounds. This in turn will decrease the amount of Si available to form CoSi₂, and could possibly affect the reaction kinetics of the CoSi₂

formation, and explains the presence of the Co-rich silicide phases and un-reacted Co found in the XRD scans for the 70 and 100 Å samples.

Pinholes on the surface of the CoSi_2 film were found in the 10 and 30 Å samples, with an aerial density of $\cong 1.68 \times 10^8 \text{ cm}^{-2}$. The formation of pinholes was not observed in significant numbers in the 50 and 70 Å samples. However, the formation of pinholes is again observed in the 100 Å sample, but with a smaller aerial density than that of the 10 and 30 Å samples. Surface reconstruction on the CoSi_2 (100) surface have been studied by Kenny, *et.al.* [22] and Hayashi, *et.al.* [23], and the formation of pinholes has been associated both with the transformation of the CoSi_2 film from a Co-terminated surface to a Si-terminated surface, as the pinholes are formed in order to permit diffusion of Si from within the layer to form the lower energy Si-terminated structure, and also any differences between the surface energies of the CoSi_2 film and Si substrate. The formation of pinholes has also been studied in the $\text{CoSi}_2/\text{Si}_{1-x}\text{Ge}_x$ system by Boyanov, *et.al.* [5] during the reaction between thin Co films and a Si-Ge film which had been pseudomorphically strained to Si (100). The stronger preference for Co-Si bonding as opposed to Co-Ge bonding at the $\text{CoSi}_2/\text{Si}_{1-x}\text{Ge}_x$ interface was proposed to lead to an increase in the interfacial energy which would drive the morphological instability. It is unclear whether both effects play a role in the formation of pinholes in this case. It is worthy to note that under the effect of both influences, in cases where the pinhole formation is non-existent, the thickness of the interlayer is such that the amount of reactants in the region adjacent to the substrate are controlled by the presence of the interlayer to the extent that when the CoSi_2 film eventually nucleates, the Si-terminated structure is the one that

initially forms and the Co-terminated \rightarrow Si-terminated surface transformation previously mentioned does not occur [22, 23, 26]. In addition, the presence of the c-Si layer serves to prevent contact between the Si-Ge layer and Co atoms diffusing towards it, until the CoSi_2 phase is able to nucleate and grow, and the further consumption of the c-Si leads to the positioning of the CoSi_2 layer adjacent to Si-Ge. In this manner, intimate contact between the two layers can be minimized until the Co silicide forms, and the problem with preferential Co-Si bonding discussed in Ref. 5 could be eliminated.

Previous studies have also shown that the presence of the Ti interlayer exerts an influence on the nucleation barrier to CoSi_2 formation. Studies by Detavernier, *et.al.* [15, 30, 31] examined the role of refractory metal interlayers in the nucleation of epitaxial CoSi_2 on Si (100). It was theorized that refractory metals which were soluble in Co_2Si or CoSi could form a ternary silicide phase and alter the CoSi_2 nucleation barrier by influencing the Gibbs free energy difference between the initial monosilicide or Co-rich silicide phase and the resulting CoSi_2 compound. However, refractory compounds which are not miscible in Co_2Si or CoSi , such as Ti, could alter the nucleation barrier by influencing the CoSi grain boundary and interfacial energies and by reducing CoSi grain boundary diffusion, leading to an increase in nucleation temperature and giving rise to a preferential orientation of CoSi_2 nuclei.

This suggests that, in this experiment, Ti may also be present as a contaminant within the grain boundaries and interfaces of the CoSi_2 film, where the reduction in grain boundary diffusion and reduction in interfacial energy between CoSi grains would lower the CoSi_2 nucleation barrier, leading to an increase in nucleation

temperature and augmenting the formation of CoSi_2 nuclei. However, since the film growth was characterized after the reaction had taken place, there is no experimental evidence which directly supports this assumption.

The possibility of the presence of Ti within the CoSi interfaces and grain boundaries, in addition to the fact that the diffusion barrier interlayer controls the flux of Co atoms towards the substrate, lends credence to the possibility that a templating mechanism is at work in forming epitaxial CoSi_2 adjacent to the substrate. However, previous studies which detail the templating mechanism involved in the formation of TiSi_2 on Si substrates [39-41] and CoSi_2 on Si substrates [38] which employ Ta as an interlayer suggest that the ability of both Ti and Co to form solid solutions with Ta, in addition to the existence of in-plane crystal symmetries between CoSi_2 or TiSi_2 and their respective Ta solid solutions is the primary mechanism responsible for templating. This suggests that the Ti interlayer used in these experiments is not likely to lend itself to templating, due to the lack of in-plane symmetries between the terminal silicide phases.

4.5 Conclusion

The growth of epitaxial CoSi_2 thin films on Si_8Ge_2 has been demonstrated, and the various Ti and Co silicide phases formed after annealing have been characterized using AES, XAFS, XRD, and SEM. Overall, the presence of a Ti interlayer has been found to be beneficial to the formation of CoSi_2 on Si_8Ge_2 , and an interlayer thickness of 50-60 Å was found to be optimal for the formation of CoSi_2 , resulting in the consumption and transformation of Co into CoSi_2 , and the

absence of any long-range ordered Ti silicide, Co-rich silicide or un-reacted Co phases.

The final chemical state of Ti interlayer was also observed, as the results from AES and an analysis of Ti-K edge absorption data suggests the formation of TiO_2 , Ti_5Si_3 , and TiSi_2 compounds in the 10, 30, and 50 Å diffusion barrier samples, indicating that titanium was an active participant in the formation of its own silicides, as opposed to reports indicating the formation of a Co-Ti-Si ternary phase in the conventional Co/Ti bi-layer reaction. Additionally, the XRD scans do not indicate the presence of any long-range ordered TiO_2 phases for these interlayer thicknesses. It is most likely that exposure of these samples to air resulted in their oxidation, and not the formation of any titanium oxides during film growth, as it is thermodynamically favorable for Si to react with titanium oxides, forming TiSi_2 and SiO_2 at high temperatures. The formation of the C54 TiSi_2 and Ti_5Si_3 with some degree of long-range order was confirmed by x-ray diffraction and XAFS, while the existence of a TiO_2 phase was confirmed by XAFS, for the samples with 70 and 100 Å interlayer thicknesses.

The diffusion barrier was found to affect the surface energetics of the CoSi_2 film, by effectively controlling the amount of reactants, possibly leading to the formation of the low-energy Si-terminated surface as indicated by the absence of pinholes in the 50 and 70 Å samples. It was also conjectured that the presence of the c-Si layer would delay the interaction between the CoSi_2 layer and the substrate, minimizing the increase in interfacial energy associated with preferential Co-Si

bonding found in the $\text{Co/Si}_{1-x}\text{Ge}_x$ system, which is thought to promote the formation of pinholes as well.

It was speculated that Ti could influence the nucleation of the CoSi_2 phase by acting as a contaminant at film grain boundaries and interfaces. It was also suggested that the interlayer could play a role as a template in the formation of CoSi_2 , as the presence of Ti has been shown to control the diffusion of Co towards the substrate, as well as influence grain boundary and interfacial energies and control grain boundary diffusion. However, the lack of in-plane symmetries between the existing compounds, as well as the absence of any Co-Ti solid solutions negates this possibility.

These occurrences can be explained by considering the initial bi-layer arrangement, and the diffusion of Si in Co and Ti, as well as differences in the Gibbs free energies of formation for both CoSi_2 and TiSi_2 .

Acknowledgements

The authors would like to thank Franz Koeck for his assistance in generating the SEM micrographs. This work was supported through funding from the National Science Foundation Grant [DMR 0102652], the Department of Energy, contract numbers DE-FG05-93ER79236 and DE-FG05-89ER45384 and the GAANN Fellowship. Research was partly done at beamline X-11A at the National Synchrotron Light Source (NSLS), Brookhaven National Laboratory. The NSLS is supported by the U.S. Department of Energy, Division of Materials Science and Division of Chemical Science.

References

1. A. Alberti, F. La Via, F. Rimini, J. Vac Sci. Technol. B, **17** (1999) 1448.
2. A. Vantomme, Marc-A. Nicolet, G. Bai, D. B. Fraser, Appl. Phys. Lett. , **62** (1993) 243.
3. S. L. Zhang, J. Cardenas, F.M. d'Heurle, B.G. Svensson, C.S. Petersson Appl. Phys. Lett., **66** (1995) 58.
4. M.L.A. Dass, D. B. Frazier, C. Wei, Appl. Phys. Lett., **58** (1991) 1308.
5. B. I. Boyanov, P.T. Goeller, D.E. Sayers, R.J. Nemanich, J. Appl. Phys., **86** (1999) 1355.
6. K.Maex, M. Van Rossum, Properties of Metal Silicides, INSPEC, (1995) 103.
7. F. R. deBoer, R. Boom, W. C. M. Mattens, A. R. Midema, A. K. Niessen, Cohesion in Metals: Transition Metal Alloys, North Holland, (1988) 259.
8. D.B. Aldrich, H.L. Heck, Y.L. Chen, D.E. Sayers, R.J. Nemanich, J. Appl. Phys., **78** (1995) 4958.
9. F. M. deHeurle, L. Miglio, Silicides: Fundamentals and Applications, Proceedings of the 16th Course of the International School of Solid State Physics, World Scientific (1999) ppg. 39, 352.
10. K. Barmak, L.A. Clevenger, P.D. Agnello, E. Ganin, M. Copel, P. Dehaven, J. Falta, F.M. d'Heurle, C. Cabral Jr., Mat. Res. Symp. Proc. **238** (1992) 575.
11. S.L. Hsia, T.Y. Tan, P. Smith, G. E. McGuire, J. Appl. Phys. **70** (1991) 7579.
12. T. Komeda, T. Hirano, G.D. Waddill, S.G. Anderson, J.P. Sullivan, J.H. Weaver, Phys. Rev. B **41** (1990) 8345.
13. R.T. Tung, F. Schrey, Appl. Phys. Lett., **67** (1995) 2164.

14. Z. Wang, D.B. Aldrich, Y.L. Chen, D.E. Sayers, R.J. Nemanich, *Thin Solid Films*, **270** (1995) 555.
15. C. Detavernier, R.L. van Meirhaeghe, F. Cardon, K. Maex, *Phys. Rev B*, **62** (2000) 12045.
16. M.A. Taubenblatt, C.R. Helms, *J. Appl. Phys.*, **53** (1982) 6308.
17. H. Hamamura, H. Itoh, Y. Shimogaki, J. Aoyama, T. Yoshimi, J. Ueda, H. Komiyama, *Thin Solid Films*, **320** (1998) 31.
18. S.M. Yalisove, R.T. Tung, D. Loretto, *J. Vac. Sci. Technol. A*, **7** (1989) 1472.
19. J.S. Byun, H.J. Kim, *J. Appl. Phys.* **78** (1995) 6784.
20. S.M. Yalisove, R.T. Tung, J.L. Batstone, *Mat. Res. Soc. Symp. Proc.* **116** (1988) 439.
21. A. Vantomme, M.A. Nicolet, N.D. Theodore, *J. Appl. Phys.* **75** (1994) 3882.
22. S.D. Kenny, I. Goldfarb, E. Akhmatskaya, G.A.D. Briggs, *Surface Science* **465** (2000) 259.
23. Y. Hayashi, M. Yoshinaga, H Ikeda, S. Zaima, Y. Yasuda, *Surface Science* **438** (1999) 116.
24. M. Iannuzzi, L. Miglio, *Surface Science* **479** (2001) 201.
25. B.-S. Chen, M.-C. Chen, *J. Appl. Phys.* **74** (1993) 1035.
26. R.T. Tung, J.L. Batstone, *Appl. Phys. Lett.* **52** (1988) 648.
27. F. Hong and G.A. Rozgonyi, *J. Electrochem. Soc.* **141** (1994) 3480.
28. *Handbook of Ternary Alloy Phase Diagrams.*
29. L. Van den hove, R. Wolters, K. Maex, R. De Keersmaecker, G. Declerck, *J. Vac. Sci. Technol. B* **4** (1986) 1358.

30. C. Detavernier, X.P. Qu, R.L. VanMeirhaeghe, B.Z. Li, and K. Maex, *J. Mater. Res.* **18** (2003) 1668.
31. C. Detavernier, R.L. VanMeirhaeghe, F. Cardon, K. Maex, W. Vandervorst, and B. Brijs, *Appl. Phys. Lett.* **77** (2000) 3170.
32. M. Newville, *J. Synchrotron Rad.* **8** (2001) 322.
33. B. Chenevier, O. Chaix-Pluchery, P. Gergaud, O. Thomas, R. Madar, and F. La Via, *Microelectron. Eng.* **70** (2003) 166.
34. L. Lu and M.O. Lai, *J. Appl. Phys.* **94** (2003) 4291.
35. G.G. Bentini, R. Nipoti, A. Armigliato, M. Berti, A.V. Drigo, and C. Cohen, *J. Appl. Phys.* **57** (1985) 270.
36. M.H. Wang and L.J. Chen, *J. Appl. Phys.* **71** (1992) 5918.
37. B. Chenevier, O. Chaix-Pluchery, P. Gergaud, O. Thomas, and F. La Via, *J. Appl. Phys.* **94** (2003) 7083.
38. J.S. Byun, S.B. Kang, H.J. Kim, C.Y. Kim, and K.H. Park, *J. Appl. Phys.* **74** (1993) 3156.
39. A. Mouroux, T. Epicier, S.-L. Zhang, and P. Pinard, *Phys. Rev. B* **60** (1999) 9165.
40. B.I. Boyanov, H. Jeon, D.E. Sayers, and R.J. Nemanich, unpublished results.
41. H. Jeon, H. Won, Y. Kim, J. Lee, and R.J. Nemanich, *J. Korean Phys.Soc.* **40** (2002) 903.
42. G. Guénin, M Ignat, and O. Thomas, *J. Appl. Phys.* **68** (1990) 6515.
43. C.A. Pico and M.G. Lagally, *J. Appl. Phys.* **64** (1988) 4957.

5. Conclusions

The stability of $\text{Ti}(\text{Si}_{1-y}\text{Ge}_y)_2$ films on $\text{Si}_{1-x}\text{Ge}_x$ and the formation of epitaxial CoSi_2 on $\text{Si}_{1-x}\text{Ge}_x$ have been investigated. It was found that the stability was governed by both thermodynamics and kinetics in the Ti-Si-Ge and Co-Ti-Si solid phase reactions.

5.1 $\text{Ti}(\text{Si}_{1-y}\text{Ge}_y)_2/\text{Si}_{1-x}\text{Ge}_x$ stability

The investigation of the thermodynamic stability of $\text{Ti}(\text{Si}_{1-y}\text{Ge}_y)_2$ films on $\text{Si}_{1-x}\text{Ge}_x$ employed the use of a Gibbs free energy model, parameterized in terms of the concentration of Ge by atomic percent, in order to determine stability between the titanium germanosilicide film and the silicon germanium substrate. The model allowed the calculation of the Ge concentration (y) of the $\text{Ti}(\text{Si}_{1-y}\text{Ge}_y)_2$ film which would be in equilibrium with $\text{Si}_{0.80}\text{Ge}_{0.20}$ and $\text{Si}_{0.70}\text{Ge}_{0.30}$ substrates. This allowed for the construction of a Ti-Si-Ge ternary phase diagram, and also allowed for the determination of the two phase field connecting the equilibrium phases.

Once the conditions of stability were determined, the appropriate thickness of amorphous silicon interlayers which, when combined with Ti and a portion of the $\text{Si}_{1-x}\text{Ge}_x$ layer, would form titanium germanosilicide in thermodynamic equilibrium with the remaining $\text{Si}_{1-x}\text{Ge}_x$ was calculated. It was determined that the formation of Ge-rich Si-Ge precipitates could be controlled by implementing an amorphous interlayer. This behavior was attributed to the availability of both Si and Ge within the titanium germanosilicide phase.

5.2 CoSi₂/Si_{1-x}Ge_x

The formation of epitaxial CoSi₂ on Si_{1-x}Ge_x was investigated. The titanium interlayer mediated epitaxy (TIME) process has been shown to promote the formation of CoSi₂ on Si (100). Studies indicate that the purpose of the Ti interlayer is to remove native oxides from the Si surface, and also to control the flux of Co atoms towards the substrate, resulting in the formation of epitaxial CoSi₂ grains on Si (100). However, a more detailed explanation of this phenomenon is found lacking in the literature.

The formation of epitaxial CoSi₂ on pseudomorphically strained Si_{1-x}Ge_x as a function of Ti interlayer thickness was investigated. It was found that as in the Co/Ti/Si (100) case, the presence of the interlayer promoted epitaxy to Si_{1-x}Ge_x. Beyond a certain thickness, the interlayer was found to react with available Si, forming its own silicide compounds. This interplay between Co and Ti in the formation of silicides has been modeled by considering the time rate of change in the Gibbs free energy of formation for each silicide phase. Significant Ti silicide formation was found to occur when the rate of change in the Gibbs free energy was equal for both silicides. The experimental results were in qualitative agreement with the model and consistent with results in the Co/Ti/Si system. In addition, the results were found to be comparable to other methods for promoting epitaxy, such as the template and modified template methods, where small amounts of Co and Si are deposited to form a CoSi₂ template before the final metallization step.

5.3 Future Work

The formation of metal silicide and metal germanosilicide thin films on both Si and $\text{Si}_{1-x}\text{Ge}_x$ has been extensively studied. Both Co and Ti are in a subset of the available metals with which to study these reactions. Possible extensions of this research involve an electrical characterization of these films, possibly employing the use of 4-point probe sheet resistance measurements. These studies could also encompass the use of x-ray photoelectron spectroscopy (XPS) to obtain detailed band structure information and to determine the Schottky barrier height (SBH) of these metal silicide and germanosilicide compounds on $\text{Si}_{1-x}\text{Ge}_x$.

Other possible extensions involve the study of forming silicide and germanosilicide compounds in the solid phase reaction of $\text{Si}_{1-x}\text{Ge}_x$ with metals such as vanadium, niobium, and tantalum, whose silicide and germanide phases have been shown to exhibit superconducting properties. Partial miscibility has been shown to exist between vanadium silicide and germanide, so that the likelihood of a V-Si-Ge phase is possible. However, further study is required to determine the feasibility of these studies.

These ideas can also be extended to study stability in nanoscale structures, where additional Gibbs free energy terms, such as surface and interfacial energies can come into play and perhaps be more dominant than the thermodynamic contributions. A question to be addressed is whether stability in nanoscale structures can be depicted using the usual phase diagrams (binary, ternary, or otherwise), or does a new method of indicating stability need to be formulated.